Vol.1, No.1, October 2010

Scientific Research

# Journal of Biomaterials and Nanobiotechnology

www.scirp.org/journal/jbnb

# Journal Editorial Board

http://www.scirp.org/journal/jbnb

*Journal of Biomaterials and Nanobiotechnology*, **2010, 1, 1-76**
Published Online October 2010 in SciRes (http://www.SciRP.org/journal/jbnb/)

# TABLE OF CONTENTS

**Volume 1 Number 1 October 2010**



 

# Journal of Biomaterials and Nanobiotechnology (JBNB)

# Journal Information

## SUBSCRIPTIONS

The *Journal of Biomaterials and Nanobiotechnology* (Online at Scientific Research Publishing, www.SciRP.org) is published quarterly by Scientific Research Publishing, Inc., USA.

### Subscription rates:

Print: $50 per issue.
To subscribe, please contact Journals Subscriptions Department, E-mail: sub@scirp.org

## SERVICES

**Advertisements**
Advertisement Sales Department, E-mail: service@scirp.org

**Reprints (minimum quantity 100 copies)**
Reprints Co-ordinator, Scientific Research Publishing, Inc., USA.
E-mail: sub@scirp.org

## COPYRIGHT



## PRODUCTION INFORMATION

For manuscripts that have been accepted for publication, please contact:
E-mail: jbnb@scirp.org

*Journal of Biomaterials and Nanobiotechnology*, **2010, 1, 1-6**
doi:10.4236/jbnb.2010.11001 Published Online October 2010 (http://www.SciRP.org/journal/jbnb)

# Novel Engineered Human Fluorescent Osteoblasts for Scaffolds Bioassays

**Katia Campioni[1], Cristina Morelli[1], Antonio D'Agostino[2], Lorenzo Trevisiol[2], Pier Francesco Nocini[2], Marco Manfrini[1], Mauro Tognon[1*]**

[1]Section of Cell Biology and Molecular Genetics, School of Medicine and Centre of Biotechnology, University of Ferrara, Ferrara, Italy; [2]Department of Odontostomatology and Maxillo-Facial Surgery, School of Medicine and School of Dentistry, University of Verona, Verona, Italy.
Email: *tgm@unife.it

Received July 7th, 2010; revised July 28th, 2010; accepted July 29th 2010.

## ABSTRACT

*Many cellular models have been used to investigate bone substitutes including coral-derived hydroxylapatite (HA). The aim of this study was to verify whether a new cellular model represented by Saos-eGFP cells can be used to test biomaterials by in vitro assays. Saos-eGFP cells which express the enhanced Green Fluorescent Protein (eGFP), were derived from the osteoblast-like cell line Saos-2. To this purpose Saos-eGFP cells were employed to investigate the in-vitro bioactivity of a well characterized coral-derived HA biomaterial, in block and granule forms. This engineered cell line, by evaluating the emitted fluorescence, allowed us to assay (i) cell adhesion, (ii) cell proliferation and (iii) colony capability. Electron microscopy analysis was employed to evaluate the (iv) morphology of cells seeded on the biomaterial surface. (v) Histological analysis of the bone grown after scaffold implantation was carried out in specimens from two clinical cases. Saos-eGFP cells indicate, as established before, that the coralline-HA biomaterials has a good in vitro cytocompatibility when tested with human osteoblast-like cells. Some differences in proliferation activity was detected for the two different forms assayed. Cytocompatibility data from in vitro analyses were confirmed by in vivo behaviour of biomaterials. Our tests suggest that the engineered cell line Saos-eGFP represents a suitable in vitro mode for studying the biocompatibility, the cell adhesion, spreading and proliferation on biomaterials developed for clinical applications. The main advantages of this cellular model are (i) less time consuming and (ii) a reduced cost of the experiments.*

***Keywords*: *Fluorescence, Osteoblast, Biomaterial***

## 1. Introduction

Investigations into bone substitutes have been addressed to different biomaterials including coral-derived hydroxylapatite (HA). One of the main goals of this biomaterial, which is similar in its chemical composition to human bone, is to modulate cellular responses which control the interaction with the scaffold. Specifically, it may induce spontaneous three dimensional self-organisation in the new tissue, as it has been observed in the physiological environment [1,2]. Indeed, cell behaviour and phenotype are governed by responses to different types of signals that include mechanical forces, electrical stimuli, and various physical cues [3]. In addition, cells sense and respond to a variety of signals including soluble growth factors, differentiation factors, cytokines, and ion gradients [4-6]. Materials employed as scaffolds must possess specific features, such as cyto- and bio-compatibility, osteo-inductivity and -conductivity, as well as the right mechanical strength to provide structural support during tissue growth and remodelling. Besides those of a bovine origin, natural HA biomaterials can also be derived from coral exoskeletons (genus Porites and Goniopora). Hydrothermal treatment (260°C.; 15,000 PSI) of the calcium carbonate exoskeletal microstructure of these corals results in conversion into hydroxylapatite [7]. Different hydrothermal coral treatments have resulted in only partial conversion of its calcium carbonate to HA [8]. As a result, its HA/$CaCO_3$ composite is resorbed faster than pure HA. Like natural bone, this HA may contain minor elements such as Mg, Sr, F, and $CO_3$ and has a completely interconnected porosity which is similar to trabecular bone.

 

Coral-derived HA biomaterial in block and granule forms, as well as other types of HA materials, have been well characterized for many parameters including their cytocompatibility using different cellular models [9-11]. These cellular models however are time-consuming, with high costs and tedious to be used.

The aim of this study was to investigate whether a new cellular model known as Saos-eGFP, derived from the osteoblast-like cell line Saos-2, can be employed for the in-vitro bioactivity of coral-derived HA biomaterial in block and granule forms. Saos-eGFP is a genetically engineered cell line obtained from Saos-2 osteosarcoma cells which express the enhanced Green Fluorescent Protein (eGFP) [12,13]. Saos-eGFP cellular model allowed us to assay (i) cell adhesion, (ii) cell proliferation and (iii) colony capability, by evaluating their emitted fluorescence. We also evaluated the (iv) morphology of the cells seeded on the biomaterial surface by employing electron microscopy. In addition, (v) histological analyses of bone grown in vivo after scaffold implantation are presented.

Our data indicate that human Saos-eGFP fluorescent cells employed to test the well characterized coral HA, as a standardized biomaterial, is a good cellular model to characterize scaffolds.

## 2. Materials and Methods

### 2.1. Saos-eGFP Cell line

An engineered human osteoblast-like cell line, known as Saos-eGFP, was obtained from parental Saos-2 cells as described elsewhere [12,13]. In brief, Saos-eGFP cells were cultured in DMEM-F12 (BioWhittaker, Milan, Italy) supplemented with 10% fetal bovine serum (BioWhittaker, Milan, Italy), 500 µ/ml penicillin/streptomycin (Sigma, Milan, Italy), and maintained in a humidified atmosphere at 37°C containing 5% $CO_2$. The antibiotic Genetycin (500 ug/ml), known as G418 (Invitrogen, Milan, Italy) was employed to keep in selection Saos-2 cells, engineered with the recombinant plasmid vector expressing the enhanced green fluorescent protein (eGFP) which carries the resistance gene (Neo) to the antibiotic (**Figure 1**). A known number of Saos2-eGFP ($5 \times 10^3$, $10 \times 10^4$, $20 \times 10^4$, $40 \times 10^4$, $80 \times 10^4$, $16 \times 10^5$) was seeded and cultured for 24 hours in 24-well plates (Ø = 10 mm). A calibration curve was obtained by reporting the number of cells present in each sample, which emitted fluorescence, on a graph (excitation λ = 488 nm, emission λ = 508 nm) (**Figure 2**).

### 2.2. Biomaterial

The assayed biomaterial, which is commercially available, is made with marine coral exoskeleton material,

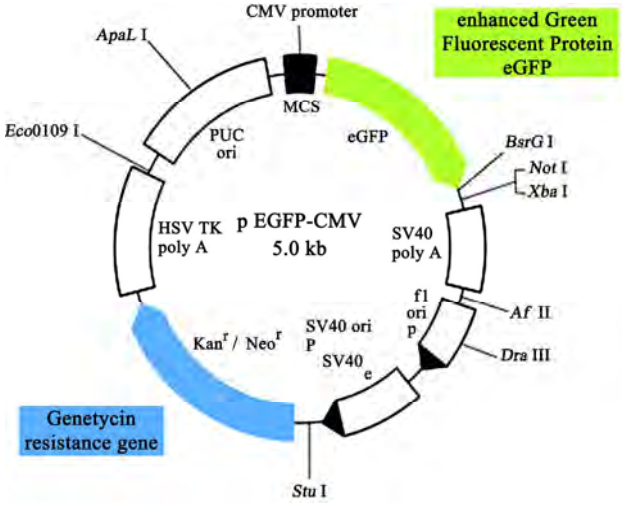


**Figure 1. pEGFP plasmid vector showing the eGFP insertion site and the Neo resistance gene.**

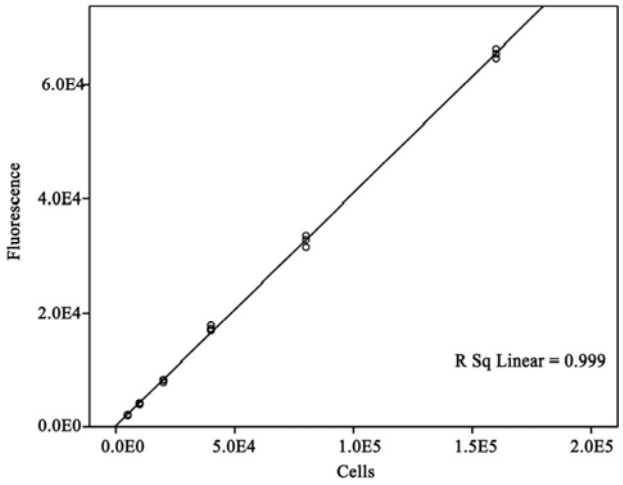


**Figure 2. The calibration curve was obtained by seeding Saos-eGFP cells at different densities and measuring the fluorescence emitted (excitation λ = 488 nm, emission λ = 508 nm). R value showed a good positive correlation between cells number and fluorescence emitted.**

hydrothermally converted to hydroxylapatite (HA). HA scaffolds are indicated for use as cancellous bone substitutes or as augmentation material for repairing bone defects, in combination with autologous bone, allografts, blood or bone marrow. This HA material is routinely used in oral-maxillo-facial surgery clinical practice for bone regeneration. In our cyto-compatibility assays the biomaterial was employed both in small blocks (10 × 10 × 10 mm) and granules (1 ÷ 4 mm).

### 2.3. Scaffold Cell Loading

Proliferating Saos-eGFP cell monolayers, at 50 ÷ 60%

 

confluence, were detached from the culture flasks and re-suspended in culture medium to obtain a cell suspension with a density of $10^4$ cells/cm$^2$ surface area, in 1 ml, for each scaffold. A tissue culture polystyrene (TCPS) vessel was employed as control. The scaffold was then placed in wells (Ø = 10 mm) filled with the proper cell suspension and incubated for 2 h. To maximize cell-scaffold interaction, cell suspension was subjected to pipetting every 15 min. After the incubation period, scaffolds were placed in empty wells. Fresh culture medium, 1 ml, was added to each scaffold.

### 2.4. Cell Adhesion and Proliferation

Saos-eGFP cells were loaded onto scaffolds and TCPS (control), in 24-well culture plates (Ø = 10 mm) and cultured as described above. In order to mimic the clinical application environment, the same volume of bone void filler was used for each type of scaffold. To analyze cell adhesion on each biomaterial and on the control, samples were incubated for 24 h at 37°C, 5% $CO_2$. Attached cells per scaffolds were detected by measuring the fluorescence (excitation $\lambda$ = 488 nm, emission $\lambda$ = 508 nm) emitted by the viable cells. Then, cells were re-fed with fresh culture medium and cultured at 37°C in a humidified atmosphere with 5% $CO_2$. Assays were carried out to evaluate cells attached on biomaterials and on the control, at 24 h, 48 h, and 96 h.

### 2.5. Cell Spreading

Saos-eGFP cells were loaded onto the scaffolds and TCPS, in 24-well culture plates (Ø = 10 mm) and cultured as described above. Samples were incubated for 24 h, 48 h ad 96 h at 37°C, 5% $CO_2$. Direct observation of the living cells on the biomaterial was carried out by fluorescence microscopy in order to determine their distribution, colonization and morphology on the biomaterials.

### 2.6. Scanning Electron Microscopy (SEM)

For the SEM analysis, Saos-eGFP ($10^4$ cells/well) were cultured on HA scaffolds for 48 h. Cells which were attached to the biomaterials were washed with PBS 1X solution and fixed for 1 h by 2.5% glutaraldehyde in a phosphate buffer and then for 4h with a 1% osmium solution in a phosphate buffer. Specimens were coated with colloidal gold and analyzed using scanning electron microscopy (SEM, Cambridge UK, model Stereoscan S-360).

### 2.7. Histology

Granules were used for maxillary sinus augmentation in patients with bone resorption in the posterior segment of the upper jaw for implant-prosthetic rehabilitation. Blocks were used as interpositional materials in orthognathic surgery patients when the upper jaw was down grafted in order to increase the stability of the mobilized segment. Biopsies were taken in accordance with the local ethical committee and after patients' written consent. In one clinical case (patient 1), biomaterial granules were used for bone regeneration in a patient who had undergone maxillary sinus augmentation for pre-prosthetic surgical rehabilitation. In this patient, a bone biopsy was taken four months after the first surgical procedure, during implant surgery. In another clinical case, (patient 2), to correct dentoskeletal deformities, blocks of biomaterial were employed as interpositional grafts in a patient treated with LeFort I osteotomy. Bone biopsies were taken from this patient, during plate removal, one year after surgery. Tissues were fixed in 4% formaldehyde and dehydrated in a graded series of alcohols. Then, all specimens were embedded in methylmethacrylate resin. Undecalcified sections were obtained using a water-cooled diamond saw. Slides were ground to a final thickness of about five μm, placed on glass slides, stained with hematoxilin- eosin and viewed and photographed in a Leitz Orthoplan photomicroscope.

### 2.8. Statistical Analysis

All data were obtained from five independent experiments and expressed as a mean value ± SD. ANOVA testing followed by post-hoc Bonferroni testing was employed to evaluate differences in the mean values among groups. Statistically significant findings were considered when $p < 0.05$. All data elaboration was computed by SPSS (SPSS Inc., Chicago, IL, U.S.A.).

## 3. Results

### 3.1. Cell Adhesion and Proliferation

The results obtained showed a good adhesive capability of Saos-eGFP cells to the biomaterial. Indeed, Saos-eGFP cells attached both to block and granules of the biomaterial with a prevalence of 67% and 64%, respectively, compared to seeded cells. In the control experiment, 94% of the seeded cells were attached to the plastic well, showing a statistically significant difference ($p < 0.01$) as regards the two scaffolds (**Figure 3**). Cells proliferated in each sample during the assay as in the control ($p < 0.01$). At 48 h, the fluorescence detected for the granules was lower than the fluorescence detected for the control and block ($p < 0.01$). Cells grown on blocks behaved differently, as shown by the data obtained at 96 incubation h. Indeed at this point, the fluorescence detected on these samples diminished with statistically significant differences as regards the control and granules ($p < 0.05$) (**Figure 4**).

 

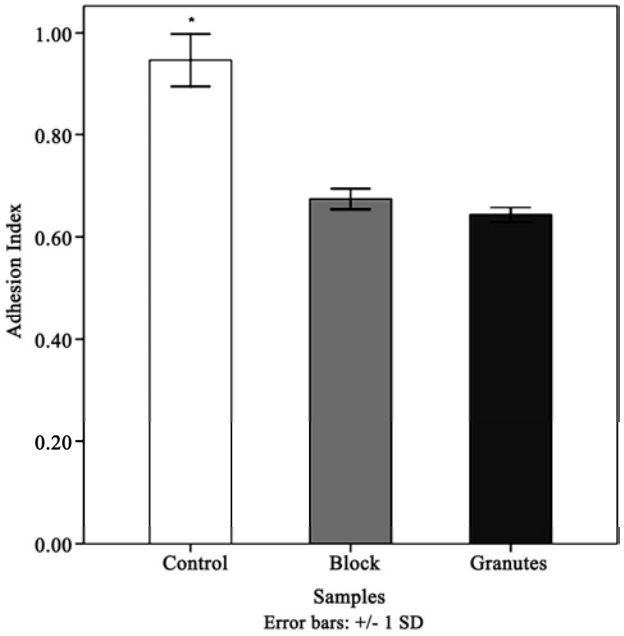


**Figure 3. Adhesion index at 24 hours of incubation for controls and biomaterials, expressed as a ratio of living cells detected by fluorescence intensity measurement at 24 incubation hours, and cells seeded.**

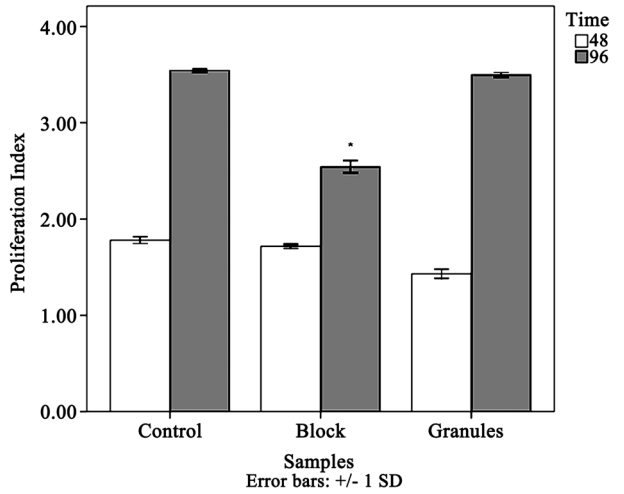


**Figure 4. Proliferation index for control and biomaterials, expressed as a ratio of living cells detected by fluorescence intensity measured at 48 hours and 96 incubation hours respectively, and living cells detected at 24 incubation hours.**

## 3.2. Cell Spreading

In the control experiment, the cell population was homogeneously distributed and appeared to have a normal morphology. Cells behaved similarly for both forms of the biomaterial. Indeed, the cells were able to colonize homogeneously on both granules and blocks (**Figure 5**).

## 3.3. Scanning Electron Microscopy

The results obtained with the SEM analysis indicate no difference in the morphology of the cells grown on the biomaterial under analysis, both granules and blocks, when compared to the control. SEM images revealed the presence of several cells anchored to the surface of the biomaterial by cytoplasmic bridges, which were similar to pseudopodia (**Figure 6**). In addition, a large amount of biomaterial debris was detected on the surface of the cell membrane. This debris was not present on the cells grown on glass, where the cell surface appeared homogeneous.

## 3.4. Histological Evaluation

Histological analysis (patient 1) showed new bone formation with resorption of the biomaterial. Indeed, fibro-osseous tissue represented about 50% of the biopsy volume, while lamellar bone was 10% of the biopsy. Bone fatty marrow and vessels represented 40% of the biopsy. There was no evidence of inflammation or foreign body reactions. The histological evaluation (patient 2) showed,

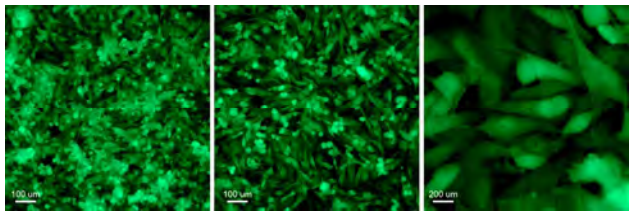

(a) (b) (c)

**Figure 5. Direct observation by fluorescence microscope. At 48 h the Saos-eGFP cells appeared well attached to the control (a) as well as to the biomaterials. The assay revealed a homogeneous distribution of Saos-eGFP cells on the surfaces of the biomaterials, both the blocks (b) and granules (c).**

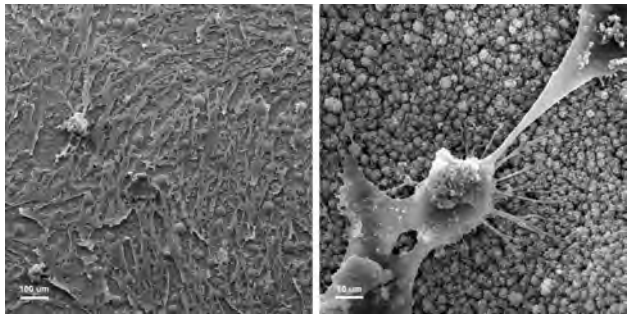

(a) (b)

**Figure 6. SEM images showed that at 48 h, Saos-eGFP cells were homogeneously distributed on block biomaterials surface (a) and appear anchored to the granular scaffold by cytoplasmic bridges also involved in cells interaction (b). Debris is also evident on the cell surface.**

 

as expected, the residual biomaterial surrounded by mature compact bone. There was evidence of bone regrowth inside the biomaterial giving continuity between osteotomy sites with significant stability for the down grafted maxilla. This biomaterial represented 20% of the biopsy volume, while bone density was in the order of 40%. The remaining 40% of the biopsy was represented by fibro-osseous tissue. In this patient, a minor inflammation process with the presence of macrophages was revealed by histological analysis (**Figure 7**).

## 4. Discussion

Saos-eGFP cells were employed to determine mature osteoblastic cell morphology, spread and proliferation on coralline-HA biomaterials. Saos-eGFP on the biomaterial showed homogeneous spreading and a different rate of proliferation. This result demonstrates that composition, surface shape and biomaterial morphology, may influence the relationship between scaffold and cell. Indeed, Saos-eGFP cells which attached to the biomaterial, in the two forms assayed, showed a good adhesion ratio, although lower than for the control (TCPS). Biomaterial blocks appear to provide a better environment for adhesion compared to biomaterial granules, as shown by the percentage of adhered cells and by proliferation at 48 culture hours. Otherwise, the proliferation index determined for the biomaterial in blocks was lower than for granules at 96 incubation hours. Results showed that the granular form of the biomaterial has a greater capability to achieve Saos-eGFP cell proliferation. Direct observation at the fluorescence microscope showed that in the control experiment, the cell population was homogeneously distributed and appeared to have a normal morphology. Cells behaved similarly on both forms of the biomaterial until 96 cultivation hours. Indeed, cells were able to colonize homogeneously both granules and blocks forming colonies on the surface and on the trabecular structure of the biomaterials. SEM images revealed the presence of several cells anchored to the surface of the biomaterial by cytoplasmic bridges, which appeared similar to pseudopodia, confirming the capability of the biomaterial to achieve cell adhesion. The presence of debris, absent on cells grown on glass, observed at 48 and incubation hours, is probably an additional cause for the diminished number of cells grown on the block after that incubation period.

Histological evaluations indicated that both biomaterial granules and blocks showed osteoconductive properties, inducing new bone formation. From a clinical point of view, the osteoconductive properties were confirmed by the stability of the endosseous implants inserted in the posterior segment of the maxilla and in down grafted maxilla.

The possibility of learning which biomaterial leaves cell morphology, spread and proliferation unaltered, would be an important step towards obtaining bone tissue regeneration by employing three dimensional scaffolds. This knowledge is fundamental to oral and maxillo-facial surgery, which uses different types of biomaterials, in particular for treating specific pathologies, such as jaw bone atrophies, periodontal defects and cystic lesions.

In this study, we have described the use of Saos-eGFP engineered cell lines employed for the preliminary *in vitro* characterization of cell morphology, spread and proliferation on biomaterials, and we have clinically demonstrated bone re-growth driven by the biomaterials tested herein. The coralline-HA biomaterials, tested with Saos-eGFP cells, showed good cyto-compatibility although some differences in proliferation activity was found as reported earlier [14]. This cellular model will allow in vivo testing only for those materials which have shown the minimal required *in vitro* properties for successful bone tissue regeneration: an absence of cyto-toxic effects and good adhesion, spread and proliferation capabilities. This study has demonstrated that human engineered osteoblast-like cells expressing the eGFP is a suitable cellular model to assay biomaterials. Saos-eGFP has the advantage to test biomaterials by measuring the emitted fluorescence instead to count each time the number of cells as usually performed with the traditional primary or transformed cell lines.

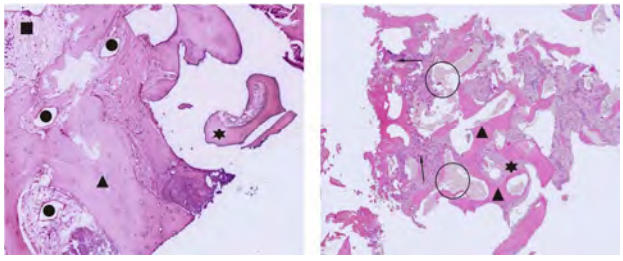

(a) (b)

**Figure 7. Histological evaluations indicate that tested biomaterial induces new bone formation, thus showing osteoconductive and osteoinductive properties. Patient 1 (a). Biopsy consist of cortical bone (▲) associated with new bone formation and fibro-osseous tissue (★). Areas of cortical (▲) and spongious bone (■) are both index of bone ingrowth together with neoangiogenetic processes demonstrated by vascular channels (●). Magnification 10x. Patient 2 (b). Black circles show exogenous material surrounded by mature cortical bone (▲) and fibro – osseous (★) tissue associated with macrophages and the infiltration of inflammatory cells (black arrows). Magnification 40x.**

## 5. Conclusions

In conclusion our cellular model reduces 1) the cost of

 

the experiments; 2) the time of the execution; 3) while giving the same kind of results obtained with other cellular models, as demonstrate herein in assaying the well characterized HA biomaterials [9-11,14].

## 6. Acknowledgements

This study was supported in part by grants to M.T and P.F.N. from the Ministero della Università e Ricerca, University of Ferrara and University of Verona. Italy.

Dr. Katia Campioni was supported by a post-doc fellowship of the Fondazione Cassa di Risparmio di Cento, Italy.

SEM analyses were carried out at the Centre of Electron Microscopy, University of Ferrara, Ferrara, Italy.

## REFERENCES

[1] J. A. Hubbell, "Bioactive Biomaterials," *Current Opinion in Biotechnology*, Vol. 10, No. 2, 1999, pp. 123-129.

[2] L. F. Reichardt, "Introduction: Extracellular Matrix Molecules. Guidebook to the Extracellular Matrix, Anchor, and Adhesion Proteins," Oxford University Press, New York, 1999, p. 335.

[3] E. H. Danen and A. Sonnenberg, "Integrins in Regulation of Tissue Development and Function," *The Journal of Pathology*, Vol. 201, No. 4, 2003, pp. 632-641.

[4] M. M. Sandberg and H. T. Aro, "Gene Expression during Bone Repair," *Clinical Orthopaedics and Related Research*, Vol. 289, 1993, pp. 292-312.

[5] T. T. Kon and J. Cho, "Expression of Osteoprotegerin, Receptor Activator of NF-kappaB Ligand (Osteoprotegerin Ligand) and Related Proinflammatory Cytokines During Fracture Healing," *Journal of Bone and Mineral Research*, Vol. 16, No. 6, 2001, pp. 1004-1014.

[6] J. R. Lieberman and A. Daluiski, "The Role of Growth Factors in the Repair of Bone. Biology and Clinical Applications." *Journal of Bone Joint and Surgery*, Vol. 84, No. A-6, 2002, pp. 1032-1044.

[7] D. M. Roy and S. K. Linnehan, "Hydroxyapatite Formed from Coral Skeletal Carbonate by Hydrothermal Exchange," *Nature*, Vol. 247, No. 438, 1974, pp. 220-222.

[8] A. R. Vaccaro, K. Chiba, *et al*., "Bone Grafting Alternatives in Spinal Surgery," *The Spine Journal*, Vol. 2, No. 3, 2002, pp. 206-215.

[9] O. Shamsuria, A. S. Fadilah, A. B. Asiah, M. R. Rodiah, A. H. Suzina and A. R. Samsudin "*In Vitro* Cytotoxicity Evaluation of Biomaterials on Human Osteoblast Cells CRL-1543; Hydroxyapatite, Natural Coral and Polyhydroxybutarate," *Medical Journal of Malaysia*, Vol. 59, Suppl. B, 2004, pp. 174-175.

[10] M. Barron, L. Franklin, J. Woodall Jr., S. Wingerter, H. Benghuzzi and M. Tucci, "Comparison of Osteoconductive Materials on MG63 Osteoblast Cell Function," *Biomedical Sciences Instrumentation*, Vol. 43, 2007, pp. 248-253.

[11] J. C. Fricain, J. Alouf, *et al*., "Cytocompatibility Study of Organic Matrix Extracted from Caribbean Coral Porites Astroides," *Biomaterials*, Vol. 23, No. 3, 2002, pp. 673-679.

[12] C. Morelli, G. Barbanti-Brodano, *et al*., "Cell Morphology, Markers, Spreading, and Proliferation on Orthopaedic Biomaterials. An Innovative Cellular Model for the *In Vitro* Study," *The Journal of Biomedical Materials Research*, Vol. 83, No. 1, 2007, pp. 178-183.

[13] M. Tognon, C. Morelli, *et al*., "A Novel Genetically Engineered Human Osteoblasts for the *in Vitro* Study of Biomaterials," In: N. Ashammakhi, R. Reis and F. Chiellini, Eds., *Topics in Tissue Engineering*, 2008, pp. 1-13.

[14] C.T. Begley, M. J. Doherty, D. P. Hankey and D. J. Wilson, "The Culture of Human Osteoblasts upon Bone Graft Substitutes," *Bone*, Vol. 14, No. 4, 1993, pp. 661-666.

 

*Journal of Biomaterials and Nanobiotechnology*, **2010, 1, 7-16**
doi:10.4236/jbnb.2010.11002 Published Online October 2010 (http://www.SciRP.org/journal/jbnb)

# Changes of Surface Composition and Morphology after Incorporation of Ions into Biomimetic Apatite Coating*

**Wei Xia[1,2*], Carl Lindahl[1,2], Cecilia Persson[1], Peter Thomsen[2,3], Jukka Lausmaa[2,4], Håkan Engqvist[1,2*]**

[1]Materials in Medicine, Applied Materials Science, the Ångstrom Laboratory, Uppsala University, Uppsala, Sweden; [2]BIOMATCELL, VINN Excellence Center of Biomaterials and Cell Therapy, Sweden; [3]Institute for Clinical Sciences, Sahlgrenska Academy at University of Gothenburg, Gothenburg, Sweden; [4]Department of Chemistry and Materials Technology, SP Technical Research Institute of Sweden, Borås, Sweden.
Email: {wei.xia, hakan.engqvist}@angstrom.uu.se

Received July 28th, 2010; revised August 19th, 2010; accepted September 20th, 2010.

## ABSTRACT

*Fabrication of trace elements incorporated apatite coating could combine the ions' pharmaceutical effect into the materials. In this study, strontium, silicon, and fluoride ions have been incorporated into apatite coatings through a biomineralization method, which mimics an in vitro mineralization process. The surface composition is tested with X-ray diffraction and X-ray photoelectron spectroscopy, and the surface morphology is characterized with scanning electron microscopy. Compared with pure hydroxyapatite coating, the strontium, silicon, and fluoride substituted apatite coatings show different morphology as spherical, needle-like, and nano-flake-like, individually. The crystal size of these biomimetic hydroxyapatite coatings decreased after ion substitution. The results of the analysis of surface composition present the ion substitutions are increased with the increasing of ion concentrations in the soaking solution. That means the ion incorporation into the apatite structure based on the biomineralization method could not only vary the ion content in but also change the morphology of the apatite coatings. Herein, the role of ion substitution is considered from the point of view of materials science at the micro structural and surface chemistry levels.*

***Keywords*: *Biomineralization, Hydroxyapatite, Coating, Substitution, Biomimetic***

## 1. Introduction

Surface composition and morphology are two key factors in implant coatings. The outermost layer of a biomaterial's surface possesses different properties depending on its elemental compositions and functionalities (such as $-PO_4$, -SiOH, -TiOH, -OH, -COOH, and $-NH_2$ groups). Bioactive silicate glasses could chemically bond with the bone tissue because they could form a SiOH layer on the surface in water solution and induce, further, the formation of hydroxyapatite [1]. Kokubo *et al*. reported the bioactivity and bone-bonding ability of titanium implants treated with an alkali hydroxide solution have been improved because of the existence of TiOH groups on the surface [2]. Surface topography also affects the bioactivity, biocompatibility, and tissue in-growth [3]. Osteoblast-like cells adhere more readily to and appear more differentiated on rough surfaces [3-5]. Recent studies report that surfaces with specific nano- and micro-topographies can improve the cell adhesion, change the cell spreading, and enhance the gene expression [6-8]. Therefore, the fabrication of bioactive materials presenting surfaces with these types of topographies is of great interest.

Hydroxyapatite (HA), $Ca_{10}(PO_4)_6(OH)_2$, a calcium phosphate found in bone and teeth, presents good osteoconductivity and osteoinductivity and is commonly used in dental and orthopedic surgery [9]. The high biocompatibility of HA has also led to its use as a coating material on metallic implants such as titanium, stainless steel and Co-Cr alloys [10-12]. However, the synthetic HA is still need to be improved. For example, it has been shown to induce apatite formation at a slower rate than other materials, such as silicate based bioactive glasses [13]. Furthermore, the low resorbability rate of synthetic, stoichiometric hydroxyapatite limits the rate of in-growth for new bone formation [14,15]. These factors may result in an increased risk of implant failure due to the deficient fixation.

 

A previous study has shown that the bioactivity and resorbability of hydroxyapatite can be improved by decreasing the crystallinity and introducing ion substitutions in its structure [16]. In fact, it is well known that natural bone mineral is a calcium deficient hydroxyapatite with low crystallinity. Various ionic substitutions, cationic as well as anionic, exist in bone mineral, such as Sr, Si, Mg, $CO_3^{2-}$ and F. Anions can be incorporated into the sites of $OH^-$ (type A) and $PO_4^{3-}$ (type B) [17], and cations can be incorporated into the sites $Ca^{2+}$ I and $Ca^{2+}$ II [18]. These ions also have important functions in the bone. For instance, a reduction in bone resorption and an increase in the mechanical strength may be obtained through Sr substitutions [19,20]. Silicon can increase the bone mineralization rate and enhance the osteopath proliferation, differentiation and collagen production [21]. Fluoride, which is good for teeth, can stabilize apatite and also stimulate the osteoblast activity [22,23]. Finally, previous research has shown that ion substituted apatite materials may improve the interaction between bone and synthetic apatite materials [24].

Methods to fabricate HA and ion substituted coatings include plasma spraying [25], sol-gel [26], magnetron co-sputtering [27], pulsed-laser deposition [28] and micro-arc oxidation techniques [29]. Although these techniques allow the preparation of HA coatings combined with a tailoring of the chemical composition, the draw- backs of synthetic HA have not been resolved. Recently, a solution method termed the biomineralization method has been used to fabricate biomimetic HA coatings on implants [3, 30-32]. This biomimetic method maintains low deposition temperatures and also provides a good surface coverage of complex geometrical shapes. The obtained coating is calcium deficient, not completely crystallized and the chemical composition can be tailored using different ions. *In vivo* studies show that this apatite coating provides faster new bone in-growth and coating resorbability in early bone formation [33]. However, a histological study found that rough titanium implants had a more positive effect on new bone formation than the biomimetic apatite coating [34].

In brief, there is room for improvement of this biomimetic coating in order to strengthen the implant and bone bonding and to have a stronger positive effect on new bone formation. Previous work suggests that the surface composition and the topography of the coatings are key parameters affecting the bioactivity, biocompatibility, and further material/tissue interactions such as tissue ingrowth. In this work, we prepared ion substituted (Sr, Si, F) apatite (*i*HA) coatings with varied compositions and surface morphology on pre-treated titanium substrates through a biomineralization method.

## 2. Materials and Methods

### 2.1. Materials

Pure titanium (Grade 2, 99.4% pure, Edstraco AB, Sweden) cut as squares (10x10mm, with a 1mm thickness) was used as a substrate for the biomimetic coatings. The base soaking medium was phosphate buffer solution (Dulbecco's PBS, Aldrich, USA). The ion composition of this PBS is: $Na^+$ (145mM), $K^+$ (4.3mM), $Mg^{2+}$ (0.49mM), $Ca^{2+}$ (0.91mM), $Cl^-$ (143mM), and $HPO_4^{2-}$ (9.6mM).

### 2.2. Surface Treatment

Crystalline titanium dioxides have been proven to strengthen the physical–chemical bonding between the implants and living bones because of their ability to induce a bone-like apatite in the body's environment [35]. Therefore, such oxidized Ti surface could be considered as a good transition layer on the Ti-based implant's surface. In this study, a titanium oxide layer was created on the titanium plates in the form of a rutile film via a thermal oxidation process. Ti plates were treated at 800℃ for 1 hour with a ramping rate of 5℃/min. Thereafter the plates were treated with an alkaline solution (1M NaOH) and ethanol in an ultrasonic bath before use.

### 2.3. Biomimetic Ion Substituted Apatite Coating Deposition

The preparation of the biomimetic ion substituted apatite coating was performed in an ion modified PBS solution. The initial pH value is 7.4 adjusted by NaOH and HCl solutions. In order to investigate, which factors that influence the biomimetic coating deposition, a series of ion concentrations and soaking times were studied. Sr, Si and F ion concentrations were varied between 0.06mM and 0.6 mM, 0.075 mM and 0.15 mM, 0.04 mM and 0.2 mM, respectively, and soaking time from 12 hours to 2 weeks. The maximum concentrations used for the different ions were limited by the precipitation of the same at higher concentrations. All specimens were soaked in 40 ml preheated solution in sealed plastic bottles, which were then stored in an oven at 37℃. The solution was exchanged every 3 days to avoid depletion of calcium and phosphate ions. All samples were rinsed with de-ionized water and dried at 37℃ prior to characterization.

### 2.4. Morphological and Chemical Characterization

The morphology of the specimens before and after coating was evaluated using field emission scanning electron microscopy (FE-SEM, LEO 1550). An SE2 detector was used with an accelerating voltage of 10 kV. The crystallinity of the specimens was analyzed using X-ray

 

diffractometry (TF-XRD, Siemens Diffractometer 5000) using Cu Ka radiation (k = 1.5418 Å). The diffractometer was operated at 45 kV and 40 mA at a 2 h range of 10–80°, with a fixed incidence angle of 1°. The chemical composition was analyzed by X-ray photoelectron spectroscopy (XPS, Physical Electronics Quantum 2000, Al Kα X-ray source).

### 2.5. Estimation of Crystal size and Crystallinity

This estimation method was referred from Li *et al* [18]. The size of HA and Sr, Si and F-HA crystals were calculated from XRD data using the Scherrer equation. The peak of (002) was fit to define the full width at half maximum intensity (FWHM):

$$d = \frac{k\lambda}{FWHM \bullet \cos\theta} \quad (1)$$

Where d is the crystal size, λ is the wavelength of Cu $K_\alpha$ radiation (λ = 1.5418Å), and k is the broadening constant varying with crystal habit and chosen as 0.9 for the elongated apatite crystallites.

$X_c$, the crystallinity, corresponds to the fraction of crystalline apatite phase in the investigated volume of powdered samples. An empirical relation between $X_c$ and the FWHM was deduced, according to the equation:

$$X_c = \left(\frac{K_A}{FWHM}\right)^3 \quad (2)$$

Where $X_c$ is the crystallinity degree, $K_A$ is a constant set at 0.24.

## 3. Resutls

**Figure 1** shows the SEM images of hydroxyapatite (HA)

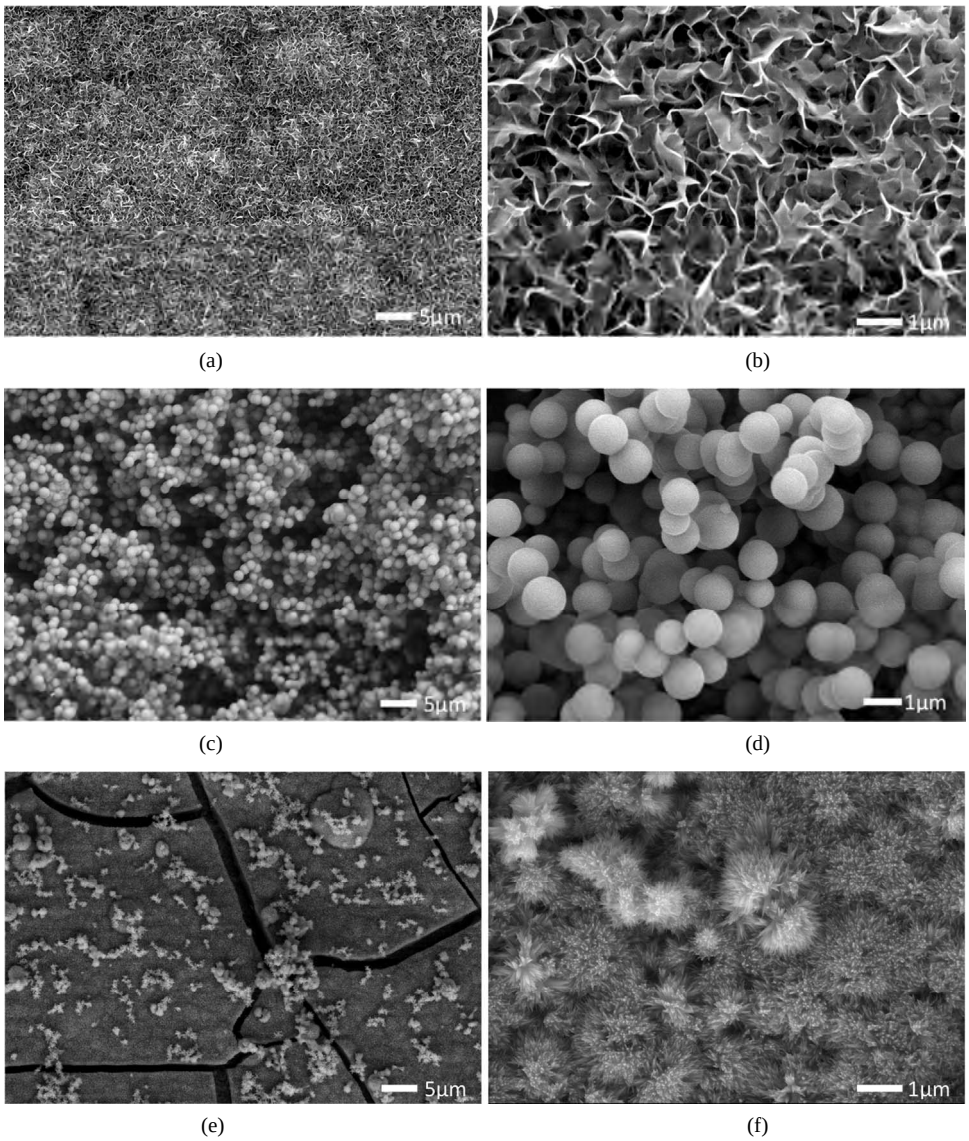


(a) (b)

(c) (d)

(e) (f)

 

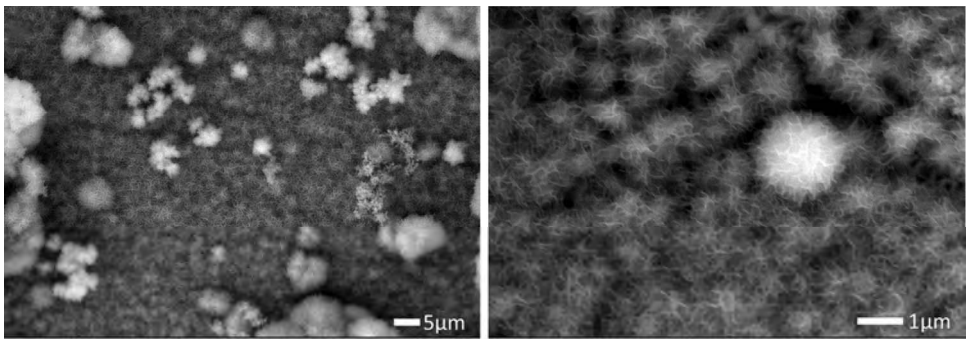


(g) (h)

**Figure 1. Surface morphology of the $TiO_2$/Ti substrates after soaking for 2 weeks in PBS containing different ion concentrations. (a) and (b) no additional ion doped, (c) and (d) 0.6 mM strontium ion doped, (e) and (f) 0.2 mM fluoride ion doped, (g) and (h) 0.15 mM silicate ion doped.**

without substituted ions, strontium substituted hydroxylapatite (Sr-HA), fluoride substituted hydroxyapatite (F-HA) and silicon substituted hydroxyapatite (Si-HA) coatings on $TiO_2$/Ti substrates after soaking in PBS for 2 weeks. It is clear that the morphology strongly depends on the substituted ions. For the pure HA coating (**Figure 1 (a)** and **(b)**), it is flake-like, with flakes of approximately 100 nm-1 μm in length and width. The Sr-HA coating (**Figure 1 (c)** and **(d)**) has an entirely different morphology with sphere-like particles of approximately 200-800 nm diameter. For the F-HA coating (**Figure 1 (e)** and **(f)**), the morphology was again different, presenting a needle-like structure. The morphology of the Si-HA coating (**Figure 1 (g)** and **(h)**) was relatively similar to the pure HA coating. It was also flake-like, but the size of the Si-HA particles was much smaller than pure HA; less than 100 nm in length and width. The XRD analysis (**Figure 2**) showed diffraction peaks of apatite in all cases, asdetected around 31º related to the overlapping of planes (211), (112), and (300), and around 26° related to plane (002).

In order to study the influence of the ion concentration on the structure of the HA coating, the results of using lower concentrations of Sr (0.06 mM), Si (0.075 mM) and F (0.02 mM) ions are shown in **Figure 3**. It can be seen that the morphology of the Sr-HA coating still appears sphere-like, although the interface is rougher, porous and with a wider size distribution. However, the decrease in Si and F ion concentration did not greatly affect the morphology of F-HA and Si-HA coatings (**Figure 3 (b)** and **(c)**). The F-HA coating was still needle-like, and the Si-HA coating was flake-like with nano-sized particles.

The early formation of the HA coatings, after soaking in PBS for 12 hours, is shown in **Figure 4**. All specimens were soaked in the high concentration ion doped PBS solution. It can be seen that the early Sr-HA coating (**Figure 4 (a)**) is a flat layer which is different to the morphology of the coating after soaking for 2 weeks. A few spherical nano-particles have formed on this early layer. These spherical nanoparticles could be considered to be the base of the formation of the second spherical Sr-HA layer. Herein the Sr-HA coating prepared using the biomineralization method is not a simple layer but a hierarchical coating with a gradient structure from a flat and dense early layer to a spherical and porous layer. The early F-HA coating (**Figure 4 (b)**) grows from the substrate with needle-like particles. There seems to be no hierarchical structure in the F-HA coating. The early formation of the Si-HA coating (**Figure 4 (c)**) shows a nano-sized flake-like layer on the substrate. Again, the structure is similar to the final structure after 2 weeks of soaking.

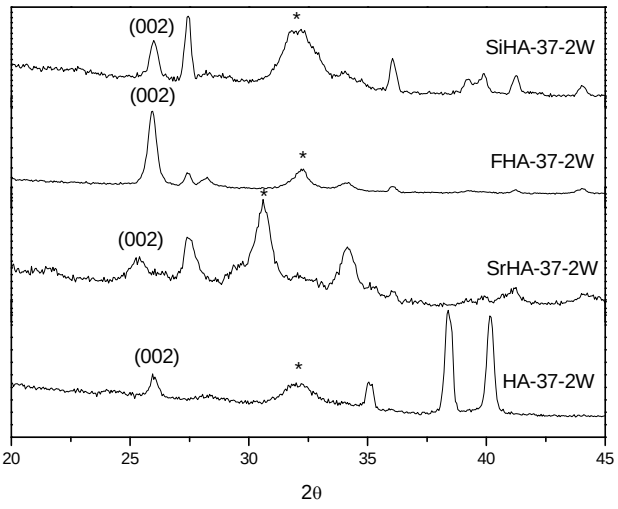


**Figure 2. XRD patterns of the HA coatings with and without ion substitution. * and (002): HA. The substrates have been soaked in pure, Sr (0.6 mM), F (0.2 mM) and Si (0.15 mM) PBS for 2 weeks.**

 

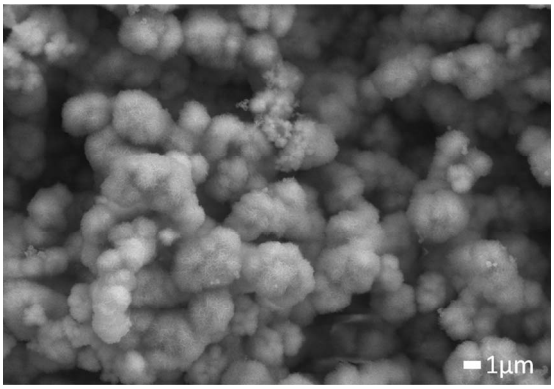


(a)

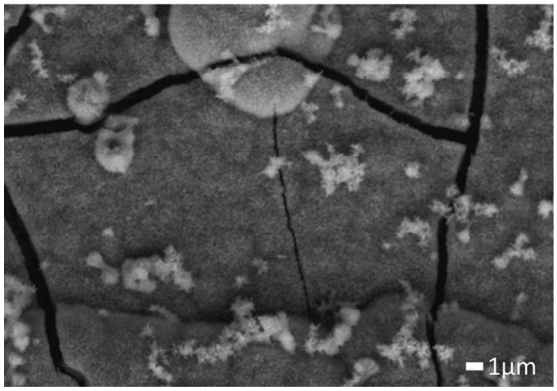


(b)

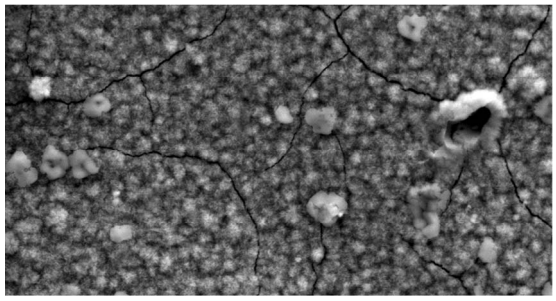

(c)

**Figure 3. Surface morphology of the TiO2/Ti substrates after soaking for 2 weeks in the lower concentration solutions. (a) 0.06 mM strontium ion doped, (b) 0.04 mM fluoride ion doped, (c) 0.075 mM silicate ion doped.**

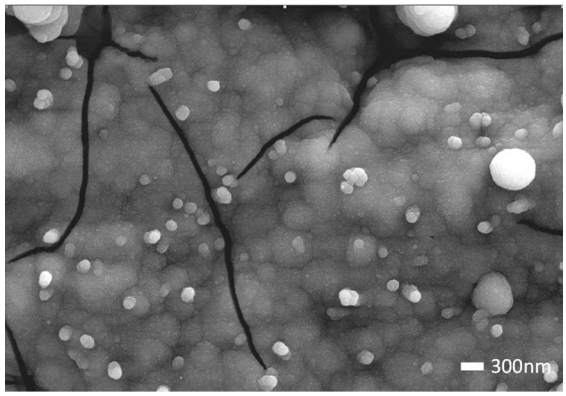


(a)

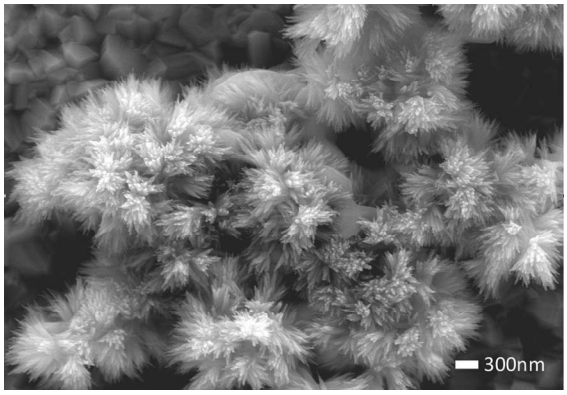


(b)

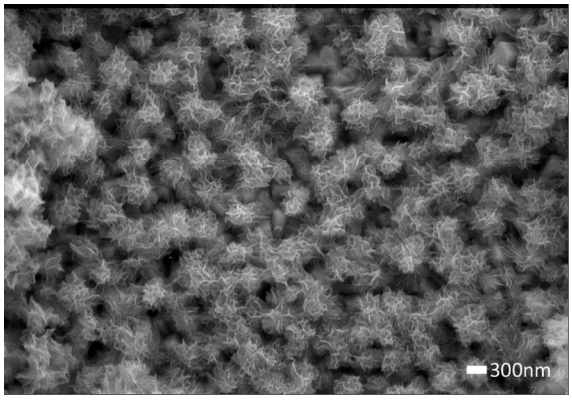


(c)

**Figure 4. Early growth of ion substituted HA coatings after soaking for 12 hours. (a) strontium (0.6 mM) substituted HA, (b) fluoride (0.2 mM) substituted HA, (c) silicate (0.15 mM) substituted HA.**

The changes of crystal size and crystallinity of different apatite coating reflected from the XRD patterns were calculated in order to observe the influence of the Sr, Si and F ions. The (002) reflection was chosen to evaluate the average crystal size because this peak was well resolved and showed no interferences. The $d_{002}$ of HA, SrHA, FHA and SiHA were 35.58, 16.27, 25.10 and 25.45nm, respectively. The crystal size decreased significantly when hydroxyapatite had been substituted strontium, fluoride and silicon ions. The crystallinity of all HA and Sr, F, and Si substituted HA coatings were very low, just 0.0185, 0.0199, 0.0186 and 0.0185, respectively. That means all of these biomimetic coatings were poor crystallized.XPS survey spectra identified calcium, phosphorus, oxygen, strontium, fluoride and silicon as themajor constituents of the strontium, fluoride and silicon substituted apatite coating on titanium plates, as expected, seeing **Figure 5**. All of these spectrums

 

were for the sample prepared at 37℃ for 2 weeks using the higher ion concentration. The peak at 134ev (**Figure 5 (a)**) was an overlap of Sr3*d* and P2*p* because Sr3$d_{5/2}$ (133 ± 0.5 eV), Sr3$d_{3/2}$ (135 ± 0.5 eV), P2*p* (132 - 133 eV) lines were closely located. The peak at 684ev (**Figure 5 (b)**) was F1*s*. The weak peak 153ev (**Figure 5 (c)**) was Si2*s*. Si2*p* (~99ev) could not be clearly observed. **Table 1** gives the atomic ratio of the ions in the coatings, obtained from XPS. It can be noted that the composition of the coatings can be varied by changing the ion concentrations in the soaking medium. When the Sr concentration was increased from 0.06 mM to 0.6 mM, the Sr content in the newly formed biomimetic coating increased from 3.56% to 7.74%. The F content in the coating increased from 1.24% to 1.53% after the concentration in PBS was increased from 0.04 mM to 0.2 mM. For the lower Si concentration (0.075 mM), no data was available from the XPS. After the Si concentration was increased to 0.15 mM, 0.56% silicon was found in the coating.

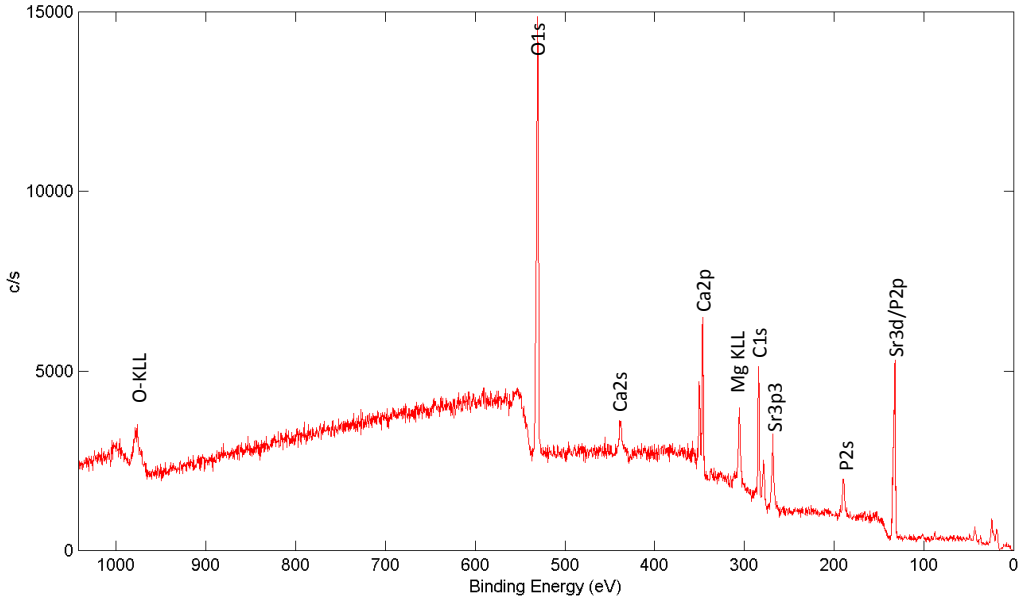


(a)

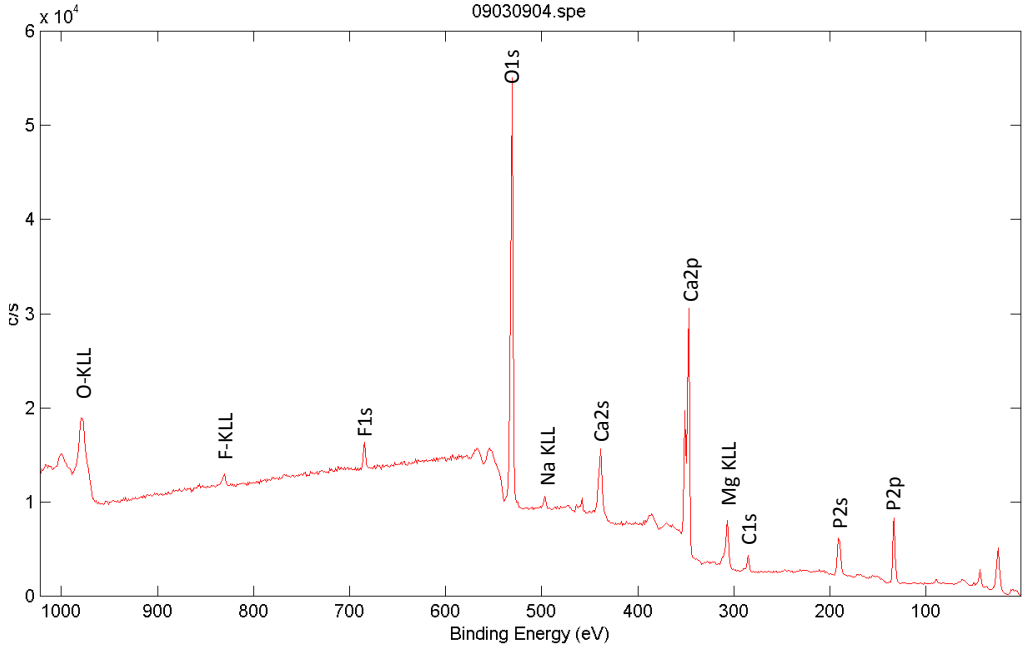


(b)

 

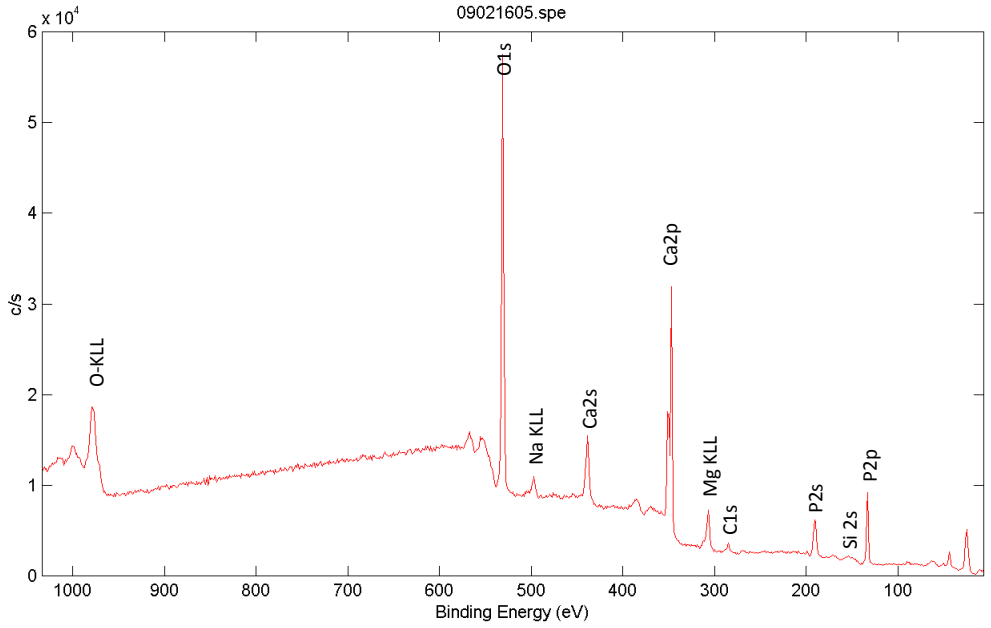


(c)

**Figure 5. XPS spectra for strontium (a), fluoride (b), and silicon (c) substituted apatite coating on titanium plates (37℃ for 2 week).**

**Table 1. Preparation parameters and atomic concentrations of the final coatings. (Error in brackets).**

| Samples | Ion concentration mM | Temperature ℃ | Time week | Substituted ion % of final coating |
|---|---|---|---|---|
| 006SrPBS-37-2W | 0.06 | 37 | 2 | 3.56 (1.01) |
| 06SrPBS-37-2W | 0.6 | 37 | 2 | 7.74 (1.53) |
| 004FPBS-37-2W | 0.04 | 37 | 2 | 1.24 (0.24) |
| 02FPBS-37-2W | 0.2 | 37 | 2 | 1.53 (0.11) |
| 0075SiPBS-37-2W | 0.075 | 37 | 2 | - |
| 015SiPBS-37-2W | 0.15 | 37 | 2 | 0.56 (0.16) |

## 4. Discussions

In this study it was shown that the topography of hydroxyapatite coatings obtained using a biomineralization method can be varied by adding different ions of varied concentrations to the soaking medium. **Figure 6** gives a schematic illustration of ion substituted hydroxyapatite coatings with different morphologies on the $TiO_2$/Ti substrates. The non substituted hydroxyapatite coating was composed of flake-like particles in the order of microns. After some of the calcium ions had been replaced by strontium ions, the flake-like coating transformed into a spherical coating with a transitional flat layer. When the $OH^-$ ions were partially replaced by F ions, the new coating had a needle-like morphology. This is very similar to the morphology of tooth enamel [36]. Hydroxyapatite incorporated with fluoride in enamel presents needle-like nanocrystals in highly ordered bundles. Compared with the Sr and F substituted hydroxyapatite coatings, Si substituted hydroxyapatite coating showed a similar morphology to pure hydroxyapatite coating. However, the particle size decreased, from the micrometer to the nanometer scale. These results are different to previously reported HA coatings prepared with solution methods, especially for the Sr-HA and the F-HA coatings [37,38]. Li *et al.* [37] reported on a solution-derived strontium doped apatite coating where the morphology was similar to pure apatite coating even though the strontium concentration reached 1.5 mM. However, in our study the morphology of the Sr-HA coating was completely different to the pure HA coating, even at concentrations as low as 0,06mM Sr. Also, a higher concentration of strontium ions seemed to facilitate the formation of more

 

spherical particles. Wang *et al*. [38] prepared a F-HA coating using an electrochemical deposition method. They reported that the obtained F-HA particles became sharper and smaller when the F concentration increased in the solution. At certain F concentrations, they could get spindle-like F-HA. Needle-like F-HA exists naturally in tooth enamel [36]. In this study, a well organized needle-like FHA coating was obtained via a mineralization method without an inductor. **Table 2** shows a decrease of the crystal size after hydroxyapatite had been substituted. This reduction in the crystal size of synthetic ion substituted hydroxyapatite was also reported by Li *et al* [18]. The poor crystallinity of the biomimetic coatings has been also reported Bracci and Bigi *et al* [39].

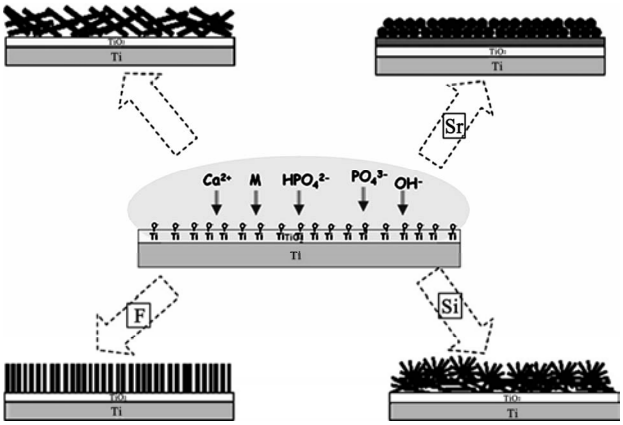


**Figure 6. Schematic illustration of ion substituted hydroxyapatite coatings with different morphology on the TiO2/Ti substrates.**

**Table 2. Crystal size and crystallinity of HA, SrHA, SiHA and FHA reflected by XRD patterns.**

| Sample | Line width (002) FWHM (2θ) | Average crystal size d (nm) | Crystallinity ($X_c$) |
|---|---|---|---|
| HA-37-2W | 25.9963 | 35.58 | 0.0185 |
| SrHA-37-2W | 25.3722 | 16.27 | 0.199 |
| FHA-37-2W | 25.9395 | 25.10 | 0.0186 |
| SiHA-37-2W | 26.0015 | 25.45 | 0.0185 |

XPS analysis showed that the ion concentration in the soaking solution also influenced the amount of ions substituted into the HA. A higher ion concentration tended to give a higher amount of substituted ions. However, the substitutions we obtained may not be the highest possible substitutions of these ions in hydroxyapatite since, in order to avoid an initial precipitation in PBS solution, higher concentrations of Sr, F and Si ions could not be used. Furthermore, from **Table 1** it can be noted that the amount of substituted ions was highest using strontium, followed by fluoride and finally silicon. This could be due to the differences in initial concentrations of the ions. However, because of the similarity in radius between $Sr^{2+}$ and $Ca^{2+}$ and $F^-$ and $OH^-$, respectively, the replacement of calcium and hydroxide ions by strontium and fluoride ions is also easier than substituting phosphate by silicate. Since the latter molecules are not single ions they are more difficult to incorporate into hydroxyapatite. Finally, one hydroxyapatite molecule has 10 calcium ions and 2 hydroxide ions. This could allow for more Sr than F substitutions. The resorption rate and the cell response of these ion substituted hydroxyapatite coatings remain to be evaluated and may be of interest for future studies.

## 5. Conclusions

A simple method for the preparation of ion substituted hydroxyapatite coatings with controlled topography and composition was explored in this study. The results showed that the surface structure could be modified by substituting different ions into the apatite structure. The strontium, fluoride and silicon substituted hydroxyapatite coatings gave spherical, needle-like, and nano-flake-like morphologies which were very different to pure hydroxyapatite. The concentration of strontium ions was also found to affect the morphology of the coatings. The lower Sr concentration resulted in irregular and porous spherical particles and the higher one resulted in regular spherical particles. For the fluoride and silicon substituted coatings, there was no obvious difference between a high ion concentration and a low one. After ion substitution, the biomimetic hydroxyapatite coatings showed a poor crystallinity, and crystal size decreased. XPS analysis showed that the atomic concentration of ions in the final coating was affected by the ion concentration in the PBS solution. A high ion concentration could result in higher amounts of substitutions. The surface composition analysis also showed that the highest amount of substitutions was achieved using strontium ions, followed by the fluoride ions and finally the silicon ions. In summary, the surface composition and morphology of hydroxyapatite produced via a biomineralization method can be controlled using ion substitutions.

## 6. Acknowledgement

This work was supported by BIOMATCELL, VINN Excellence Center of Biomaterials and Cell Therapy.

## REFERENCES

[1] L. L. Hench, "Bioceramics: From Concept to Clinic," *Journal of the American Ceramic Society*, Vol. 74, No. 7,

 

July 1991, pp. 1487-1510.

[2] T. Kokubo, "Bioceramics and Their Clinical Applications," CRC Press, USA, 2008.

[3] J. E. Ellingsen and S. P. Lyngstadaas, "Bio-Implant Interface: Improving Biomaterials and Tissue Reactions" CRC Press, USA, 2003.

[4] R. Batzer, Y. Liu, D. L. Cochran, S. Szmuckler-Moncler, D. D. Dean, B. D. Boyan and Z. Schwartz, "Prostaglandins Mediate the Effects of Titanium Surface Roughness on MG63 Osteoblast-Like Cells and Alter Cell Responsiveness to 1 Alpha,25-$(OH)_2D_3$," *The Journal of Biomedical Materials Research*, Vol. 41, No. 3, September 1998, pp. 489-496.

[5] C. H. Lohmann, J. R. Sagun, V. L. Sylvia, D. L. Cochran, D. D. Dean, B. D. Boyan and Z. Schwartz, "Surface Roughness Modulates the Response of MG63 Osteoblast-Like Cells to 1,25-(OH)(2)D(3) Through Regulation of Phospholipase A(2) Activity and Activation of Protein Kinase A," *The Journal of Biomedical Materials Research*, Vol. 47, No. 2, November 1999, pp. 139-151.

[6] A. S. G. Curtis, "Small is Beautiful but Samller is the Aim: Review of a Life of Research," *Europe Cell & Mater*, Vol. 8, No. 22, October 2004, pp. 27-36.

[7] A. S. G. Curtis and P. Clark, "The Effect of Topographic and Mechanical Properties of Materials on Cell Behaviour," *Critical Reviews in Biocompatibility*, Vol. 5, 1990, pp. 343-362.

[8] L. Chou, J. D. Firth, V.-J. Uitto and D. M. Brunette, "Substratum Surface Topography Alters Cell Shape and Regulates Fibronectin mRNA level MRNA Stability Secretion and Assembly in Human Fibroblastes," *Journal of Cell Science*, Vol. 108, April 1995, pp. 1563-1573.

[9] M. Vallet-Regí, "Ceramics for Medical Applications," *Journal of Chemical Society, Dalton Transactions*, 2001, pp. 97-108.

[10] F. H. Lin, Y. S. Hsu, S. H. Lin and J. S. Sun, "The Effect of Ca/P Concentration and Temperature of Simulated Body Fluid on the Growth of Hydroxyapatite Coating on Alkali-Treated 316L Stainless Steel," *Biomaterials*, Vol. 23, No. 19, October 2002, pp. 4029-4038.

[11] X. Liu, P. Chu and C. X. Ding, "Surface Modification of Titanium, Titanium Alloys, and Related Materials for Biomedical Application," *Materials Sciences and Engineering Report*, Vol. 47, No. 3-4, December 2004, pp. 49-121.

[12] L. Sun, C. C. Berndt, K. A. Gross and A. Kucuk, "Material Fundamentals and Clinical Performance of Plasma-Sprayed Hydroxyapatite Coatings: A Review," *The Journal of Biomedical Materials Research*, Vol. 58, No. 5, 2001, pp. 570-592.

[13] H. Oonishi, L. Hench, J. Wilson, F. Sugihara, E. Tsuji, M. Matsuura, S. Kin, T. Yamamoto and S. Mizokawa, "Quantitative Comparison of Bone Growth Behavior in Granules of Bioglass, A-W Glass-Ceramic, and Hydroxyapatite," *The Journal of Biomedical Materials Research*, Vol. 51, No. 1, July 2000, pp. 37-46.

[14] D. Knaack, M. E. P. Goad, M. Aiolova, C. Rey, A. Tofighi, P. Chakravarthy and D. D. Lee, "Resorbable Calcium Phosphate Bone Substitute," *The Journal of Biomedical Materials Research*, Vol. 43, No. 4, 1998, pp. 399-409.

[15] C. P. A. T. Klein, A. A. Driessen, K. d. Groot and V. D. Hoof, "Biodegradation Behavior of Various Calcium Phosphate Materials in Bone Tissue," *The Journal of Biomedical Materials Research*, Vol. 17, No. 5, September 1983, pp. 769-784.

[16] C. Ergun, T. J. Webster, R. Bizios and R. H. Doremus, "Hydroxylapatite with Substituted Magnesium, Zinc, Cadmium, and Yttrium. I. Structure and Microstructure," *The Journal of Biomedical Materials Research Part A*, Vol. 59, No. 2, February 2002, pp. 305-311.

[17] R. A. Young and P. E. Mackie, "Crystallography of Human Tooth Enamel: Initial Structure Refinement," *Materials Research Bulletin*, Vol. 15, No. 1, January 1980, pp. 17-29.

[18] Z. Y. Li, W. M. Lam, C. Yang, B. Xu, G. X. Ni, S. A. Abbah, K. M. C. Cheung, K. D. K. Luk and W. W. Lu, Chemical Composition, Crystal Size and Lattice Structural Changes after Incorporation of Strontium into Biomimetic Apatite," *Biomaterials*, Vol. 28, No. 7, March 2007, pp. 1452- 1460.

[19] E. Canalis, M. Hott, P. Deloffre, Y. Tsouderos and P. J. Marie, "The divalent Strontium Salt S12911 Enhances Bone Cell Replication and Bone Formation *in vitro*," *Bone*, Vol. 18, No. 6, June 1996, pp. 517-523.

[20] J. Christoffersen, M. R. Christoffersen, N. Kolthoff and O. Barenholdt, "Effects of Strontium Ions on Growth and Dissolution of Hydroxyapatite and on Bone Mineral Detection," *Bone*, Vol. 20, No. 1, January 1997, pp. 47-54.

[21] A. M. Pietak, J. W. Reid, M. J. Stott and M. Sayer, "Silicon substitution in the Calcium Phosphate Bioceramics," *Biomaterials*, Vol. 28, No. 28, October 2007, pp. 4023-4032.

[22] C. Robinson, R. C. Shore, S. J. Brookes, S. Strafford, S. R. Wood and J. Kirkham, "The Chemistry of Enamel Caries," *Critical Reviews in Oral Biology and Medicine*, Vol. 11, No. 4, 2000, pp. 481-495.

[23] Y. Wang, S. Zhang, X. Zeng, L. L. Ma, W. Weng, W. Yan and M. Qian, "Osteoblastic Cell Response on Fluoridated Hydroxyapatite Coatings," *Acta Biomater*, Vol. 3, No. 2, March 2007, pp. 191-197.

[24] E. Zhang and C. Zou, "Porous Titanium and Silicon-Substituted Hydroxyapatite Biomodification Prepared by a Biomimetic Process: Characterization and *In vivo* Evaluation," *Acta Biomater*, Vol. 5, No. 5, June 2009, pp. 1732-1741.

[25] W. Xue, H. L. Hosick, A. Bandyopadhyay, S. Bose, C. Ding, K. D. K. Luk, K. M. C. Cheung and W. W. Lue, "Preparation and Cell–Materials Interactions of Plasma Sprayed Strontium-Containing Hydroxyapatite Coating," *Surface & Coatings Technology*, Vol. 201, No. 8, January 2007, pp. 4685-4693.

[26] G. Qi, S. Zhang, K. A. Khora, W. Weng, X. Zeng and C. Liu, "An Interfacial Study of Sol–Gel-Derived Magne-

 

sium Apatite Coatings on Ti6Al4V Substrates," *Thin Solid Films*, Vol. 516, No. 16, June 2008, pp. 5172-5175.

[27] E. S. Thian, J. Huang, S. M. Best, Z. H. Barber and W. Bonfield, "Novel Silicon-Doped Hydroxyapatite (Si-HA) for Biomedical Coatings: An *In vitro* Study Using Acellular Simulated Body Fluid," *The Journal of Biomedical Materials Research Part B*: *Appl Biomater*, Vol. 76, No. 2, February 2006, pp. 326-333.

[28] E. L. Solla, P. Gonzalez, J. Serra, S. Chiussi, B. Leon and J. G. Lopez, "Pulsed Laser Deposition of Silicon Substituted Hydroxyapatite Coatings from Synthetical and Biological Sources," *Applied Surface Science*, Vol. 254, No. 4, December 2007, pp. 1189-1193.

[29] Y. Han, D. H. Chen and L. Zhang, "Nanocrystallized SrHA/SrHA–$SrTiO_3$/$SrTiO_3$–$TiO_2$ Multilayer Coatings Formed by Micro-Arc Oxidation for Photocatalytic Application," *Nanotechnology*, Vol. 19, No. 33, July 2008, pp. 335-705.

[30] H. B. Wen, J. R. D. Wijin, F. Z. Cui and K. D. Groot, "Preparation of Calcium Phosphate Caotings on Titanium Implant Materials by Simple Chemistry," *The Journal of Biomedical Materials Research*, Vol. 41, No. 2, Auguest 1998, pp. 227-236.

[31] J. Forsgren, F. Svahn, T. Jarmar and H. Engqvist, "Formation and Adhesion of Biomimetic Hydroxyapatite Deposited on Titanium Substrates," *Acta Biomaterialia*, Vol. 3, No. 6, November 2007, pp. 980-984.

[32] W. Xia, C. Lindahl, J. Lausmaa, P. Borchardt, A. Ballo, P. Thomsen and H. Engqvist, "Biomineralized Strontium Substituted Apatite/Titanium Dioxide Coating on Titanium Surfaces," *Acta Biomaterialia*, Vol. 6, No. 4, April 2010, pp. 1591-1600.

[33] D. V. Vasudev, J. L. Ricci, C. Sabatino, P. J. Li and J. R. Parsons, "*In vivo* Evaluation of a Biomimetic Apatite Coating Grown on Titanium Surfaces," *The Journal of Biomedical Materials Research Part A*, Vol. 69, No. 4, June 2004, pp. 629-636.

[34] F. He, G. Yang, X. Wang and S. Zhao, "Bone Responses to Rough Titanium Implants Coated with Bjiomimetic Ca-P in Rabbit Tibia," *The Journal of Biomedical Materials Research Part B*, Vol. 90, No. 2, August 2009, pp. 857-863.

[35] R. Hazan, R. Brener and U. Orun, "Bone-Growth to Metal Implants is Regulated by Their Surface Chemical Properties," *Biomaterials*, Vol. 14, No. 8, July 1993, pp. 570-574.

[36] A. Boyde, "Microstructure of Enamel," *Ciba doundation symposium* 205- *dental enamel*, John Wiley & Sons, New York, 1997.

[37] A. L. Oliveira, R. L. Reis and P. Li, "Strontium-Substituted Apatite Coating Grown on Ti6Al4V Substrate through Biomimetic Synthesis," *The Journal of Biomedical Materials Research Part B*, Vol. 83, No. 1, October 2007, pp. 258-265.

[38] J. Wang, Y. Chao, Q. Wan, Z. Zhu and H. Yu, "Fluoridated Hydroxyapatite Coatings on Titanium Obtained by Electrochemical Deposition," *Acta Biomaterialia*, Vol. 5, No. 5, June 2009, pp. 1798-1807.

[39] B. Bracci, P. Torricelli, S. Panzavolta, E. Boanini, R. Giardino and A. Bigi, "Effect of $Mg^{2+}$, $Sr^{2+}$, and $Mn^{2+}$ on the Chemico-Physical and *in vitro* Biological Properties of Calcium Phosphate Biomimetic Coatings," *Journal of Inorganic Biochemistry*, Vol. 103, No. 12, December 2009, pp. 1666-1674.

 

*Journal of Biomaterials and Nanobiotechnology*, **2010, 1, 17-30**
doi:10.4236/jbnb.2010.11003 Published Online October 2010 (http://www.SciRP.org/journal/jbnb)

# Water—A Key Substance to Comprehension of Stimuli-Responsive Hydrated Reticular Systems*

**Miloslav Milichovsky**

Department of Wood, Pulp and Paper, University of Pardubice, Faculty of Chemical Technology, Pardubice, Czech Republic.
Email: miloslav.milichovsky@upce.cz

Received August 3rd, 2010; revised August 24th, 2010; accepted September 20th, 2010.

## ABSTRACT

*Thermo-responsive hydrated macro-, micro- and submicro-reticular systems* (*TRHRS*), *particularly polymers forming hydrogels or similar networks, have attracted extensive interest because comprise biomaterials, smart or intelligent materials. Phase transition temperature* (*LCST or UCST, i.e. low or upper critical solution temperature, respectively*) *at about the TRHRS exhibiting a unique hydration-dehydration change is a typical characteristic. The characterization and division of the TRHRS are described followed by explanation of their behaviour. The presented original explanation is based on merely combination of basic thermodynamical state of individual useful macromolecule chains* (*long-chain or coil*) *with inter- and intra-mutual action of attractive and repulsive intramolecular hydration forces among them being strongly dependent upon temperature. Acquainted with this piece of knowledge, a theoretical concept of really biological systems movement, e.g. muscle tissues or artificial muscle etc., can be formulated.*

***Keywords*****:** *Thermally Responsive Materials, Hydrogels, Hydration Forces, Volume Phase Transition*

## 1. Introduction

Stimuli-responsive polymers – so-called smart polymers – have attracted great interest in academic and applied science recently. Most commonly, approaches take advantage of thermally induced, reversible phase transitions. In this context, polymers forming hydrated reticular systems found great interest. Hydrated reticular systems, *i.e.* networks in water environment, feature all of bio-objects and the products of their existence. We can identify these structures in nano- (submicro-), micro- and macro-scale as submicro-, micro- and macro-reticular hydrated systems, respectively. Supramolecular and hypermolecular structures are typical, e.g. the hydrogels on peptide basis and fibre-networks on cellulosic basis.

Hydrogels consist of elastic networks that can uptake as much as 90–99% w/w of water in their interstitial space. Hydrogels have high water content and a soft and rubbery consistency. Such systems have been especially focused in the biomedical area as they provide adequate semiwet three-dimensional environment for cells and tissue interaction and they can be combined with biological or therapeutic molecules. They can be also chemically controlled and designed to tailor their mechanical and functional properties [1-3]. Therefore hydrogels have been proposed for a series of biomedical and biological applications, including tissue engineering [3,4], drug release systems [5-9], biological sensors [12-14], temperature and light-responsive films [15] or tuneable hydrogel photonic crystals as optical sensors [16]. The most common hydrogels are the ones obtained by chemical crosslinking of hydrophilic macromolecules. Such linkages prevent the dissolution of the material but water can penetrate within the structure, causing the swelling of the structure without disrupting the mechanical and geometrical integrity of the structure. If the macromolecules composing the network react with some external variable, e.g. temperature, switching between a stretched to a squeezed states then the corresponding hydrogel could reversible swell and deswell in response to this stimulus. Such smart hydrogels have been proposed for a series of biomedical applications [17,18], not only in the delivery of therapeutic agents [5-9], but also in tissue engineering [10,11], intelligent microfluidic switching [19-21], sensors/diagnostic devices [22,23] and actuators [24,25].

For these purposes predominantly the recent new surface techniques are utilised. These smart designs are mostly based on stimuli-responsive materials forming self-assembled monolayers and polymer films. Methods such as spin coating, chemical vapour deposition, laser

*This work was supported by the Ministry of Education, Youth and Sports of the Czech Republic under the Research Project MSM0021627501.

 

ablation, plasma deposition and chemical or electrochemical reactions have been widely applied to the fabrication of thin polymer films [26]. Further utilisation of the effect of external temperature stimuli was already demonstrated in several applications of nanometre-thick poly(N-isopropylacrylamide) (PNIPAAm)-grafted surfaces for separation processes [27-38] including gel permeation chromatography [33], size exclusion chromatography [36] and aqueous chromatography [27-30,37] inclusive high performance liquid chromatography (HPLC) [31,33-36]. In most of these applications, the packing material is modified with PNIPAAm to change the property of the stationary of the column in response to alteration of temperature.

The most peculiar property of these systems, however, is probably their stimuli-responsive behaviour. The thermo-responsive behaviour is typical but only for hydrogels because fibre-networks are composed of high consistency hydrogel fibres distributed in macro-space of water environment. Thermo-responsive hydrogels undergo a phase transition in response to temperature changes. Up to now, almost all of the thermo-responsive hydrogels have been featured with negatively thermo- responsive volume phase transition, *i.e.* with the existence of a lower-critical solution temperature, LCST. Below LCST, the un-crosslinked polymer chains are soluble in water whereas above LCST the polymer chains form submicro- and micro-aggregates, which separate from solution. Thermo-responsive hydrogels composed of cross-linked polymer chains undergo fast [38,39], reversible structural changes from a swollen to a collapsed state by expulsing water. However, also another kind of thermo-responsive hydrogels exist which is opposite to that LCST-hydrogels, *i.e.* the hydrogels with an upper-critical solution temperature, UCST. These hydrogels shrink at lower temperature and swell at higher temperature.

Obviously, due to short history of this family and the fact that these materials are not commercially available, a great deal of fundamental knowledge regarding their properties is still lacking. Polymer interactions are very complex and no complete molecular-level understanding exists to date. Mostly, the absence of water molecule interaction is typical for theoretical interpretation of this specifically behavior.

## 2. Classification of TRHRS

According to behavior of thermo-responsive hydrated reticular systems (TRHRS) during dilution we can divide them onto water dilute-able and non dilute-able, the crosslinked 3D networks (see **Figure 1**) or crosslinked 2D networks – films. Additionally, it is possible to divide the dilute-able TRHRS onto fully dilute-able polymer solutions at T< LCST (or T > UCST) and coacervated [51-53] submicro- or micro-TRHRS or flocculated macro-TRHRS.

The dilute-able TRHRS coacervate or flocculate in water environment due to weak bonds among of polymer chains, micro-particles and hydrogel particles or fibers and micro-fibers, respectively. It is typical of the submicro-, micro- and macro-networks that are disrupting during dilution process, *i.e.* the quasi-hydrogels are coacervating and the fiber networks are flocculating, respectively. As a temperature changes, the sol-gel reversible hydrogels transition occurs due to non-chemical crosslinks being formed among grafted and branched elements of copolymers.

The crosslinked structures created by strong particularly chemical bonds among polymer chains like micro- and macro-sponges have been then swelled or shrunk in response to the temperature change over the LCST.

### 2.1. LCST Hydrogels

PNIPAAm, has been the most used macromolecule in thermo-responsive hydrogels. The changing in properties with temperature in PNIPAAm is based on a phenomenon that is thermodynamically similar to that causing temperature-induced protein folding [17]. Above the LCTS a reversible structural transition occurs from expanded coil (soluble chains) to compact globule (insoluble state), at around 32°C in pure water [3,13,14,40-42]. Below the LCST, the hydrogel is swollen and absorbs a significant amount of water, while above LCST, the hydrogel dramatically releases free water and begins to shrink. Mostly opinion is prevailing that the solubility is affected because the amphiphilic PNIPAAm chains hide the hydrophilic amide groups and expose the hydrophobic isopropyl groups in the compact globule structure. The most common LCST hydrogels are the ones obtained by chemical crosslinking of hydrophilic macromolecules. Such linkages prevent the dissolution of the material but water can penetrate within the micro-reticular structure, causing the swelling of the structure without disrupting the mechanical and geometrical integrity of the structure.

During a volume transition the hydrogel anti-bonding system formed between water molecules and the polymeric chains is disturbed, being this thermodynamically favourable increasing in entropy the main driving force for the occurrence of the transition. For the case of crosslinking systems this transition can be seen through an abrupt shrinkage of the hydrogel above the LCST associated with the change in the swelling capability of the hydrogel. In addition, DSC analysis indicates that this process is accompanied especially for cross-linked hydrogel with heat consumption, *i.e.* an endothermic process [1,2,39]. The LCST, the characteristic tempera-

 

ture for solution–to-gel transition, is also defined as the temperature at which the elastic modulus crosses over the viscous modulus []. From this reason, the rheological behaviour of hydrogels as the function of temperature is oft measured [1,11].

N-isopropylacrylamide may be also copolymerized in order to include linear, end functionalized and crosslinked binary and ternary copolymers [4,5], graft and block copolymers [1,17,18]. However, PNIPAAm is non-biodegradable and it is not readily cleared from the body at physiological temperature. That is why bioadsorbable thermo-responsive polymer systems have been achieved by incorporation of biodegradable segments such as hyaluronic acid [46], gelatine [12], peptides [47] and collagen [1,32] into PNIPAAm-based polymers. N,N´-methylenebisacrylamide (MBA) is oft utilized as crosslinker [39,43]. Such macromolecular design widens the applicability of such systems in a variety of biomedical applications inclusive biomineralization on biodegradable substrates [44]. Such modifications are particularly important to tailor the LCST of PNIPAAm-based systems. For example, random copolymers containing hydrophilic units (e.g. acrylic acid) or $Ba^{2+}$ ions exhibit higher values of the LCST [4,5], and an opposite trend is observed in copolymers containing hydrophobic groups (e.g. n-butyl methacrylate) [34] or $Cs^{+}$ ions [5]. It was also observed (laminin-1-functionalized methylcellulose by periodate oxidation) [10] that the LCST is dependent on polymer concentration, as decreasing polymer concentration increased the LCST. This observation is in contradiction with UCST increase vs. temperature – see **Figure 1**.

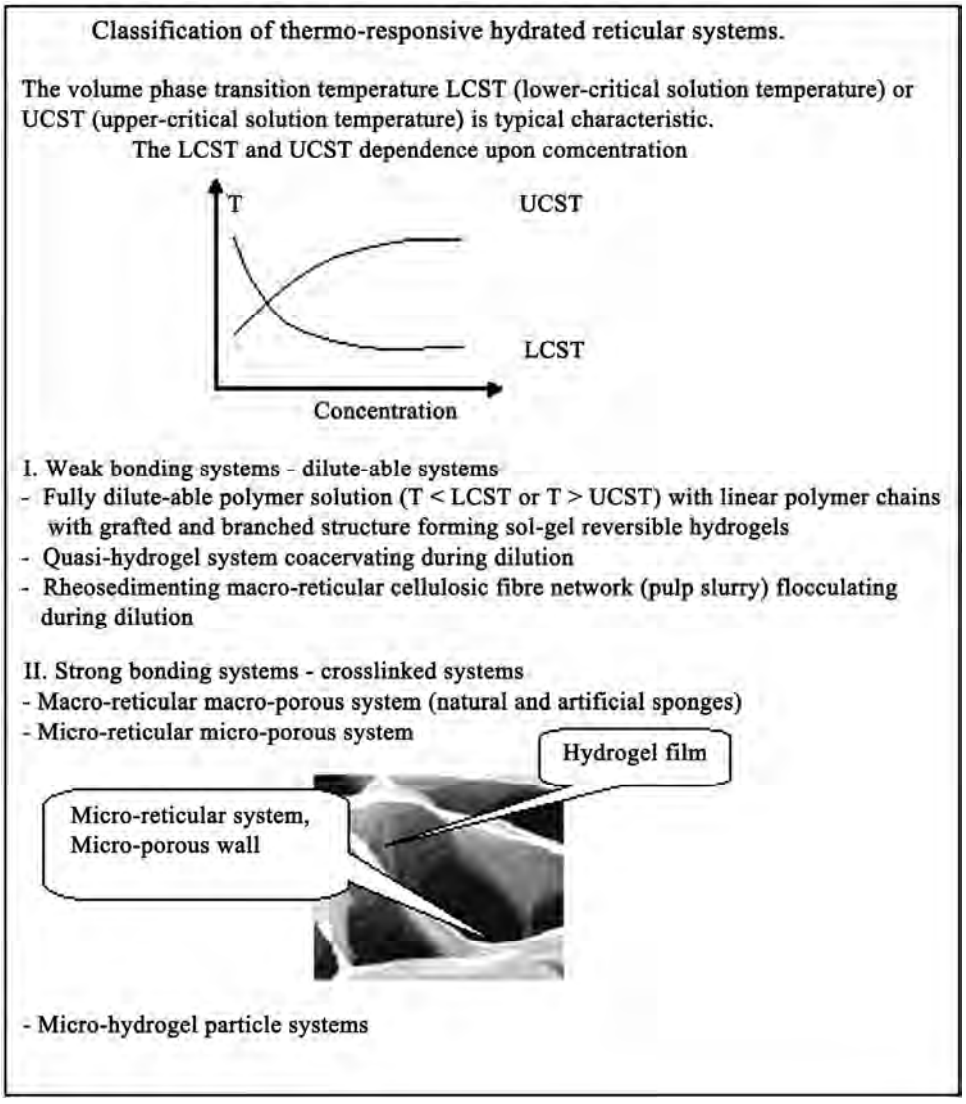


**Figure 1. Schematic illustration of classification of thermo-responsive hydrated reticular systems.**

 

Instead of PNIPAAm-based polymers also other polymer bases exist, e.g. poly(N,N-diethylacrylamide) (pDEAAm) [45], poly(N-cyclopropylacrylamide) [15], a "dual" nanocomposite based on poly(vinyl acetate) (PVAc) and cellulose whiskers [12], poly-D-lysine-functionalised chitosan [11], the hydrogel photoresist, which was formulated by mixing poly(HEMA-co-MMA) synthesized by radical copolymerization of 2-hydroxyethyl methacrylate (HEMA) and methyl methacrylate (MMA) with a crosslinker, tetramethoxymethyl glycoluril [16]. Most promising family of protein polymers is elastine-like polypeptides (ELP) [1,32]. ELPs have shown an outstanding biocompatibility. In addition, the ELPs have an acute "smart" nature.

Below the transition temperature, the uncrosslinked polymer chains are soluble in water but above LCST, the polymer starts a complex self-assembling process that leads to an aggregation of polymer chains, initially forming nano- and micro-particles, which segregates from the solution [32]. The copolymers with branched structure,(e.g.poly-(NIPAAm-co-AAc-co-HEMAPTMC, *i.e.* prepared by copolymerization of NIPAAm, acrylic acid (AAc) and biodegradable monomer hydroxyethyl methacrylate-poly(trimethylenecarbonate)(HEMAPTMC)) are accompanied above LCST with sol-gel transition occurred immediately when the clear solution is immersed into the water bath. After incubation, a highly flexible gum-like material is then formed and de-swelling is further observed during continued warming in water bath [4].

For the case of crosslinking three-dimensional systems this transition can be seen through an abrupt shrinkage of the hydrogel above the LCST associated with the change in the swelling capability of the hydro-reticular material. The volume phase transition process upon heating connected with water molecules expulsion from hydro-reticular spaces - known as hydrogel syneresis [50] - is reversible with thermal and stimuli responsivity [13,39, 48-49] but with different response dynamic and volume changes. It was proved that the reversible transition during the heat cycle is due to the elasticity of crosslinked hydrogels [16]. Since the rapid response dynamic and large volume changes due to temperature variation is the essential function for intelligent hydrogels applications, the thermo-responsive hydrogels with improved response rate and large volume changes to an external temperature stimulus are preferred [31,39]. The improved response dynamic of the hydrogels are obtained through incorporating siloxane linkage [31], cold polymerization and the pore-forming agent, etc. [39].

Though a lot of information exists describing the behaviour of TRHRS some of the mechanisms involved in the volume transition critical solution temperature are still not well understood. The smart surface designs mostly based on stimuli-responsive materials forming self-assembled monolayers (SAMs) and surface-tethered polymers, known as polymer brushes, suggested that the polymer chains of PNIPAAm and its copolymers have two structures in aqueous solution [26]. Below its LCST, PNIPAAm polymer is in an extended, solvent-swelled structure, but when heated up above LCST, the polymer undergoes a phase transition to yield a collapsed morphology that excludes water [17,44]. For example, these widespread structural changes enable the multiresponsive surfaces reversible change on silicon substrate to be realised between superhydrophilicity and superhydrophobicity [13]. It is important that the silicon surface roughness becomes the main factor in intensifying this behaviour. In contrast to magnitude of the contact angel changes on flat film, a remarkably large change in this one was induced on rough substrate. Logically, for a rough surface with a high surface free energy, the film is more hydrophilic or more hydrophobic. Nevertheless, PNIPAAm surfaces cannot be described only in terms of surface wettability, because above the LCST the surfaces are only partially dehydrated [33].

Usually, this behaviour is based on confusing explanation that a hydrogen bond network between the amide groups and water molecules are formed at lower temperature, whereas at higher temperatures the stabilizing H-bonds break up and the hydrophobic interactions become predominant [26]. Thus the hydrophobic interactions among the hydrophobic groups become stronger which subsequently induce the freeing of the entrapped water molecules from the hydrogel network [13,26,39]. However, indication confirming an important role of water molecules in behaviour of TRHRS was observed. Temperature- and light-responsive polyacrylamide copolymers featuring salicylideneanilin as a photochromic group is reported which structure by irradiation and turning off the UV light is changed, but the respective LCSTs values remained higher than before irradiation. The LCST shift after irradiation can be explained by an intramolecular stabilization of the exited *keto* form in high polar media such as water because after evaporation of the samples solutions and redissolving in water, the values for the LCST were the same as before irradiation [15].

A similar mechanism of structural transition from expanded coil to squeezed proper thermodynamically advantageous structure is possible to expect at crosslinked TRHRS as the temperature is raised above the LCST, because macroporous hydrogels, *i.e.* hydrated macroreticular systems, are consisted from walls which are formed by micro- and submicro-porous sections of the hydrogel character as well as. These facts ensue from the

 

observations of non-expectable low wall density of macroporous thermo-sensitive hydrogels from recombinant elastin-like polymers (ELP) [1]. For example, according to myself recalculation of the results presented in liter. [1], the wall densities of ELP hydrogels in clear water were 0,4405 g/cm$^3$ at T = 4$^o$C and 0,6081 g/cm$^3$ at T = 37$^o$C but had been lowered dramatically with increasing salt/polymer ratio at T = 4$^o$C to 0,0677 – 0,0850 g/cm$^3$ although the densities at T = 37$^o$C were approximately unchanged (0,436 - 0,617 g/cm$^3$). By parallel action of all submicro- and micro-sections composing the walls of macro-reticular system, the hydrated macroporous system is then swelled or de-swelled in dependence on the temperature changes crossing a value of the LCST.

Summarizing up of the all above mentioned facts, we can conclude that at usually conditions, *i.e.* at room temperature and inert environment, the PNIPAAm polymer has preferred thermodynamically advantageous a coil conformation because the hydrophobic interactions among isopropyl pendant groups. However, due to peculiar water activity, the coil conformation is stretched at temperature below the LCST in contradiction with squeezed the original coil conformation above the LCST as the repulsive domain activity is weakened – see schematic illustration in **Figure 2**. The peculiar water activity is accompanied below the LCST by origination of repulsive water action among polymer chains, its segments, submicro- and micro-colloidal particles etc. arising from equally water molecules orientations at interacting interface micro-domains due to hetero- followed by homo-H-bonds among them, *i.e.* a hydration anti-bonding system. Obviously, a width of vicinal immobilised water within interacting polymer interfaces decreases with increase of polymer concentration because improving disruption action of the hydration repulsive forces being weakened dramatically with a temperature increase. As result, the LCST decreases with polymer concentration increase [10].

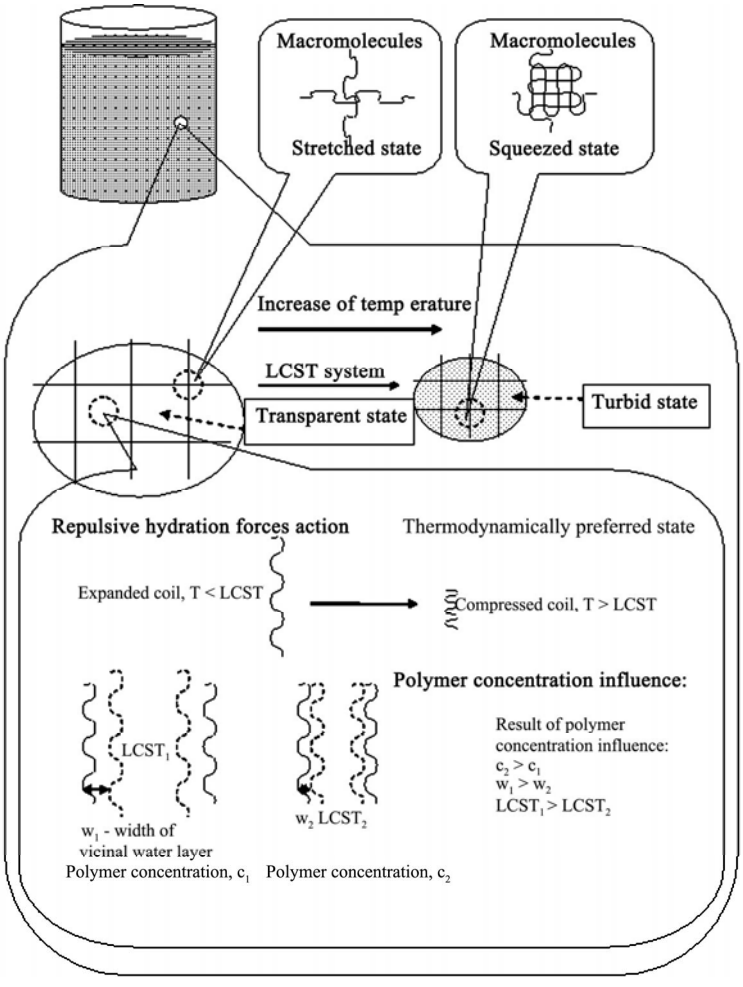


**Figure 2. Schematic illustration of temperature and concentration influence on behaviour of hydrated micro- and nano-reticular systems distinguished by LCST.**

 

## 2.2. UCST Hydrated Reticular Systems

Until very recently [17,43], little works has been reported on positively thermo-responsive microgel particles with UCST, *i.e.* hydrogels that shrink at lower temperature and swell at higher temperatures, although they should be preferred to negatively thermo-responsive microgels in certain applications. The UCST hydrogels are mainly composed of an interpenetrating polymer network (IPN) of polyacrylamide (PAAm) and poly(acrylic acid) (PAAc) or poly(acrylamide-co-butyl methacrylate) crosslinked with MBA [43]. The formation of helices (double or triple in polysaccharides such as agarose, amylase, cellulose derivatives and carrageenans or in gelatine, respectively) and corresponding aggregation upon cooling, forming physical junctions, are on the base of hydrogel formation [17]. Dilute-able but coacervating quasi-hydrogel with UCST are represented by urea-formaldehyde (UF) pre-condensates [51-53].

Thermo-responsive volume phase transition behaviour of these TRHRS is opposite to that of PNIPAAm-based polymers. Again, the description of this behaviour is based on confusing explanation [43] that the IPN hydrogels form intermolecular complexes via hydrogen bonding at temperatures lower than the UCST while dissociate at temperatures higher than the UCST. According to this explanation, driven by the hydrogen bonding, the PAAm/PAAc based IPN hydrogels shrink at lower temperatures and swell at higher temperatures revealing positively thermo-responsive volume transition behaviour. Aside from the facts that mostly parts of IPN are penetrated with water molecules, it is interesting to look in closer way at the areas in the LCST and UCST hydrated reticular systems.

Really, the mechanism of the reversible behaviour is similar to that of TRHRS with the LCST but in opposite manner - see schematic illustration in **Figure 3**. At usually conditions, *i.e.* at room temperature and inert environment, the UCST hydrated crosslinked and un-crosslinked polymers have preferred thermodynamically advantageous a long-chain structure which is squeezed in water environment to compressed coil conformation due to origination of weak hydration bonding system. The hydration bonding system [52-58] among polymer chains, its segments, submicro- and micro-colloidal particles etc.

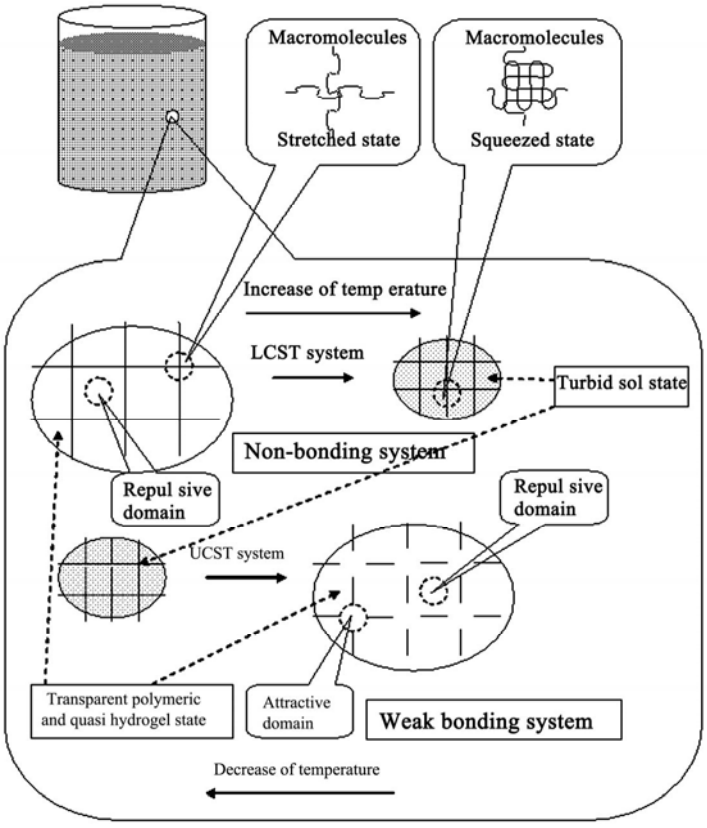


**Figure 3. Schematic comparison of both the TRHRS with LCST and UCST. The weak bonding system is represented in this case by coacervating of quasi hydrogel system with UCST.**

 

arise from opposite water molecules orientations at interacting interface micro-domains because hetero- H-bonds to proton-acceptor or proton-donor groups of polymer chains and homo-H-bonds among water molecules. As the temperature increases the hydration bonding system is weakened because the increase of water molecules kinetic energy. Above the UCST, the hydration bonding system is weaker than inner opposite stress of compressed polymer chains of TRHRS and the polymer chains have been expanded. As result, the crosslinked TRHRS are swelled and the polymer chains in non-crosslinked TRHRS are dissolved. Under the UCST, the hydration bonding system is stronger than inner opposite tension of compressed flexible polymer chains and the polymer long chains have been compressed. The process is resulted in de-swelling and coacervating of crosslinked hydrogel and dissolved polymers, respectively.

With increase of polymer concentration in contradiction with LCST systems a width of vicinal immobilised water also increases within interacting polymer interface micro-domains, because improving stabilization action of the hydration attractive forces although they are disturbed as well with a temperature increase. As result, the UCST increases with polymer concentration increase [51] – see **Figure 4**.

## 3. TRHRS with Weak Bonding System

As already said, the UCST hydrated polymers with preferred the long-chain flexible structure are squeezed in water environment to compressed coil conformation due to origination of weak intra- and inter-hydration bonding system. Obviously, both the intra-hydration bonds squeeze the long-chain un-crosslinked polymer structure to compressed coil conformation and the inter-hydration bonds squeeze the long-chain but crosslinked structures to de-swelled form in temperatures below UCST. However, other characteristic behaviour is observed if a hydrated reticular system is composed of relative rigid rod like particles as short polymer chains or fibres. The short polymer chains or fibres in hydrated submicro- or macro-reticular systems, respectively, are formed through inter-hydration bonds and the inter-hydration repulsive domains, *i.e.* mutually functioning hydration bonding and de-bonding sites. As typical, due to increased fluctuation at the bonding and de-bonding activities of interacting micro-sites during dilution the submicro-reticular systems are coacervating and the macro-reticular systems are flocculating.

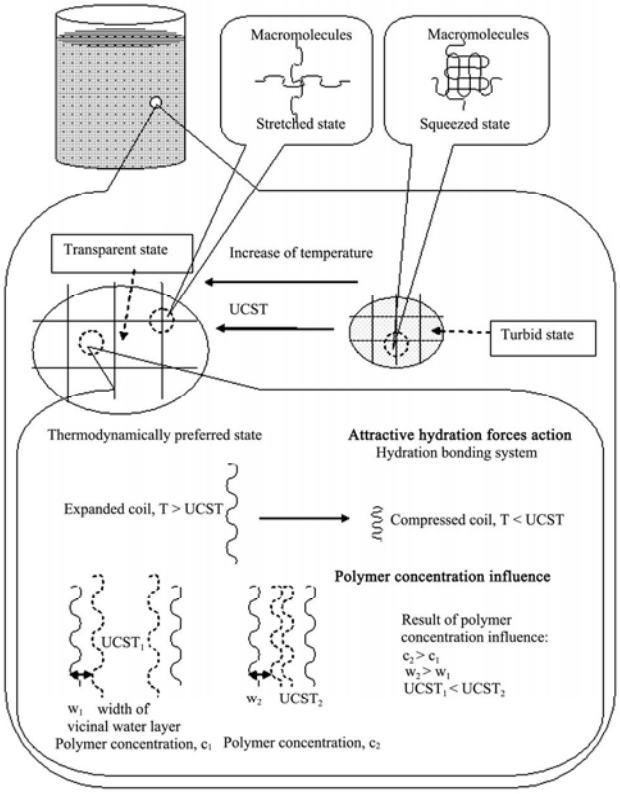


**Figure 4. Schematic illustration of temperature and concentration influence on behaviour of hydrated micro- and submicro-reticular systems distinguished by UCST.**

 

The submicro weak bonding hydro-reticular system accompanied by coacervation during a dilution is well demonstrated by use of UF pre-condensate [51-53]. The UF pre-condensates form in concentrated state optically homogeneous systems with water, but when gradually diluted the quasi-hydrogel system having reached so-called critical degree of dilution (CDD) gets turbid, *i.e.* the quasi-hydrogel – coacervate transition [51] is taken place. The behaviour of such systems can be simply explained by concept of hydrations forces. Individual oligomeric molecules or short relative rigid polymer chains are evenly distributed in water environment at concentrated state at room temperature, when the hydration forces are functioning to sufficient extent. Minimum internal energy can be reached if all water molecules are contained only in mutually hydration spheres of diffusing character around the hydrated molecules or short polymer chains. The whole system is isotropic with regard to the sizes of its structural units and more viscous owing to the attraction of hydration forces. The lower is CDD, the higher is viscosity of this system. In the water system, hydration forces that repulse alternate regularly with hydration forces that attract. On gradual diluting, hydrated structural units separate from each other, becoming more free and mobile owing to the fluctuation effect of the attractive and repulsive forces and as well a heat. They are less and less limited in their motion, so that they take a more preferable orientation in their collisions. Owing to non-isometric form of the structural units, some of these ones take a new better arranged state at suitable moment after breaking a 3D submicro-network, becoming oriented to each other in a certain order similar to the concentrated state. The whole system of structural units behaves during dilution like a stretching network which is gradually ruptured after reaching CDD. As a rule, the quasi-hydrogel – coacervate transition is accompanied logically by exothermic heat effect followed by increase of density, viscosity and surface tension of sedimented coacervate phase [51]. A lot of additional components influence the attractive forces connecting the individual weak links of network of UF pre-condensates and also the properties of the coacervates. This influence is either a positive one, *i.e.* an increase of the attraction, or negative one, *i.e.* a decrease of attractive hydration forces. As we can expect the UCST is increased due to increasing attractive hydration forces, *i.e.* with improving hydration bonding ability of the TRHRS.

The macro-reticular systems with weak bonding system are represented by papermaking pulp slurries composed of fibres of cellulosic or ligno-cellulosic character. It is typical for components with marked papermaking properties that forms fibre network which is only compressed during sedimentation, *i.e.* process behaviour called as rheosedimentation [59,60]. Basic condition of rheosedimentation is an ability of pulp fibre to form a network with special behaviour, *i.e.*, due to weak bonding system a fibre network is compressed by gravity [60,61]. The homogeneous pulp fibre network is formed at concentration higher than1 kg/m$^3$ of suspension. Following dilution of the suspension under the concentration of 1 g/l is then accompanied by flocculation and rheosedimentation. However, the rheosedimented fibre net- work is not in fully homogeny state because lack of shear forces (agitation) disturbing rheosedimenting floccules. The temperature influences of both the macro-reticular fibre system and the hydrogels structure of fibres with complicated morphology. Predominantly, the tempera- ture-responsive activity of hydrated microstructure of fibres is important from practical point of view. We have been observed during wet pulp beating that characteristic decreasing of pulp drainage ability with increasing input beating energy is abruptly increased if the temperature of beating pulp slurry is higher then 40$^o$C – see **Figure 5**. This fact indicates some LCST behaviour of hydrogels forming the beated fibres. As the temperature is raised above the LCST the fibre hydrogels deswell by contraries with the swelled state below the LCST, *i.e.* at temperature above the LCST of fibres the pulp slurry is better drained and vice versa.

## 3.1. SCHL Theory and Hydration Bonding Concept

The SCHL (structural changes in hydration layers) theory [62] has been designed to deal with the interaction

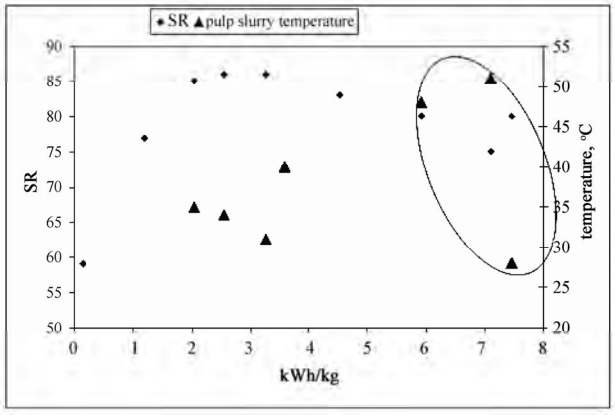


*Notice: SR – degree of pulp beating according to Schopper-Riegler (ČSN EN ISO* 5267-1) *- the drainage ability of pulp slurry decreases with increasing of SR*; *Effective beating energy consumption* (*kWh/kg of oven dried pulp fibre). Beating conditions: - Laboratory ring beater; - Non-bleached hemp pulp prepared by alkaline cooking method; - Pulp beated at* 3% *consistency during* 49 *minutes at approximately constant operating beater edge load.*

**Figure 5. Temperature of pulp slurry influence upon drainage ability of beated hemp pulp.**

 

mechanism in hydrated hydrophilic systems. The hydration bonding concept, *i.e.* a formation of hydration weak bonds or anti-bonds, follows up of the SCHL theory. The idea of the origins and effect of hydration forces is based on typical dipole character of water molecules and on their two possible basic orientations in hydration spheres (called as immobilised or vicinal water) around the hydrophilic sub-micro domains [52-57] depending upon their nature. The possible orientations of water molecules with regard to the hydrophilic domains forming hydrophilic phase interface vary essentially between the following extreme positions (see **Figure 6**):

◄ orientation with the H-atoms of water molecules to the submicro domain with proton acceptor activities,

► orientation with the O-atoms of water molecules to the submicro domain with proton donor activities.

Owing to this orientations of water molecules, an intermolecular field of force produced by hydrogen bonds formed among them will then spread by means of the other molecules through the hydration sphere under the influence of this orientation of water molecules, becoming more and more diffused until it equals the zero value in bulk of water. This effect serves as origin of the force action between interacting sub-micro domains of phase interfaces, *i.e.* the hydration forces. If the orientation of water molecules is equal to each of the interacting domains, the two sub-micro domains will affect each other with repulsive hydration forces, *i.e.* the hydration debonding system prevails. In the opposite case, when the orientation of water molecules to each of the sub-micro domains is different, the interacting surface domains will affect each other with attractive forces, *i.e.* creation the hydration bonding system. According to this theory, the groups forming hydrogen bonds with water followed by hydration bond formation can be divided into three types:

i) H-donor groups and molecules: such as primary alcoholic OH-groups, secondary amino groups and primary amino groups.

ii) Amphoteric groups and molecules: such as $H_2O$, secondary alcoholic OH-groups in polysaccharides, and partially primary amino groups, amido groups etc.

iii) H-acceptor groups: such as hemiacetal oxygen in saccharides, carbonyl groups, and tertiary amino groups.

Interestingly, under the same conditions, the repulsive forces are effective over a greater distance and the effect of attractive forces prevails on short distances (approximately smaller than 4 nm) but at the shortest distances the attractive forces are stronger than repulsive forces.

This difference appears in the interactions of heterogeneous mosaic surfaces [62] containing sub-micro domains in which repulsive and attractive hydration forces act simultaneously as a kind of equilibrium established in which the two interacting surfaces reach a definite optimum distance from each other – see **Figure 7**. In the interaction, mutual diffusion of their hydration spheres takes place, connected with a change of their structure. The effects of hydration forces decrease with a temperature increase and practically disappear at boiling point of water. The structural changes take place on the molecular level, being accompanied by appropriate heat effects [51-53,62]. Theoretically [62] it has been shown and confirmed experimentally [51] that the action of attractive forces is an exothermic process connected with decreasing of entropy while the action of repulsive hydration forces (*i.e.* under influence of external forces) has an endothermic character connected with increasing of entropy.

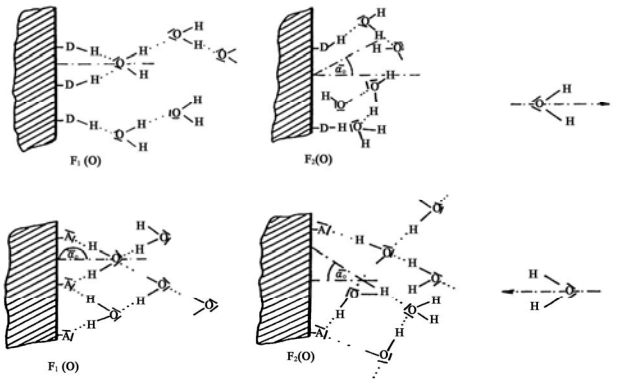

**Figure 6. Conception [62] of the orientation of water molecules around various types of sub-micro domains at phase interface. $\overline{\alpha_o}$ - average axis angle of water molecules related to the phase interface normal at its close vicinity; F(0) – potential energy of water molecule in d (distance) = 0; A – proton acceptor group, D – proton donor group.**

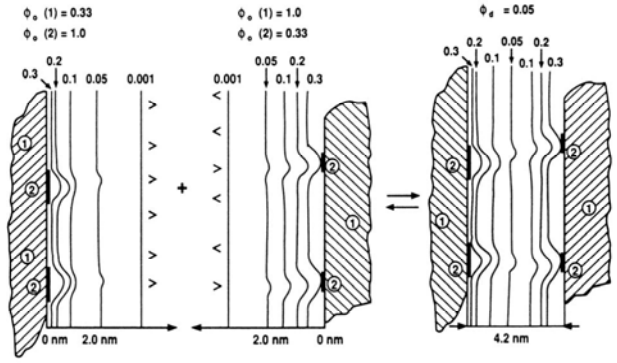

**Figure 7. The course and dependence [51] of isopotentials on the distance between interacting domains of heterogeneous surfaces – the creation of hydration bond system. >; < - depiction of the prevailing orientation of water molecules in the hydration layers; d – distance from the phase boundary; $\Phi_o$ (relative potential of water molecule in d = 0) = $F_1(0) / F_2(0)$, $F_2(0) > F_1(0)$.**

 

### 3.2. Biomimetic Systems Especially Artificial Muscles

Recently, discovery of cellulose as a smart material was described that can be used for biomimetic sensor/actuator devices and micro-electromechanical systems [25]. This smart cellulose is termed electroactive paper (EAPap) because it can produce a large bending displacement with low actuation voltage and low power consumption. The authors in [25] are proposed that electroactive paper is advantageous for many applications such as micro-insect robots, micro-flying objects, micro-electromechanical systems, biosensors, and flexible electrical displays. By use of this phenomenon it is possible also to explain and simulate muscles movement.

EAPap is made with a cellulose film (cellophane) on which gold electrodes are deposited on both sides. An EAPap actuator was supported vertically in environment chamber that can be controlled the humidity and temperature. By excitation of voltage application to the actuator a bending deformation is evoked. The authors [25] believe that the actuation is due to a combination of two mechanisms: ion migration (diffusion of sodium ions to anode?) and dipolar orientation. Again, in spite of their confusing and irrational explanation of the EAPap movement the received results have high inspiring potential and challenge. The tip displacement of the EAPap actuator is dependent on applied electric field, its frequency, EAPap sample thickness and temperature but predominantly on humidity. The humidity affects the displacement, where a high relative humidity leads to a large displacement. It is no problem to explain this behaviour by use of SCHL theory.

An orientation of water molecules in immobilized layers around cellulose macromolecules in stratified structure of EAPap actuator is determined by presence of proton donor groups or proton acceptor groups at their interacted surfaces. The overall film structure and its shape are formed among structural cellulosic units due to both the hydrogen-bonding bridging in dry state and the hydration-bonding bridging in wet state. Extent and intensity of this bonding system is determined by size, concentration and distribution of nano-domains either with the attractive or the repulsive force action, *i.e.* among interacting opposite nano-surfaces with reversal or identical basic orientation of water molecules, respectively. The basic orientation of water molecule is given by presence of surface proton donor groups or proton acceptor groups of cellulose. Whilst hemiacetal and glycosidic oxygen in cellulose is typical proton-acceptor groups the hydroxyl groups can behave as proton-donor and proton-acceptor groups. Nevertheless, one is supposed that mostly behaviour of hydroxyl groups in cellulosic materials has more a proton-donor character.

In consequence of this preposition, the domains of prevailing hydration-bonding bridging are regularly distributed within cellulosic material with flat formation. By any disturbing this distribution, the paper strip curling is evoked because the inner tension equilibrium is disturbed. As schematically presented in **Figure 8**, by application of oriented electric field on cellulosic material in wet state the water molecules in bonding nano-domains contained nearest the electrodes are reoriented. However, reorientation at cathode is different of the reorientation at anode – at anode are reoriented only all the water molecules having been oriented to this pole with hydrogen atoms and at cathode only these ones having been oriented to this pole with oxygen atoms at basic origin state. Moreover, the distribution of attractive forces formed around both the **A** and **D** and the **D** and **A** nano-centres is not the same – it is supposed a prevailing **A** - **D** structure orientation in bonding domains. At this situation, an application of dc electric field is evoked a weaker bond system in layers laying near anode and vice-versa a stronger bond system in layers near cathode. Due to this effect the paper strip gets to bend to anode. Logically, the effect is strongly dependent upon relative humidity, the reorientation of water molecules is independent on diffusion process and it is relatively quickly.

Obviously, by similar effect, but in microscale, a muscles movement is possible to explain. The main preposition – the non-symmetrical distribution of attractive forces formed around both the **A** and **D** and the **D** and **A** nano-centres.

The enhancement of the protein folding owing to the physical properties and microstructure of the host organic-inorganic nanoporous silica matrix induced by the nature of the functional groups and the siloxane network is probably a further similar effect of the hydration forces system activity [64].

## 4. Conclusions

During last decade a lot of information was collected describing the behaviour of hydrated reticular systems (e.g. hydrogels, quasi-hydrogels, pulp fibre network) with a temperature response, *i.e.* the hydrogels with LCST and the hydrogels with UCST. Particularly, the TRHRS with LCST were studied because their biomedical importance. It seems that the behaviour is given by specific thermodynamically base conformation state of a main polymer forming the TRHRS at room temperature, *i.e.*:

- squeezed state of polymer coil conformation above LCST being stretched by an influence of inner repulsive intermediary forces under LCST and,

- more stretched state of polymer coil conformation above UCST being contrary compressed by an influence

 

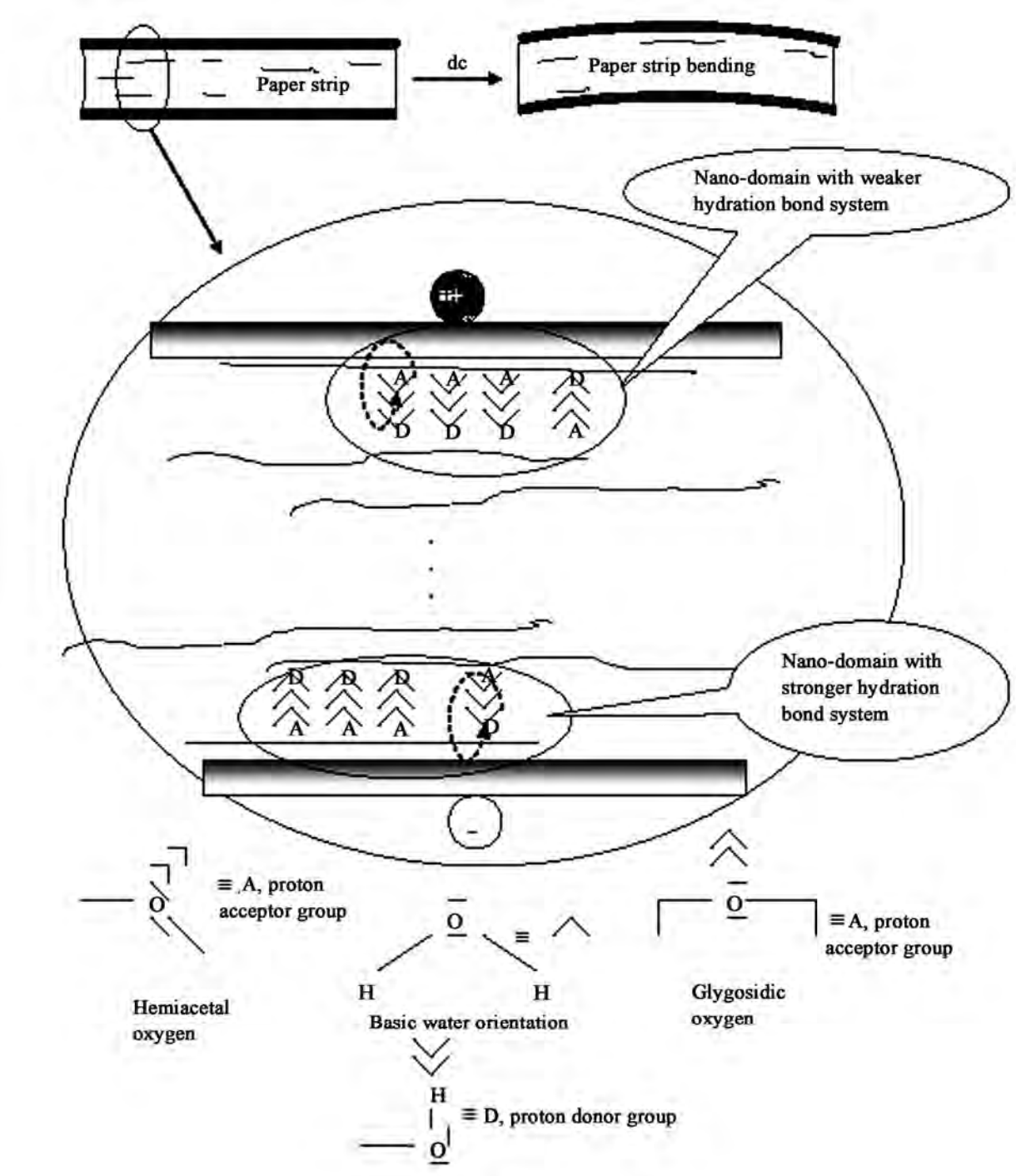


**Figure 8. Schematically representation of water molecules reorientation in vicinity of electric input field inside nano-localities of cellulosic materials.**

of the intermediary attractive forces under UCST.

It was shown that both sorts of the intermediary forces are the repulsive and attractive intramolecular hydration forces theoretically explained by SCHL theory.

However, more challenging attention is evoking by swelling or de-swelling activity of elastic crosslinked polymers forming hydrogels with rapid thermoresponsive dynamics, because their similarity to biomimetic dynamic of muscle tissues of animals. At present, the aim to better understanding to movement of biological

 

systems prompting the TRHRS to offer the crosslinked hydrogels serve as artificial objects of experimental studies. Acceptable moveable hydrogel system, e.g. with stratified structure composed of useful crosslinked both the LCST and the UCST hydrogels, is possible to create and to evoke its movement by changing temperature around LCST and UCST but only in a connection with mutually water transport. The recently described biomimetic systems not behave as a really artificial muscle but only as the hydrogel with rapid syneresis. Obviously, a muscle movement represented by mutual movement of different muscle tissue like myosin and actins take place on an- other principle than that one connected with water expulsion and retention. Moreover, the dynamic of real muscle response is incomparable higher because it is not connected with water transport.

As a matter of fact, actually how is it possible to realise this basic bio-property?

As theoretically follows of the hydration bonding - debonding concept being applied upon micro- and submitcro-reticular systems, the stratified muscle tissue is squeezed by prevailing of hydrated bond formation and stretched by prevailing of hydrated anti-bonds. The all of changes are evoked only by merely overturning the orientation of interacting water molecules in hydration layers around interacting hydrophilic interface micro-domains. This overturning is relative very quickly and it is connected with heat evolving - the formation of attractive hydration forces is prevailing - or heat consumption - the formation of repulsive hydration forces is prevailing. A real mechanism evoking this water molecule orientation changing by inner or outer stimuli in muscle tissue is still not known. Probably, the evocation of amphoteric hydroxyl or amino interface groups is responsible for this alternating orientation.

## REFERENCES


[1] L. Martín, M. Alonso, A. Girotti, F. J. Arias and J. C. Rodríguez-Cabello, "Synthesis and characterization of macroporous thermosensitive hydrogels from recombinan elastin-like polymers," *Biomacromolecules*, Vol. 10, No. 11, 2009, pp. 3015-3022.

[2] A. Girotti, J. C. Reguera, F. J. Rodríguez-Cabello, M. Arias, A. Alonso and J. MaTestera, "Design and bioproduction of a recombinanat multi(bio)functional elastin-like protein polymer containing cell adhesion sequences for tissue engineering purposes," *Journal of Matierals Science, Materials in Medicine*, Vol. 15, 2004, pp. 479-484.

[3] J. E. Wong, A. K. Gaharvar, D. Müller-Schulte, D. Bahadur and W. Richtering, "Dual-stimuli responsive PNiPAM microgel achieved via layer-by layer assembly: magnetic and thermoresponsive," *Journal of Colloid and Interface Science*, Vol. 324, 2008, pp. 47-54.

[4] K. L. Fujimoto, M. Zuwei, D. M. Nelson, R. Hashizume, J. Guan, K. Tobita and W. R.Wagner, "Synthesis, characterization and therapeutic efficacy of a biodegradable, thermoresponsive hydrogel designed for application in chronic infarcted myocardum," *Biomaterials*, Vol. 30, 2009, pp. 4357-4368.

[5] J. Xiao-Jie, C. Liang-Yin, L. Li, M. Peng and M. L. Young, "A Novel Thermoresponsive hydrogel with ion-recognition property through supramolecular host-guest complexation," *Journal of Physical Chemistry B*, Vol. 112, 2008, pp. 1112-1118.

[6] J. J. Kang Derwent and W. F. Mieler, "Thermoresponsive hydrogels as a new ocular drug delivery platform to the posterior segment of the eye," *Transactions of the American Ophthalmological Society*, Vol. 106, 2008, pp. 206-214.

[7] Y. H. Bae, R. Okano, S. Hsu, W. Kim, "Thermo-sensitive polymers as on-off switches for drug release," *Makromol. Chem. Rapid Commun.*, No. 8, 1987, pp. 481-485.

[8] D. Ghate and H. F. Edelhause, "Ocular Drug Delivery," *Expert Opinion on Drug Delivery*, No. 3, 2006, pp. 275-287.

[9] T. Yasukawa, Y. Ogura, H. Kimura, E. Sakurai and Y. Tabata, "Drug delivery from ocular implants," *Expert Opinion on Drug Delivery*, No. 3, 2006, pp. 261-273.

[10] S. E. Stabenfeldt, A. J. García and M. C. LaPlaca, "Thermoreversible laminin-functionalized hydrogel for tissue engineering," *Journal of Biomedical Materials Research Part A*, 2006, pp. 718-725.

[11] K. E. Crompton, J. D. Goud, R. V. Bellamkonda, T. R. Gengenbachm, D. I. Finkelstein, M. K. Horne and J. S. Forsytie, "Polylysine-functionalised thermoresponsive chitosan hydrogel for neural tissue engineering," *Biomaterials*, Vol. 28, 2007, pp. 441-449.

[12] K. Shanmuganathan, J. R. Capadona, S. J. Rowan and Chr. Weder, "Stimuli-responsive mechanically adaptive polymer nanocomposites," *Applied Materials & Interfaces*, Vol. 2, No. 1, 2010, pp. 165-174.

[13] F. Xia, H. Ge, Y. Hou, T. L. Sun, L. Chen, G. Z. Zhang and L. Jiang, "Multiresponsive surfaces change between superhydrophilicity and superhydrophobicity," *Advanced Material*, Vol.19, 2007, pp. 2520-2524.

[14] L. Qiaofang, L. Pengxiao, G. Ying, Zh. Yongjun, "Thermally induced phase transition of glucose-sensitive core-shell microgels," *Applied Materials & Interfaces*, March 2010.

[15] F. D. Jochum and P. Theato, "Temperature and light-responsive polyacrylamides prepared by a double polymer analogous reaction of activated ester polymers," *Macromolecules*, Vol. 42, 2009, pp. 5941-5945.

[16] J. H. Kang, J. H. Moon S. K. Lee, S. G. Park, S. G. Jang, S. Yang and S. M. Yang, "Thermoresponsive hydrogel photonic crystals by three-dimensional holographic lithography," *Advanced Material*, Vol. 20, 2008, pp. 3061-3065.

[17] J. F. Mano, "Stimuli-responsive polymeric systems for biomedical applications," *Advanced Engineering Materi-*


 

*als*, Vol. 10, No. 6, 2008, pp. 515-527.

[18] M. Yoshida, R. Langer, A. Lendlein and J. Lahan, "From advanced biomedical coatings to multi-functionalized biomaterials," *J. Macrom. Sci., Part C: Polymer reviews*, Vol. 46, 2006, pp. 347-3756.

[19] G. Santaneel, N. Arup, C. Yang, T. Cai, Somesree GhoshMitra, D. Diercks and H. Zhibing, "Thermoresponsive Hydrogel Microvalve Based on Magnetic Nanoheaters for Microfluidics," In: J. Cheng, A. Khademhosseini, H.-Q. Mao, M.Stevens and C. Wang, Eds., *Responsive Biomaterials for Biomedical Applications, Mater. Res. Soc. Symp. Proc*., Warrendale, PA, 2008, Vol. 1095E.

[20] D. J. Beebe, J. S. Moore, J. M. Bauer, Q. Yu, R. H. Liu, C. Devadoss and B.-H. Jo, "Functional hydrogel structures for autonomous flow control inside microfluidic channels," *Nature*, Vol. 404, 2000, pp. 588-590.

[21] N. Idota, A. Kikuchi, J. Kobayashi, K. Sakai and T. Okano, "Microfluidic valves comprising nanolayered thermoresponsive polymer-grafted capillaries," *Advanced Material*, Vol. 17, 2005, pp. 2723-2727.

[22] H. Yang, Y.-H. Han, X.-W. Zhao, K. Nagai and Z.-Z Gu, "Thermal responsive microlens arrays, "*Appl. Phys. Lett*., Vol. 89, 2006, pp. 111-121.

[23] D. Chandra, J. A. Taylor and S. Yang, "Replica molding of high-aspect-ratio (sub) micron hydrogel pillar arrays and their stability in air and solvents," *Softmatter*, Vol. 4, 2008, pp. 979-984.

[24] M. E. Harmon, M. Tang and C. W. Frank, "A microfluidic actuator based on thermoresponsive hydrogels," *Polymer*, Vol. 44, 2003, pp. 4547-4556.

[25] J. Kim, S. Yun and Z. Ounaies, "Discovery of cellulose as a smart material," *Macromolecules*, Vol. 39, 2006, pp. 4202-4206.

[26] P. M. Mendes, "Stimuli-responsive surfaces for bioaplications," *Chem. Soc. Rev.*, Vol. 37, 2008, pp. 2512-2529.

[27] H. Kanazawa, K. Yamamoto, Y. Matsushima, N. Takai, A. Kikuchi and Y. Sakurai, "Temperature-responsive chromatography using poly (N- isopropylacrylamide)-modified silica," *Anal. Chem.*, Vol. 68, No. 1, 1996, pp. 100-105.

[29] H. Kanazawa, Y. Matsushima, T. Okano, "Temperature-responsive chromatography," *Adv. Chromatogr.*, Vol. 41, 2001, pp. 311-336.

[30] A. Kikuchi and T. Okano, "Intelligent thermoresponsive polymeric stationary phases for aqueous chromatography of biological compounds," *Prog. Polym. Sci.*, Vol. 27, 2002, pp. 1165-1193.

[31] H. Kanazawa, T. Sunamoto, Y. Matsushima, A. Kikuchi and T. Okano, "Temperature-responsive chromatographic separation of amino acid phenylthiohydantions using aqueous media as the mobile phase," *Anal. Chem.*, Vol. 72, 2000, pp. 5961-5966.

[32] H. Kanazawa, K. Yamamoto, Y. Y. Kashiwase, Y. Matsushima, N. Takai, A. Kikuchi, Y. Sakurai and T. Okano, "Analysis of peptides and proteins by temperature-responsive chromatographic system using N-isopropylacrylaide polymer-modified columns," *J. Pharm. Biomed. Anal*., Vol. 15, 1997, pp. 1545-1550.

[33] M. Gewehr, K. Nakamura, N. Ise and H. Kitano, "Gel permeation chromatography using porous glass beads modified with temperature-responsive polymers," *Makromolekulare Chemie*, Vol. 193, 1992, pp. 249-256.

[34] K. Hosoya, E. Sawada, K. Kimata, T. Araki, N. Tanaka and J. M. J. Frechet, "In situ surface selective modi- fication of uniform size macroporous polymer particles with temperature-responsive poly-n-isopropylacrylamide," *Macromolecules*, Vol. 27, 1994, pp. 3973-3976.

[35] H. Kanazawa, Y. Kashiwase, K. Yamamoto, Y. Matsushima, A. Kikuchi, Y. Sakurai and T. Okano, "Temperature-responsive liquid chromatography. 2. Effects of hydrophobic groups in N-isopropylacrylamide copolymer-modified silica," *Anal. Chem.*, Vol. 69, 1997, pp. 823-830.

[36] H. Lakhiari, T. Okano, N. Nurdin, C. Luthi, P. Descouts, D. Muller and J. Jozefonvicz, "Temperature-responsive size-exclusion chromatography using poly(N-isopropylacrylamide) grafted silica," *Biochim. Biophys. Acta*, Vol. 1379, 1998, pp. 303-313.

[37] H. Kanazawa, T. Sunamoto, E. Ayano, Y. Matsushima, A. Kikuchi and T. Okano, "Temperature-responsive chromatography using poly(N-isopropylacrylamide) hydrogel-modified silica," *Anal. Sci.*, Vol. 18, 2002, pp. 45-48.

[38] E. Ayano, Y. Okada, C. Sakamoto, H. Kanazawa, T. Okano, M. Ando and T. Nishimura, "Analysis of herbicides in water usingtemperature-responsive chromatography and an aqueous mobile phase," *J. Chromatogr. A*, Vol. 1069, 2005, pp. 281-285.

[39] M. Lutecki, B. Strachotova, M. Uchman, J. Brus, J. Plestil, M. Slouf, A. Strachota and L. Matejka, "Thermosensitive PNIPA-Based Organic-Inorganic Hydrogels," *Polym. J.*, Vol. 38, No. 6, 2006, pp. 527-541.

[40] X.-Z. Zhang, F.-J. Wang, C. C. Chu, "Thermoresponsive Hydrogel with Rapid Response dynamics," *J. Mat. Sci., Materials in Medicine*, Vol. 14, 2003, pp. 451-455.

[41] H. Hou, W. Kim, M. Grunlan and A. Han, "A thermoresponsive hydrogel poly (N-isopropylacrylamide) micropatterning method using microfliudic techniques," *J. Micromech. Microeng*, Vol. 19, 2009, pp. 1-6, 2009.

[42] R. M. P. da Silva, J. F. Mano and R. L. Reis, "Smart thermoresponsive coatings and surfaces for tissue engineering: switching cell-material boundaries," *Trends in Biotechnology*, Vol. 25, No. 12, 2006, pp. 577-583.

[43] H. Hatakeyma, A. Kichuchi, M. Yamato and T. Okano, "Bio-functionalized thermoresponsive interfaces facilitating cell adhesion and proliferation," *Biomaterials*, Vol. 27, 2006, pp. 5069-5078.

[44] X. Xin-Cai, Ch. Liang-Yin, Ch. Sen-Mei, Z. Jia-Hua, "Monodispersed thermoresponsive hydrogel microspheres with a volume phase transition driven by hydrogen bonding," *Polymer*, Vol. 46, 2005, pp. 3199-3209.

[45] J. Shi, N. M. Alves and J. F. Mano, "Thermally responsive biomineralization on biodegradable substrates," *Adv.*

 

*Funct. Mater.*, Vol. 17, 2007, pp. 3312-3318, 2007.

[46] Z. Ding, R. B. Fong, C. J. Long, P. S. Stayton and A. S. Hoffman, "Size-dependent control of the binding of biotinylated proteins to streptavidin using a polymer shield," *Nature*, Vol. 411, 2001, pp. 59-62.

[47] S. Ohya, Y. Nakayama and T. Matsuda, "Thermoresponsive artificial extracellular matrix for tissue engineering: hyaluronic acid bioconjugated with poly-(N-isopropylacrylamide)grafts," *Biomacromolecules*, Vol. 2, 2001, pp. 856-63.

[48] S. Ohya and T. Matsuda, "Poly (N-isopropylacrylamide) (PNIPAM)-grafted gelatin as thermoresponsive three-dimensional artificial extracellular matrix: molecular and formulation parameters vs. cell proliferation potential," In: Polym. Ed., *J. Biomater. Sci.* Vol. 16, 2005, pp. 809-827.

[49] J. A. Jaber and J. B. Schlenoff, "Polyelectrolyte multilayers with reversible thermal responsivity," *Macromolecules*, Vol. 38, 2005, pp. 1300-1326.

[50] S. A. Sukhishvili, "Responsive polymer films and capsules via layer-by-layer assembly," *Current Opinion in Colloid & Interface Science*, Vol. 10, 2005, pp. 37-44.

[51] K. Edelmann, "Lehrbuch der Kolloidchemie," Band I. VEB Deutscher Verlag der Wissenschaften, Berlin, 1962, pp. 353-358.

[52] M. Milichovský, "Behaviour of hydrophilic components in papermaking suspension. Part II. Experimental hydrated hydrophilic modeling system – Its properties and behaviour," *Scientific Papers, University of Pardubice*, Vol. 56, 1992, pp. 155-182.

[53] M. Milichovský, "A new concept of chemistry refining processes," *TAPPI J.*, Vol. 73, No. 10, 1990, pp. 221-232.

[54] M. Milichovský, "The role of hydration in papermaking suspension," *Cellulose Chem. Technol*., Vol. 26, No. 5, 1992, pp. 607-618.

[55] M. Milichovský, "O mechanizme vzaimodejstvij v bumagoobrazujustschich gidrofilnych sistemach," *Chimija Drevesiny*, No. 1, 1990, pp. 69-78.

[56] M. Milichovský, "Chemische Aspekte der Mahlung von Zellstoff," *Zellstoff und Papier*, Vol. 38, No. 1, 1989, pp. 17-23.

[57] M. Milichovský, "Nowe poglady na wlasciwosci papierniczy zawiesin wodnych," *Przeglad Papierniczy*, Vol. 46, No. 12, 1990, pp. 418-422.

[58] M. Milichovský, "Klíčová role vody při výrobě a užití papíru a papírenských výrobků (Water as Key Substance in Production and Utilisation of Paper Products)," *Papír a celulóza*, Vol. 55, No.11, 2000, pp. 302-308, 2000.

[59] M. Milichovský, "Voda – klíčový fenomén při výrobě a užití papíru a papírenských výrobků (Water – the Key Phenomenon in Production and Utilisation of Paper Products)," *Chemické listy*, Vol. 94, No. 9, 2000, pp. 875-878.

[60] M. Milichovský, "Způsob dějů a jejich hodnocení probíhajících v papírenských suspenzích (Evaluation of phenomena taking place in paper suspension)," *Papír a celulóza*, Vol. 33, No. 7-8, 1978, pp.V61-V64, 1978.

[61] M. Milichovský and Bř. Češek, "Rheosedimentation – typical and characteristic phenomenon of paper matter," *Cellulose Chem. Technol*., Vol. 38, No. 5-6, 2004, pp. 385-397.

[62] M. Fišerová, J. Gigac and J. Balberčák, "Sedimentation properties of hardwood kraft pulp suspensions," *Papír a celulóza*, Vol. 64, No. 11-12, 2009, pp.362-364.

[63] M. Milichovský, "Behaviour of hydrophilic components in papermaking suspension. Part I. Interactions among hydrated particles – Theory of structural changes in hydrated layers," *Scientific Papers, University of Pardubice*, Vol. 56, 1992, pp. 123-154.

[64] M. Milichovský, "Teorie chování hydrofilních disperzních soustav III (Theory of behaviour of hydrophilich dispersion systems III. Experimental evidence of SCHL theory)," *Scientific Papers, University of Pardubice*, Vol. 51, 1988, pp. 149-168.

[65] B. Menaa, F. Menaa, C. Aiolfi-Guimaraes and O. Sharts, "Silica-based nanoporous sol-gel glasses: from bioencapsulation to protein folding studies," *International Journal of Nanotechnology*, Vol. 7, No. 1, 2010, pp. 1-45.

 

*Journal of Biomaterials and Nanobiotechnology*, **2010, 1, 31-36**
doi:10.4236/jbnb.2010.11004 Published Online October 2010 (http://www.SciRP.org/journal/jbnb)

# Measurement of Protein 53 Diffusion Coefficient in Live HeLa Cells Using Raster Image Correlation Spectroscopy (RICS)

**Sungmin Hong[1], Ying-Nai Wang[2], Hirohito Yamaguchi[2], Harinibytaraya Sreenivasappa[1], Chao-Kai Chou[2], Pei-Hsiang Tsou[1], Mien-Chie Hung[2], Jun Kameoka[1,2]**

[1]Department of Electrical and Computer Engineering, Texas A & M University, College Station, Texas, USA; [2]Department of Molecular and Cellular Oncology, University of Texas, M. D. Anderson Cancer Center, Houston, Texas, USA.
Email: kameoka@ece.tamu.edu, mhung@mdanderson.org

Received August 24th, 2010; revised September 14th, 2010; accepted October 21st, 2010.

## ABSTRACT

*We have applied Raster Image Correlation Spectroscopy* (*RICS*) *technique to characterize the dynamics of protein* 53 (*p*53) *in living cells before and after the treatment with DNA damaging agents. HeLa cells expressing Green Fluorescent Protein* (*GFP*) *tagged p*53 *were incubated with and without DNA damaging agents, cisplatin or eptoposide, which are widely used as chemotherapeutic drugs. Then, the diffusion coefficient of GFP-p*53 *was determined by RICS and it was significantly reduced after the drug treatment while that of the one without drug treatment was not. It is suggested that the drugs induced the interaction of p*53 *with either other proteins or DNA. Together, our results demonstrated that RICS is able to detect the protein dynamics which may be associated with protein-protein or protein-DNA interactions in living cells and it may be useful for the drug screening.*

***Keywords***: *Raster Image Correlation Spectroscopy, Diffusion Coefficient, p*53*, DNA Damage*

## 1. Introduction

Analysis of protein-protein or protein-DNA interaction is indispensable for current molecular biology to understand various signaling pathways that are essential for maintenance of cellular functions in living cells. To this end, several biochemical and molecular biological techniques have been developed, such as far western blot [1], co-immunoprecipitation [2], Mass spectrometry [3], electromobility shift assay (EMSA) [4], and chromatin immunoprecipitation (ChIP) [5]. Although these techniques have their own advantages, they require long process time and a large amount of samples. More importantly, these techniques do not provide the information regarding the high spatial and temporal interaction dynamics that may provide the novel insight into current biology. Thus, several techniques, for example, Single Particle Tracking (SPT) [6], Fluorescence Recovery after Photo bleaching (FRAT) [7], and Foster Resonance Energy Transfer (FRET) [8,9], have been developed to provide higher temporal/spatial resolution for molecular dynamics in living cells. Recently, Digman and coworkers introduced the new approach, called as Raster Image Correlation Spectroscopy (RICS), which enables to measure the protein dynamics in a living cell by using commercial laser scanning confocal microscope without adding additional expensive components. The detailed theories are described elsewhere [10-13]. Briefly, RICS can analyze the spatial fluctuation in the fluorescence signal, which is generated by the movement of fluorescence labeled molecules, to obtain molecular diffusion information.

The tumor-suppressor protein p53, that has been known as "the guardian of the genome," is frequently mutated or deleted in variety of human cancer types and plays an essential role in tumorigenesis [14]. In response to DNA damage, p53 is phosphorylated at several serine/threonine residues, resulting in its stabilization and activation [15]. Activated p53 forms a complex with multiple transcription co-factors and binds to promoter regions of target genes such as p21, Bax GADD45 and Puma that are involved in cell cycle arrest or apoptosis [16,17]. Cisplatin and etoposide are DNA damaging agents that have been used as chemotherapeutic drugs. Cisplatin unwind intra- and interstrand crosslinking of

 

DNA while etoposide disrupts DNA replication and repair by inhibiting topoisomerase II enzyme [18,19]. Thus, both anti-cancer agents damage to DNA that induce p53 accumulation and activation.

In this paper, we have investigated the effects of DNA damaging agents, cisplatin and etoposide, on p53 dynamics in living HeLa cells by using RICS. After the drug treatment, the significant reductions of p53 mobility were observed compared to the one without drug treatment. Both cisplatin and etoposide induced DNA damage that stabilized and activated p53, resulting in the formation of the DNA-p53-transcription co-factors complex. Therefore, the results obtained by RICS explain the p53 dynamics in living cells.

## 2. Materials and Methods

### 2.1. Cell Culture and Plasmid Preparation, Transfection, and Drug Treatment

Human cervical cancer, HeLa cells were obtained from American Type Culture Collection (ATCC) and maintained in DMEM/F12 medium supplemented with 10 % fetal bovine serum and antibiotics. pEGFP-C2 was obtained from Clontech laboratories. p53 Open Reading Frame was digested out from pcDNA3-myc-p53 with EcoRI and XhoI, and ligated into pEGFP-C2 EcoRI/SalI sites. pcDNA3-myc-p53 was prepared by polymerase chain reaction (PCR) and described previously [20]. EGFP empty vector or GFP-p53 expression plasmid was transfected into HeLa cells using electroporation. After 24 hours transfection, the cells were seeded in 50 mm Glass Bottom culture dish (MatTek Corp.) at around 50 % density and cultured for additional 12 hours. Since our preliminary experiments showed that over 50 μM drugs induced apoptotic cell death after 24 hours, the cell samples were treated or untreated with either 20 μM cisplatin (Sigma) or 20 μM etoposide (Sigma) for the different periods of time and subjected to confocal microscopy analysis.

### 2.2. Confocal Microscope

The confocal fluorescent microscopy (Olympus FV100) equipped with air-cooled 488nm argon ion laser was employed for this study (**Figure 1**). The series of images were collected using 60X water immersion objective (NA = 1.2). The scan speed was set at 12.5 μs/pixel. The scan area was 256 × 256 pixels and 100 frames were collected for each sample. The corresponding line and the frame time were 4.325 ms and 1.150 s, respectively. 488 nm wavelength of laser with 1.5 % power was used for the GFP excitation, and emission spectrum was filtered between 500 and 600 nm. The microscope was operated in the pseudo photon counting mode. The beam waist radius was calibrated using 10 nM fluorescein in 0.01 M NaOH at the beginning of experiment, and it was 0.5 μm. The collected fluorescence data were analyzed using the Globals software package developed at the Laboratory for Fluorescence Dynamics at the University of California at Irvine [21].

## 3. Results

**Figure 2** showed the RICS analysis for GFP alone in living HeLa cells immediately after adding cisplatin and etoposide. The diffusion coefficients were measured every 4 hours after adding the drugs. The GFP samples were used to calibrate the RICS analysis. The autocorrelation spectrum after background subtraction showed that GFP diffused freely into the nucleus. The measured diffusion coefficients of GFP were 38.26 ± 5.62 $\mu m^2/s$ (cistplatin-treated) and 41.32 ± 9.81 $\mu m^2/s$ (etoposide-treated) at the 0 hour. Also, consistent values were observed over time (43.73 ± 6.57 $\mu m^2/s$ and 44.36 ± 6.82 $\mu m^2/s$ at the 16 hour) as shown in **Table 1**.

To compare the dynamics of p53 in response to DNA damaging agents, HeLa cells expressing GFP-tagged p53 were exposed to cisplatin or etoposide and subjected to RICS analysis. We first collected 100 frame images of GFP-p53 immediately after drugs treatment. Following, GFP-p53 in HeLa cells treated with the drugs were monitored every 4 hours upto 16 hours.

**Figure 3** showed the auto-correlation of confocal images and fitting of the spatial correlation function at 16 hours after drugs treatment. These results suggest that GFP-p53 interacts with other molecules such as proteins and DNAs after the drug treatment and, as a result, the diffusion coefficients were reduced. As shown in **Figure 4**, the measured diffusion coefficients of GFP-p53 were 19.92 ± 3.64 $\mu m^2/s$ and 18.76 ± 2.68 $\mu m^2/s$ immediately after adding cisplatin and etoposide, repectively, and these results were in a good agreement with previous

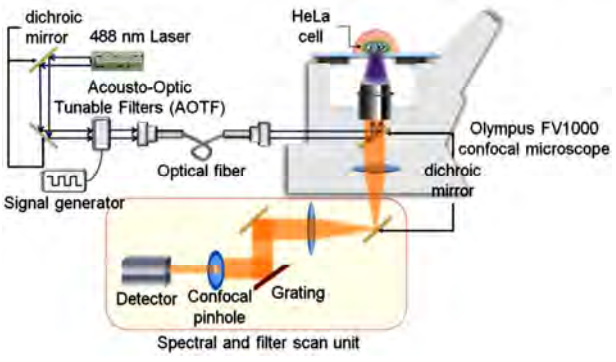


**Figure 1. Schematic diagram of system setting.**

 

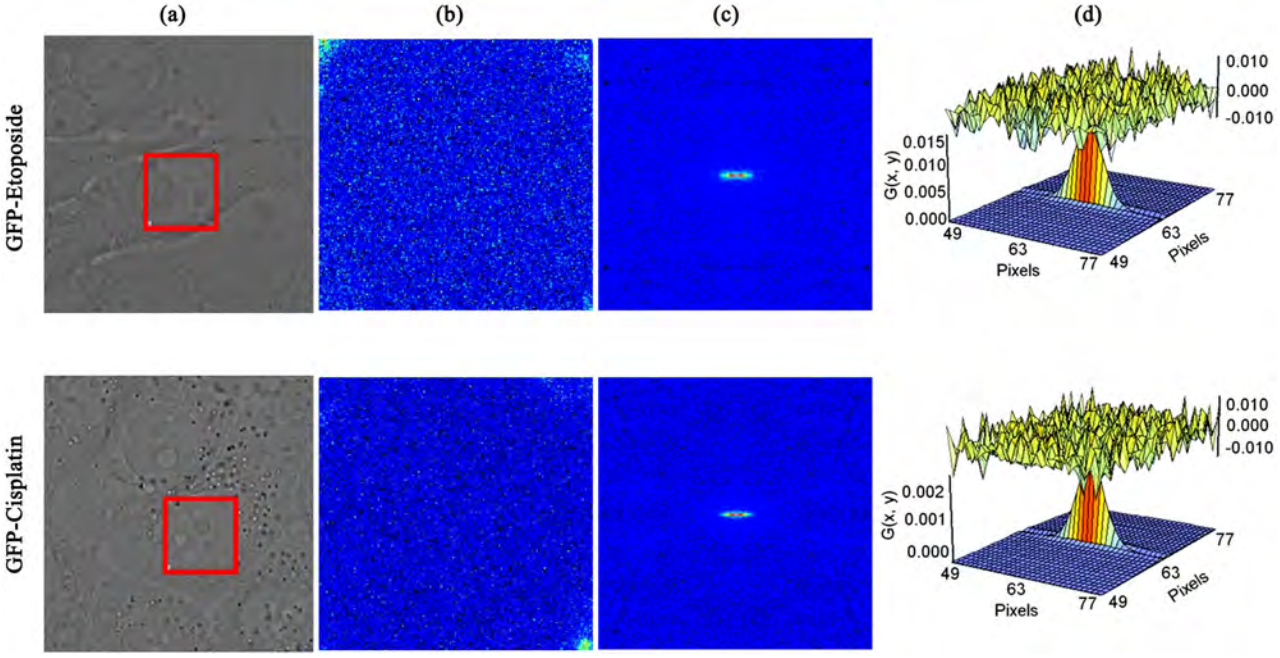


**Figure 2. RICS analysis of GFP in live HeLa cells at 0 hour after anti-cancer drugs treatment. (a) Optical images of HeLa cell with the region of interest (ROI) for RICS analysis, (b) intensity images of ROI (nucleus), (c) RICS autocorrelation function of 128 × 128 pixels, (d) fit (lower surface) and residues (upper surface) of the spatial correlation function.**

**Table 1. Summary of diffusion coefficient in the nuleus of HeLa cells.**

| | | Diffusion Coefficient ($\mu m^2/s$) | | | | |
|---|---|---|---|---|---|---|
| | | *0 hr* | *4 hr* | *8 hr* | *12 hr* | *16 hr* |
| Cisplatin | GFP | 38.26 ± 5.62 | 37.55 ± 5.67 | 42.65 ± 9.46 | 44.72 ± 9.14 | 43.73 ± 6.57 |
| | GFP-p53 | 19.92 ± 3.64 | 8.23 ± 5.78 | 3.25 ± 0.38 | 3.21 ± 1.18 | 3.28 ± 2.87 |
| Etoposide | GFP | 41.32 ± 9.81 | 36.54 ± 6.61 | 41.21 ± 8.29 | 44.72 ± 8.97 | 44.36 ± 6.82 |
| | GFP-p53 | 18.76 ± 2.68 | 12.77 ± 5.42 | 3.05 ± 0.60 | 3.57 ± 1.08 | 3.25 ± 1.36 |

reported result (15.4 ± 5.6 $\mu m^2/s$) [22]. The diffusion dynamics of GFP-p53 were gradually decreased over time, and significant reductions of GFP-p53 mobility were observed at 8 hr after drugs injection, (3.25 ± 0.38 $\mu m^2/s$ for cisplatin and 3.05 ± 0.60 $\mu m^2/s$ for etoposide).Then, it maintained the constant values after 8 hr in the presence of both drugs. The diffusion dynamics changes of GFP-p53 in response to the drugs were summarized in **Table 1**.

## 4. Discussion

In this work, we measured the diffusion coefficient of GFP-tagged p53 in the nucleus of HeLa cells using RICS approach. Also, DNA damaging agents were used to verify p53 dynamics in response to DNA damage.

The diffusion coefficients of GFP obtained by RICS were agreed well with previously reported value. Hinow et al. applied free diffusion model to explain the mobility of GFP in the nucleus of H1299 human large cell lung carcinoma cell using confocal FRAP technique, and they reported the diffusion coefficient of GFP (41.6 ± 13.6 $\mu m^2/s$) [22]. Since GFP was not involved in DNA damage response, the diffusion of GFP was not affected by anti-cancer drugs. This demonstrated that RICS method could provide the stable result in measuring diffusion coefficient in living HeLa cells.

After DNA damaging agent treatment, the significant reductions in GFP-p53 mobility were observed in the nucleus. It is well known that p53 is stabilized and activated in response to DNA damage [23]. In this study,

 

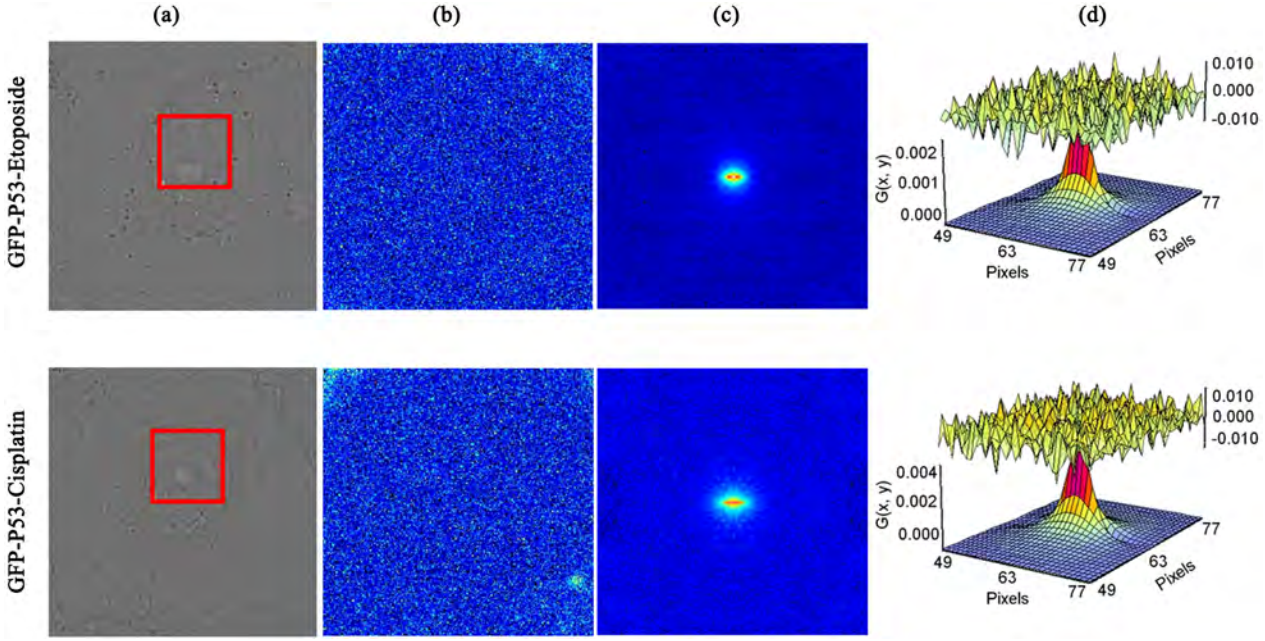


**Figure 3. RICS analysis of GFP-p53 in live HeLa cells at 16 hours after anti-cancer drugs treatment. (a) optical images of HeLa cell with the region of interest (ROI) for RICS analysis, (b) intensity images of ROI (nucleus), (c) RICS autocorrelation function of 128×128 pixels, (d) fit (lower surface) and residues (upper surface) of the spatial correlation function.**

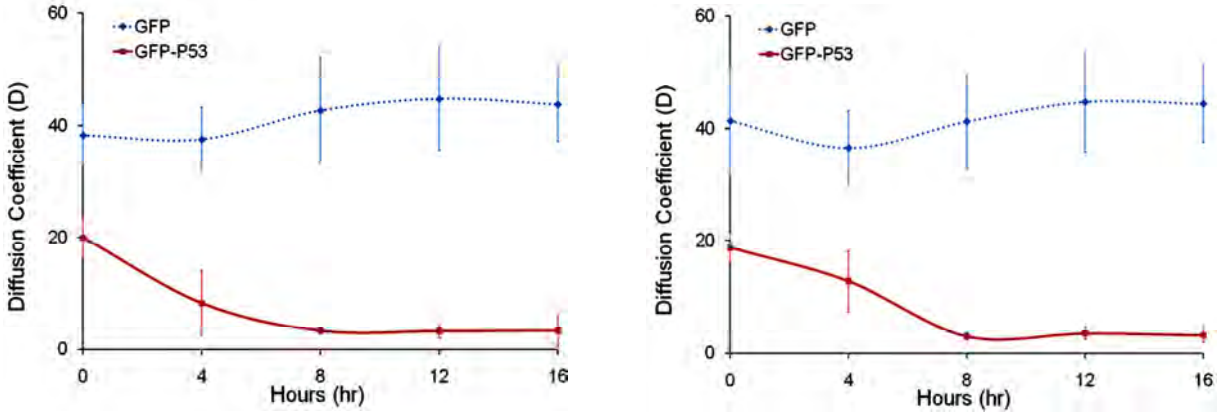


(a) (b)

**Figure 4. The diffusion coefficient graph as a function of time. (a) diffusion dynamics changes of GFP or GFP-p53 in cisplatin treated cells, (b) diffusion dynamics changes of GFP or GFP-p53 in etoposide treated cells.**

20 μM concentrations of cisplatin and etoposide were used. It would be expected that higher concentration of drugs induces the quicker reduction of the mobility of GFP-p53 due to the p53 activation by more DNA damage. Furthermore, it has been known that ciplatin induces single stranded break of DNA[24] while etopside causes double stranded break of DNA[25]. Thus, the combination of these drugs induces more DNA damage, and it also would be expected that the combination of both drugs induces the quicker reduction of the mobility of GFP-p53.

Moreover, it has been shown that p53 translocates from cytosol to the nucleus after DNA damage. Activated p53 form a complex with multiple transcriptions co-factors and binds to the specific promoter region in DNA to induce target genes within 8 hours. As a result, p53 mobility was expected to be decreased. Our results for fluctuations of GFP-p53 diffusion coefficients were consistent with our prediction from the current knowledge regarding p53.

 

## 5. Conclusions

In conclusion, we have successfully measured the diffusion coefficients of GFP-p53 in living HeLa cells subjected to DNA damage agents by using commercial confocal microscope to RICS analysis method. RICS is able to measure protein diffusion in live cells using regular confocal microscope and require relatively short period of time. Therefore, it may be applied to a large-scale, high throughput drug screening based on the activation or inactivation of tumor suppressors or oncogene products in the future.

## 6. Acknowledgements

This project has been supported by the CMUH Cancer Research Center of Excellence DOH 99-7D-C-111-005, Taiwan, Institute of Basic Science, China Medical University and Hospital/M. D. Anderson Cancer Center Sister Institution Fund, CCSG CA16672, NIH R 01 CA109311, NIH PO1 099031, and US Army Department Breast Cancer Research Program W81XWH-08-1-0649-01 to M.-C.H.; NIH R21 CA135318-01A1 and US Army Department Breast Cancer Research Program W81XWH-08-1-0644 to J.K. The use of the Micrsoscopy and Imaging Center facility at Texas A & M University is acknowledged. The Olympus FV1000 confocal microscope acquisition was supported by the Office of the Vice President for Research at Texas A & M University.

## REFERENCES

[1] Y. Wu, Q. Li and X.-Z. Chen, "Detecting Protein-Protein Interactions by Far Western Blotting," *Nat. Protocols*, Vol. 2, No. 12, 2007, pp. 3278-3284.

[2] P. Yaciuk, "Co-Immunoprecipitation of Protein Com-plexes," *Methods in Molecular Medicine*, Vol. 131, 2007, pp. 103-111.

[3] D. Figeys, L. D. McBroom and M. F. Moran, "Mass Spectrometry for the Study of Protein-Protein Interac-tions," *Methods*, Vol. 24, No. 3, 2001, pp. 230-239.

[4] M. Gaudreault, M.-E. Gingras, M. Lessard, S. Leclerc and S. L. Guérin, "Electrophoretic Mobility Shift Assays for the Analysis of DNA–Protein Interactions," *Methods in Molecular Biology*, Vol. 543, 2009, pp. 15-35.

[5] B. G. Hoffman and S. J. M. Jones, "Genome-wide Identification of DNA-protein Interactions Using Chromatin Immunoprecipitation Coupled with Flow Cell Sequencing," *Journal of Endocrinol*, Vol. 201, No. 1, 2009, pp. 1-13.

[6] K. Jaqaman, D. Loerke, M. Mettlen, H. Kuwata, S. Grin-stein, S. L. Schmid, et al., "Robust Single-particle Tracking in Live-cell Time-lapse Sequences," *Nature Methods*, Vol. 5, No. 8, 2008, 695-702.

[7] D. Axelrod, D. E. Koppel, J. Schlessinger, E. Elson and W. W. Webb, "Mobility Measurement by Analysis of Fluorescence Photobleaching Recovery Kinetics," *Biophysical Journal*, Vol. 16, No. 9, 1976, pp. 1055-1069.

[8] P. Roy, Z. Rajfur, P. Pomorski and K. Jacobson, "Microscope-based Techniques to Study Cell Adhesion and Migration," *Nature Cell Biology*, Vol. 4, No. 4, 2002, pp. E91-E96.

[9] I. A. Demarco, A. Periasamy, C. F. Booker and R. N. Day, "Monitoring Dynamic Protein Interactions with Photoquenching FRET," *Nature Methods*, Vol. 3, No. 7, 2006, pp. 519-524.

[10] M. A. Digman, P. Sengupta, P. W. Wiseman, C. M. Brown, A. R. Horwitz and E. Gratton, "Fluctuation Correlation Spectroscopy with a Laser-Scanning Microscope: Exploiting the Hidden Time Structure," *Biophysical Journal*, Vol. 88, No. 5, 2005, pp. L33-L36.

[11] M. A. Digman, C. M. Brown, P. Sengupta, P. W. Wise-man, A. R. Horwitz and E. Gratton, "Measuring Fast Dynamics in Solutions and Cells with a Laser Scanning Microscope," *Biophysical Journal*, Vol. 89, No. 2, 2005, pp, 1317-1327.

[12] C. M. Brown, R. B. Dalal, B. Hebert, M. A. Digman, A. R. Horwitz and E. Gratton, "Raster Image Correlation Spectroscopy (RICS) for Measuring Fast Protein Dynamics and Concentrations with a Commercial Laser Scanning Confocal Microscope," *Journal of Microscopy*, Vol. 229, No. 1, 2008, pp. 78-91.

[13] M. A. Digman and E. Gratton, "Analysis of Diffusion and Binding in Cells using the RICS Approach," *Microscopy Research and Technique*, Vol. 72, No. 4, 2009, pp. 323-332.

[14] [14] K. M. Ryan, A. C. Phillips and K. H. Vousden, "Regulation and Function of the p53 Tumor Suppressor Protein," *Current Opinion in Cell Biology*, Vol. 13, No. 3, 2001, pp. 332-337.

[15] A. M. Bode and Z. Dong, "Post-translational Modification of p53 in Tumorigenesis," *Nature Reviews Cancer*, Vol. 4, No. 10, 2004, pp. 793-805.

[16] O. Laptenko and C. Prives, "Transcriptional Regulation by p53: One Protein, Many Possibilities," *Cell Death & Differentiation*, Vol. 13, No. 6, 2006, pp. 951-961.

[17] J. K. Sax and W. S. El-Deiry, "p53 Downstream Targets and Chemosensitivity," *Cell Death & Differentiation*, Vol. 10, No. 4, pp. 413-417.

[18] M. Jiang, X. Yi, S. Hsu, C.-Y. Wang and Z. Dong, "Role of p53 in Cisplatin-induced Tubular Cell Apoptosis: Dependence on p53 Transcriptional Activity," *American Journal of Physiology Renal Physiology*, Vol. 287, No. 6, 2004, pp. F1140-1147.

[19] P. J. Smith, (1990), "DNA Topoisomerase Dysfunction: A New Goal for Antitumor Chemotherapy," *BioEssays*, Vol. 12, No. 4, pp. 167-172.

[20] H. Yamaguchi, N. T. Woods, L. G. Piluso, H.-H. Lee, J. Chen, K. N. Bhalla, *et al*., "p53 Acetylation Is Crucial for Its Transcription-independent Proapoptotic Functions,"

 

*Journal of Biological Chemistry*, Vol. 284, No. 17, 2009, 11171-11183.

[21] J. Beechem, E. Gratton, M. Ameloot, J. Knutson and L. Brand, "The Global Analysis of Fluorescence Intensity and Anisotropy Decay Data: Second-Generation Theory and Programs," *Topics in Fluorescence Spectroscopy*, Vol. 2, 2002, pp. 241-305.

[22] P. Hinow, C. E. Rogers, C. E. Barbieri, J. A. Pietenpol, A. K. Kenworthy and E. DiBenedetto, "The DNA Binding Activity of p53 Displays Reaction-Diffusion Kinetics," *Biophysical Journal*, Vol. 91, No. 1, 2006, pp. 330-342.

[23] D. P. Lane, "p53, guardian of the genome," *Nature*, Vol. 358, No. 6381, 1992, pp. 15-16.

[24] L. Yen, N. Zeng-Rong, X.-L. You, S. Richard, B. C. Langton-Webster and M. A. Alaoui-Jamali, "Regulation of Cellular Response to Cisplatin-induced DNA Damage and DNA Repair in Cells Overexpressing p185erbB-2 is Dependent on the Ras Signaling pathway," *Oncogene*, Vol. 14, No. 15, 1997, pp. 1827-1835.

[25] S. A. S. Walles, R. Zhou and E. Liliemark, "DNA Damage Induced by Etoposide; A Comparison of Two Different Methods for Determination of Strand Breaks in DNA," *Cancer Letters*, Vol. 105, No. 2, 1996, pp. 153-159.

 

*Journal of Biomaterials and Nanobiotechnology*, **2010, 1, 37-41**
doi:10.4236/jbnb.2010.11005 Published Online October 2010 (http://www.SciRP.org/journal/jbnb)

# Effect of Nano - Titanium Dioxide with Different Antibiotics against Methicillin-Resistant *Staphylococcus Aureus*

**Aashis S. Roy[1], Ameena Parveen[2], Anil R. Koppalkar[3], M. V. N. Ambika Prasad[1*]**

[1]Department of Materials Science, Gulbarga University, Gulbarga, Karnataka, India; [2]Department of Physics, Gurmithkal, Yadgir, Karnataka, India; [3]Materials Science Lab, S. S. Margol College, Shahabad, Gulbarga, Karnataka, India.
Email: *amb1_prasad@rediffmail.com

Received June 14th, 2010; revised June 25th, 2010; accepted June 30th, 2010.

## ABSTRACT

*The different investigation has been carried out on the biological activities of titanium dioxide nanoparticle but the effect of this nano product on the antibacterial activity of different antibiotics has not been yet demonstrated. In this study the nano size $TiO_2$ is synthesized using citric acid and alpha dextrose and the enhancement effect of $TiO_2$ nanoparticle on the antibacterial activity of different antibiotics was evaluated against Methicillin-resistant Staphylococcus aureus (MRSA). During the present study, different concentrations of nano-scale $TiO_2$ were tested to find out the best concentration that can have the most effective antibacterial property against the MRSA culture. Disk diffusion method was used to determine the antibacterial activity of these antibiotics in the absence and presence of sub inhibitory concentration of $TiO_2$ nano particle. A clinical isolate of MRSA, isolated from Intensive Care Unit (ICU) was used as test strain. In the presence of sub-inhibitory concentration of $TiO_2$ nanoparticle (20 µg/disc) the antibacterial activities of all antibiotics have been increased against test strain with minimum 2 mm to maximum 10mm. The highest increase in inhibitory zone for MRSA was observed against pencillin G and amikacin (each 10 mm). Conversely, in case of nalidixic acid, $TiO_2$ nanoparticle showed a Synergic effect on the antibacterial activity of this antibiotic against test strain. These results signify that the $TiO_2$ nanoparticle potentate the antimicrobial action of beta lactums, cephalosporins, aminoglycosides, glycopeptides, macrolids and lincosamides, tetracycline a possible utilization of nano compound in combination effect against MRSA.*

***Keywords:*** *Nano - Titanium Oxide, S. Aureus, Drug Resistance, Antibacterial Activity*

## 1. Introduction

Methicillin-resistant *Staphylococcus aureus* (MRSA) is one of the major nosocomial pathogens responsible for a wide spectrum of infections, including skin and soft tissue infections, pneumonia, bacteraemia, surgical site infections (SSI), catheter related infections [1]. Intensive care unit characteristically has higher rates of infections and increased transmission rates, high antibiotic use and large numbers of vulnerable patients [2]. The emergence of bacterial resistance to antibiotics and its dissemination, however, are major health problems, leading to treatment drawbacks for a large number of drugs [3,4]. Consequently there has been increasing interest in the use of inhibitors of antibiotic resistance for combination therapy [5,6].

Nanostructured materials are attracting a great deal of attention because of their potential of achieving specific processes and selectivity, especially in biological and pharmaceutical applications [7-9]. Gold, silver and copper have been used mostly for the synthesis of stable dispersions of nanoparticles [10,11]. A unique characteristic of these synthesized metal particles is that a change in the absorbance or wave length gives a measure of the particle size, shape and interparticle properties [12]. Nanomaterials are called “a wonder of modern medicine”. It is stated that antibiotics kill perhaps a half dozen different disease-causing organisms but nanomaterials can kill some 650 cells [13]. Resistant strains fail to develop if we apply nanoparticles based formulations in their culture media.

The antibacterial activity of $TiO_2$ has been found to be due to a reaction of the $TiO_2$ surface with water. On exposure to ultraviolet (UV) irradiation, $TiO_2$ releases free radicals such as OH, $O_2^-$, $HO_2$-, and $H_2O_2$. This

 

potent oxidizing power characteristically results in case of bacteria and other organic substances [14-16]. The small nanometer-scale $TiO_2$ particles impose several effects that govern its antibacterial action we examined the antimicrobial activity of nanostructured titanium dioxide with different antibiotics against MRSA. The different investigation has been carried out on the biological activities of titanium dioxide nanoparticle but the combination effects of this product with different antibiotics have not been demonstrated. The nanocrystalline particles of $TiO_2$ are synthesized using ultrasonic irradiation, and the particle sizes are controlled using different solvents during the sonication process.

Objectives of the present study are (i) synthesis of nano size titanium dioxide using citric acid and alpha dextrose (ii) analyse the effect of Titanium nanoparticles on the antibacterial activity of different antibiotics against MRSA (iii) estimation of MRSA growth in the presence of $TiO_2$ nanoparticles have been reported having an extremely good safety profile and no toxicity observed when taken at different nanosize. Taken together, this compound as a highly safe compound may be considered for combination therapy against MRSA, due its potential synergetic effect with important antibiotics such as beta lactums, cephalosporins, aminoglycosides.

## 2. Materials and Methods

Titanium dioxide particles preparation: In the following, the two step sol-gel preparation method used is described detail. Nanocrystalline titanium dioxide was prepared by employing citric acid route were saturated solution of α-Dextrose used as a surfactant.

Two separate solutions were prepared. In first step: titanium nitrate and citric acid are taken in 1:3 and are thoroughly stirred using magnetic stirrer with ammonia solution at 80˚C about 5-6 hrs. Ammonia solution is used to maintain the pH 4 of solution. Finally a gel is formed. In second step, saturated solution of alpha dextrose is added and stirred for 1hr at 120˚C to the spongy type gel of nanoscaled $TiO_2$ formed. This spongy gel is ignited at a temperature of about 300˚C for 1 hr. At this temperature a combustion process takes place in the spongy gel containing citric acid a result of it we have nanostructured titanium dioxide.

## 3. X-Ray Diffraction (XRD)

X-ray diffraction Phase identification was carried out by X-Ray powder diffraction at ambient temperature. A Shintag X1 diffractometer with Cu Kα (1.54 A) radiation in θ – θ configuration was used. The patterns were recorded in the 2-70 range at 0.05 step size using 3-s acquisition time per step. The mean particle size was calculated using the Debye–Scherrer Equation 1 in which K is a constant equal to 0.9, λ is the wavelength of the Cu Kα radiation, β is the half peak width of the diffraction peak in radiant and θ is the Braggs angle of (311) plane.

$$\tau = K\lambda/\beta\cos\theta \quad (1)$$

*Staphylococcus aureus* was isolated from Clinical specimens collected from ICU of Durgabai Deshmukh Hospital and Research Center and Osmania Hospital, Hyderabad, South India. Oxacillin-disc diffusion method was done for identification of methicillin-resistance. This MRSA was used as test strain. Antibiotic susceptibility test was performed for the test strain (MRSA) against 23 antibiotics by disc agar diffusion method (DAD) on Muller-Hinton agar (Himedia, India), according to the guidelines recommended by National Committee for Clinical Laboratory Standards (NCCLS) [17].

## 4. Disk Diffusion Assay to Evaluate Combined Effects

To determine combined effects, each standard paper disc was further impregnated with sub-inhibitory concentration of titanium dioxide nanoparticle (10 µg/disc). A single colony of test strains were grown overnight in Muller-Hinton broth medium on a rotary shaker (200 rpm) at 35˚C. The inoculums were prepared by diluting the overnight cultures with 0.9% NaCl to a 0.5 McFarland standard and were applied to the plates along with the standard and prepared disks containing of titanium dioxide nanoparticle (10 µg/disc). Clinical isolates of MRSA from our culture collection were used as test strains. After incubation at 37˚C for 24 hrs, the zones of inhibition were measured. The assays were performed in triplicate.

## 5. Estimation of MRSA Growth in the Presence of Nanocrystalline $TiO_2$

The 2 mL of the overnight-cultured MRSA was added to 100 mL nutrient broth, containing 0.12% glucose with and without 0.01, 0.5 and 1% nano-$TiO_2$ and incubate at 30˚C for 24 hrs. Optical density measurements were taken at 600 nm to monitor the bacterial concentration.

## 6. Results and Discussions

The nano size titanium dioxide is synthesized using citric acid and alpha dextrose. The small nanometer scale $TiO_2$ particles as seen in the **Figure 1** will impose several effects that govern its antibacterial action. The X-ray diffraction pattern shows cubic peaks of $TiO_2$, which indicates the nanocrystalline nature of pure nanostructured titanium dioxide and is shown in the **Figure 2**. By comparing the XRD pattern standard JCPS data (432-161) of $TiO_2$, indicating the prominent peaks corresponding to $2\theta = 27^{\circ}$, $39^{\circ}$, $48^{\circ}$, $55^{\circ}$ and $63^{\circ}$ are due to (110), (200), (112),

 

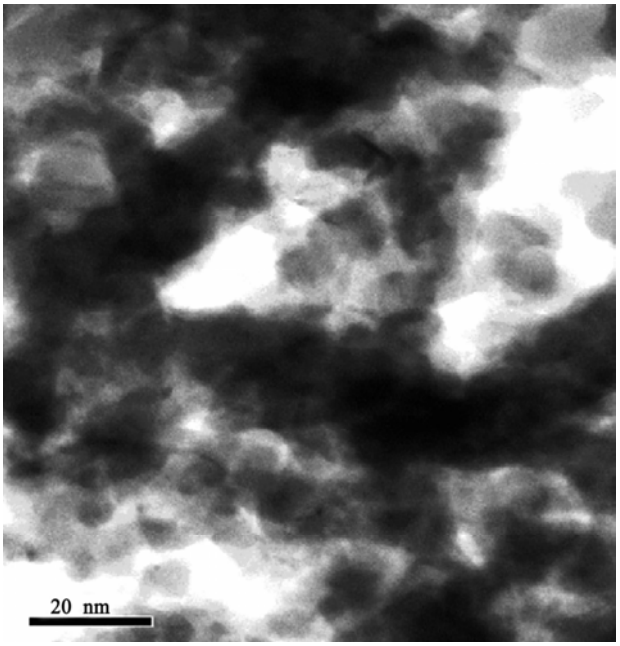


**Figure 1. Showing TEM image of $TiO_2$ nanoparticles.**

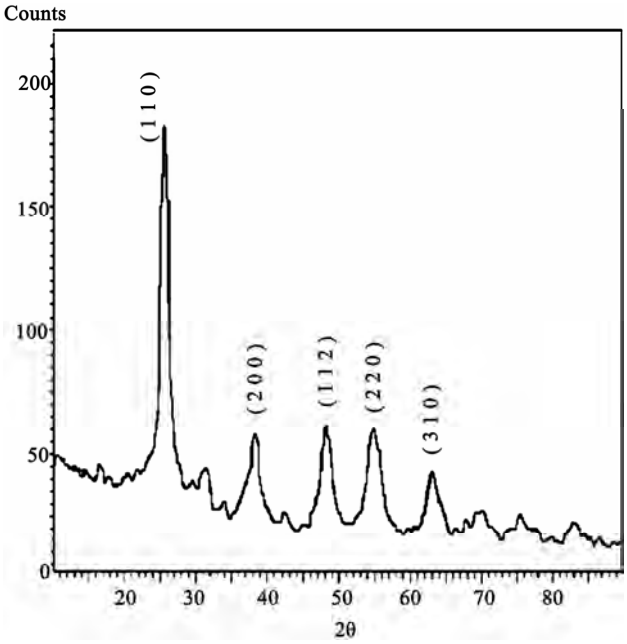


**Figure 2. XRD pattern of $TiO_2$.**

(220) and (310) planes which indicates formation of single phase titanium dioxide. The crystalline size of the Titanium dioxide is calculated by using debye-scharrer equation and it was found to be around 20 nm. Titanium dioxide has a very good potential to move into the clinic [18]. In this investigation the effect of $TiO_2$ nanoparticle on the antibacteria of different antibiotics was investtigated against MRSA using disk diffusion method. The antimicrobial resistance of MRSA against various antibiotics is increased without nano-$TiO_2$ and decreases with nanoscaled $TiO_2$. The diameter of inhibition zones (mm) around the different antibiotic discs with $TiO_2$ and without titanium dioxide nanopatrticles against test strain are shown in [**Table 1**].

The antibacterial activities of all antibiotics have been increased in the presence of nanosize titanium dioxide against test strain. The highest antibacterial activities increases in area were observed for penicillin and amikacin (10 mm) followed by ampicillin and Gentamycin (in each 09 mm), oxacillin, cloxacillin (08 mm), amoxycillin, cephalexin, cefotoxime, ceftazidime, vancomycin, streptomycin (in each 07 mm) erythromycin, clindamycin (06 mm) and tetracyclin (05 mm). The moderate increases in inhibition zone areas for ciprofloxacin, rifampicin, sulphazidime and cotrimoxazole (04 mm).The lowest increase in inhibition zone area against the Chloramphenicol (03 mm) followed by norfloxacin and clarithromycin (02 mm).

Conversely, for nalidixic acid, titanium dioxide nanoparticle shows no effect on the antibacterial activity of this antibiotic against the test strain. It should be pointed out that the titanium dioxide nanoparticle content of 10 µg/disc was chosen to guarantee that the effect produced was due to the combination and not to the effect of the $TiO_2$ nanoparticle itself. So the effect observed in this condition could be due to the antibiotic-titanium dioxide nanoparticle combination. At the concentration tested, $TiO_2$ nanoparticle significantly improved antibiotic efficacy against *S. aureus* when combined with beta lactums, cephalosporins, aminoglycosides.

The optical density of the medium was investigated as the number of bacteria after contact with the nano- particles. **Figure 3** shows the growth of MRSA at diff- erent concentrations and the effect of different 0.01, 0.5 and 1% nano-$TiO_2$ on the in growth and killing of MRSA. As demonstrated by the figure, 0.01% nano-$TiO_2$ did not have antibacterial efficiency on MRSA but the concentrations of 0.5 and 0.1% nano-$TiO_2$ inhibited the bacterial growth. Also shows that 0.5% nano-$TiO_2$ showed 1.9 times decrease the optical density of bacterial cultures as compared to the control. While, in the presence of 1% nano-$TiO_2$, the optical density of MRSA cultures decreased 4.5 times as compared to the control experiment.

A study states the nano-$TiO_2$ as a strong and effective bactericidal agent [18]. During the present study, different concentrations of nanosized $TiO_2$ were tested to find out the best concentration that can have the most effective antibacterial property against the MRSA culture. This is the first report of combination effect of $TiO_2$ nanoparticles with different antibiotics. Today, $TiO_2$

 

**Table 1. the comparative activities of various antibiotics and antibiotic with Nanosized$TiO_2$ against MRSA.**

| Sl. No. | Antibiotics | Symbol | Inhibition Zone of Antibiotic (mm) | Inhibition Zone of Antibiotic with $TiO_2$ (20nm) in (mm) | Increased zone size (mm) |
|---|---|---|---|---|---|
| **1** | **B-lactams** | | | | |
| 01. | Penicillin G | P (10U) | 34 | 44 | 10 |
| 02. | Oxacillin | Wx (1 µg) | 11 | 19 | 08 |
| 03. | Cloxacillin | Cx (30 µg) | 19 | 27 | 08 |
| 04. | Ampicillin | A (10 µg) | 29 | 38 | 09 |
| 05. | Amoxycillin | Am (25 µg) | 20 | 26 | 07 |
| **2** | **Cephalosporins** | | | | |
| 06. | Cephalexin | Cp (30 µg) | 25 | 32 | 07 |
| 07. | Cefotoxime | CX (30 µg) | 24 | 33 | 07 |
| 08. | Ceftazidime | Ca (30 µg) | 16 | 23 | 07 |
| **3** | **Glycopeptides** | | | | |
| 09. | Vancomycin | V (30 µg) | 15 | 22 | 07 |
| **4** | **Aminoglycosides** | | | | |
| 10. | Amikacin | Ak (10 µg) | 15 | 25 | 10 |
| 11. | Gentamycin | G (50 µg) | 14 | 24 | 09 |
| 12. | Streptomycin | S (25 µg) | 13 | 19 | 07 |
| **5** | **Flouroquinolones** | | | | |
| 13. | Ciprofloxacin | Cf (5 µg) | 20 | 24 | 04 |
| 14. | Norfloxacin | No (10 µg) | 15 | 17 | 02 |
| **6** | **Azlides** | | | | |
| 15. | Clarithromycin | Cw (15 µg) | 17 | 19 | 02 |
| **7** | **Macrolides** | | | | |
| 16. | Erythromycin | E (15 µg) | 15 | 21 | 06 |
| **8** | **Lincosamides** | | | | |
| 17. | Clindamycin | Cl (10 µg) | 20 | 26 | 06 |
| **9** | **Sulphonamides** | | | | |
| 18. | Cotrimoxazole | Co (25 µg) | 17 | 21 | 04 |
| 19. | Nalidixicacid | Na (30 µg) | 16 | 16 | 00 |
| 20. | Rifampicin | R (15 µg) | 25 | 29 | 04 |
| 21. | Tetracyclin | T (30 µg) | 21 | 26 | 05 |
| 22. | Sulphazidime | Sz (25 µg) | 12 | 17 | 04 |
| 23. | Chloramphenicol | C (30 µg) | 18 | 21 | 03 |

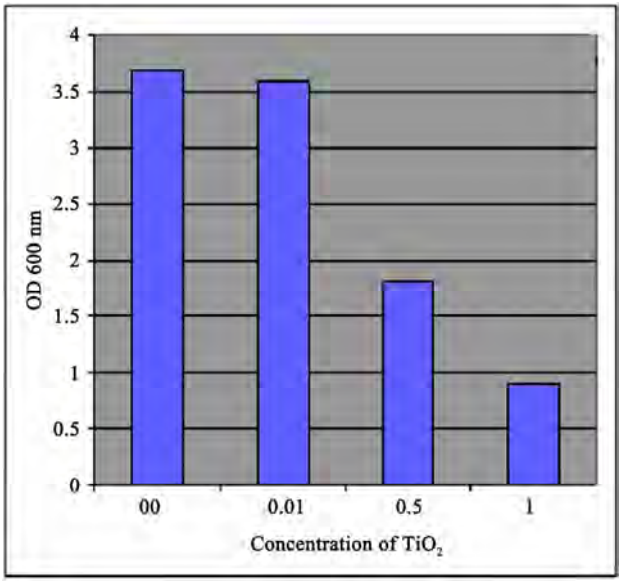


**Figure 3. MRSA growth at different concentrations of $TiO_2$.**

nanoparticle are cosmetic ingredient has drawn the attention of scientists because of its extensive pharmaceutical properties. In different phases, clinical trials, no toxicity except mild dehydration was observed when taken at doses as high as g/day and it is reported as an attractive choice for many disease therapies.

Recently some metal nanoparticles have been evaluated for increasing the antibacterial activities of different antibiotics. Several investigations have suggested the possible mechanisms involving the interaction of nanomaterials with the biological molecules. It is believed that microorganisms carry a negative charge while metal oxides carry a positive charge. This creates an "electromagnetic" attraction between the microbe and treated surface. Once the contact is made, the microbe is oxidized and dead instantly. Generally, it is believed that nanomaterials release ions, which react with the thiol group (-SH) of the proteins present on the bacterial surface. Such proteins protrude through the bacterial cell membrane, allowing the transport of nutrients through the cell wall. Nanomaterials inactivate the proteins, decreasing the membrane permeability and eventually causing the cellular death [19]. In this study using disk diffusion assay we showed that the antibacterial activity of

 

beta lactums, cephalosporins, aminoglycosides, glycolpeptides, erythromycin, clindamycin and tetracycline can be increased by $TiO_2$ nanoparticles. Therefore, this compound or its future derivatives have a good potential for combination effect against MRSA.

## 7. Conclusions

The synthesis of nanosize titanium dioxide of 20nm was carried out successfully using citric acid and alpha dextrose as double surfactants. The small nanometer scale $TiO_2$ particles which impose several effects that govern its antibacterial action. The antibacterial activities at different concentrations of nano-$TiO_2$ were investigated. The antimicrobial resistance of MRSA against various antibiotics is increased without nano-$TiO_2$ and decreases with nano-$TiO_2$. Need the further work to find out the exact reason to for enhancement of activity of antibiotics in presence of $TiO_2$ nanoparticles.

## REFERENCES


[1] N. De San, O. Denis, M. F. Gasasira , R. De Mendonca , C. Nonhoff and M. J. Struelens, "Controlled Evaluation of the IDI-MRSA Assay for Detection of Colonization by Methicillin-Resistant, *Staphylococcus aureus* in Di- verse Mucocutaneous Specimens," *Journal of Clinical Microbiology*, 2007, Vol. 45, No. 4, pp. 1098-1101.

[2] N. Safdar and D. G. Maki, "The Community of Risk Factors for Nosocomial Colonization and Infection with Anti-Microbial-Resistant *Staphylococcus aureus*, Entero-Coccus, Gramnegative Bacilli, Clostridium Difficile and Candida," *Annals of Internal Medicine*, Vol. 136, 2002, pp. 834-844.

[3] L. C. Braga, A. A. Leite, K. G. Xavier , J. A. Takahashi, M. P. Bemquerer, E. Chartone-Souza, *et al*., "Synergic Interaction between Pomegranate Extract and Antibiotics against *Staphylococcus Aureus*," *Canadian Journal of Microbiology*, Vol. 51, No. 7, 2005, pp. 541-547.

[4] G. C. Schito, "The Importance of the Development of Antibiotic Resistance in *Staphylococcus aureus*," *Clinical Microbiology Infection*, Vol. 12, Suppl. 1, 2006, pp. 3-8.

[5] S. Gibbons, "Phytochemicals for Bacterial Resistance. Strengths, Weaknesses and Opportunities," *Planta Medica*, Vol. 74, No. 6, 2008, pp. 594-602.

[6] G. D. Wright, "Resisting Resistance: New Chemical Strategies for Battling Superbugs," *Chemistry and Biology*, Vol. 7, No. 6, 2000, pp. R127-R132.

[7] X. Wu, H. Liu, J. Liu, K. N. Haley, J. A. Treadway, J. P. Larson, *et al*., "Immunofluorescent Labeling of Cancer Marker Her2 and Other Cellular Targets with Semiconductor Quantum Dots," *Nature Biotechnology*, Vol. 21, No. 1, 2003, pp. 41-46.

[8] J. D. Fortner, D. Y. Lyon, C. M. Sayes, A. M. Boyd, J. C. Falkner, E. M. Hotze, Alemany *et al*., "C-60 in Water: Nanocrystal Formation and Microbial Response," *Environmental Science and Technology*, Vol. 39, No. 11, 2005, pp. 4307-4316.

[9] P. Li, J. Li, Q. Wu and J. Li, "Synergistic Antibacterial Effects of Lactum Antibiotic Combined with Silver Nanoparticles," *Journal of Nanotechnology*, Vol. 16, No. 9, 2005, pp. 1912-1917.

[10] A. M. Smith, H. Duan, M. N. Rhyner, G. Ruan and S. A. Nie, "Synthesis of Gold Nanoparticles Bearing the Bioconjugation," *Phys Chem Chem Phys*, Vol. 8, 2006, p. 3895.

[11] G. J. Kearns, E. W. Foster and J. E. Hutchison, "Substrates for Direct Imaging of Chemically Functionalized $SiO_2$ Surfaces by Transmission Electron Microscopy," *Analytical Chemistry*, Vol. 78, 2006, p. 298.

[12] P. Mulvaney, "Surface Plasmon Spectroscopy of Nanosized Metal Particles Langmuir," Vol. 12, 1996, p. 788.

[13] T. Sungkaworn, W. Triampo, P. Nalakarn, D. Triampo, I. M. Tang, Y. Lenbury, *et al*., "The Effects of $TiO_2$ Nanoparticles on Tumor Cell Colonies: Fractal Dimension and Morphological Properties," *International Journal of Biomedical Science*, Vol. 2, No. 1, 2007, pp. 67-74.

[14] M. Cho, H. Chung, W. Choi, *et al*., "Different Inactivation Behaviors of MS-2 Phage and *Escherichia coli* in $TiO_2$ Photocatalytic Disinfection," *Applied and Environmental Microbiology*, Vol. 71, 2005, pp. 270-275.

[15] A. Fujishima, N. R. Tata and A. T. Donald, "Titanium Dioxide Photocatalysis," *Journal of Photochemistry and Photobiology C*: *Photochemistry Reviews*, Vol. 1, 2000, pp. 1-21.

[16] K. Shiraishi, H. Koscki, T. Tsurumoto, *et al*., "Antimicrobial Metal Implant with a $TiO_2$-Conferred Photocatalytic Bactericidal Effect against *Staphylococcus aureus*," *Surf. Inter. Anal*., Vol. 41, 2008, pp. 17-21.

[17] NCCLS, "Performance Standards for Antimicrobial Susceptibility Testing," 12*th Informational Supplement M*100-*S*12, *National Committee for Clinical Laboratory Standards*, Villanova, PA. 2002.

[18] B. Shopsin, M. Gomez, S. O. Montgomery, D. H. Smith, M. Waddington, D. E. Dodge, D. A. Bost, M. Riehman, S. Naidich and B. N. Krieswirth, "Evalution of Protein A Gene Polymorphic Region DNA Sequencing for Typing of *Staphylococcus aureus* Strains," *Journal of Clinical Microbiology*, Vol. 37, 1999, pp. 3556-3563.

[19] H. Zhang and G. Chen, "Potent Antibacterial Activities of Ag/$TiO_2$ Nanocomposite Powders Synthesized by a One-Pot Sol-Gel Method," *Environmental Science and Technology*, Vol. 43, No. 8, 2009, pp. 2905-2910.


 

*Journal of Biomaterials and Nanobiotechnology*, **2010, 1, 42-49**
doi:10.4236/jbnb.2010.11006 Published Online October 2010 (http://www.SciRP.org/journal/jbnb)

# Preparation and Characterization of Homogeneous Hydroxyapatite/Chitosan Composite Scaffolds via *In-Situ* Hydration

**Hong Li[1,2*], Chang-Ren Zhou[1,2], Min-Ying Zhu[1], Jin-Huan Tian[1,2], Jian-Hua Rong[1,2]**

[1]Department of Materials Science and Engineering, Jinan University, Guangzhou, China; [2]Education Ministry Research Centre of Artificial Organs & Materials, Jinan University, Guangzhou, China.
Email: [*]tlihong@jnu.edu.cn, hli2@clemson.edu

Received May 14th, 2010; revised June 5th, 2010; accepted June 30th, 2010.

## ABSTRACT

*Hydroxyapatite*(*HAP*)*/Chitosan*(*CS*) *composite is a biocompatible and bioactive material for tissue engineering. A novel homogeneous HAP/CS composite scaffold was developed via lyophilization and in situ hydration. A model CS solution with a Ca/P atom ratio of* 1.67 *was prepared through titration and stirring so as to attain a homogeneous dispersion of HAP particles. After lyophilization and in situ hydration, rod-shaped HAP particles* (5 *μm in diameter*) *within the CS matrix homogeneously scattered at the pore wall of the CS scaffold. X-ray diffraction* (*XRD*) *and Fourier-Transformed Infrared spectroscopy* (*FTIR*) *confirmed the formation of HAP crystals. The compressive strength in the composite scaffold indicated a significant increment over a CS-only scaffold. Bioactivity in vitro was completed by immersing the scaffold in simulated body fluid* (*SBF*), *and the result suggested that there was an increase in apatite formation on the HAP/CS scaffolds. Biological in vivo cell culture with MC* 3*T*3-*E*1 *cells for up to* 7 *days demonstrated that a homogeneous incorporation of HAP particles into CS scaffold led to higher cell viability compared to that of the pure CS scaffold or the HAP/CS scaffold blended. The results suggest that the homogeneous composite scaffold with better strength, bioactivity and biocompatibility can be prepared via in vitro hydration, which may serve as a good scaffold for bone tissue engineering.*

***Keywords*: *Hydroxyapatite, Chitosan, Scaffold, Composite, Hydration***

## 1. Introduction

Tissue engineering, which applies methods from engineering and life sciences to create artificial constructs to direct tissue regeneration, has attracted many scientists and surgeons with a hope to treat patients in a minimally invasive and less painful way. The important process of a tissue engineering paradigm is to isolate specific cells to grow them on a scaffold. A scaffold should be in combination with support for tissue architecture, biomolecules and selective transportation of ions in body fluids. Chitosan (CS) is the partially deacetylated form of chitin that can be extracted from crustacean. Apart from being bioresorbable, it is biocompatible, non-harmful, non-toxic compounds and biofunctional. In addition, CS is easy to mould a 3-dimensional scaffold which can support tissue ingrowth, aid in the formation of tissue structure, and promote growth and mineral rich matrix deposition by osteoblast in culture for bone tissue engineering [1]. It is important to note that CS in combination with hydroxyapatite (HAP, $Ca_{10}(PO_4)_6(OH)_2$), further enhance tissue regenerative efficacy and osteoconductivity [2-4]. HAP can accelerate the formation of bone-like apatite on the surface of implant and can induce bone formation [5]. By the way, incorporation of HAP into a CS polymer matrix has also been shown a significant enhancement of mechanical strength [6].

Several studies have focused on the composite scaffold for bone tissue engineering [7-9], such as CS/calcium phosphate [7], CS/HAP bilayer scaffold [8]. The composite had been prepared by different processing, such as mechanical mixing of HAP powder in a solution [10,11], co-precipitation [12], and biomimetic process [13,14]. Generally, HAP powder was mixed with CS dissolved in 2% acetic acid solution, poured into a mould, and freezing-dried to make sponge composites. The final material was heterogeneous, which was shown in the macroscopically less homogeneous. However, to ensure a more

 

effective contact between scaffold and tissue, a homogeneous composite scaffold should be prepared. In addition, a uniform distribution of inorganic particles in polymer matrix theoretically and experimentally improves mechanical property [15,16].

The present work aims to design and develop a homogeneous composite scaffold fabricated from biopolymer CS and bioceramic HAP as a candidate for bone tissue engineering applications. It is hypothesized that a homogeneous HAP dispersion could lead to an enhancement on mechanically competent, bioactivity and biocompatibility. Generally, a homogeneous dispersion can be obtained if the materials mixed and formed in an aqueous environment. However, CS is acid-soluble while HAP usually forms in a solution with pH > 10. Therefore, in order to achieve a homogeneous HAP/CS composite scaffold, the combination of the lyophilization method and *in situ* hydration in alkine aqueous was applied in this work. The composition, morphology, mechanical property, bioacitivity and biocompatibility of the homogenous composite scaffold were studied.

## 2. Experimental Procedures

### 2.1. Preparation of the Composite Scaffold

CS powder was supplied commercially with the degree of deacetylation over 97% (Shanghai Boao Biotechnology Co., Shanghai, China; the viscosity-average relative molecular weight was $1.8 \times 10^6$ Da.). A CS aqueous solution of 2 wt% was prepared by dissolving CS powder into deionized water containing 2 wt% acetic acid. Then, under agitation, a stoichiometric 2 mol/L $CaCl_2$ solution was slowly added into the CS solution. Subsequently, a 1.2 mol/L $K_2HPO_4$ solution, with a Ca/P atom ratio of 1.67, was added dropwise. The ratio of HAP to CS solution was 60/100 by weight. After stirring, the suspension was put into dishes (diameter of 30 mm, and depth of 5 mm) and 24-well plates (diameter of 14 mm, and depth of 14 mm), and then rapidly transferred into a freezer at presented temperature –40°C to solidify the water and induced phase separation. The solidifying route maintained at that temperature over night. In the next stage, frozen samples were lyophilized using a freeze-dryer (Uniequip, Germany) for 24 hrs. The obtained scaffolds were hydrated with a mixture of 0.1 N sodium hydroxide solution and pure ethanol with a 2:1 volumetric ratio for different time periods. After *in situ* hydration, the samples washed with deionized water till the pH of washout water was about 7. Finally, the samples treated were freeze-dried again to obtain the CS/HAP porous scaffolds. The samples were denoted by D.

As a control, HAP/CS composite scaffold was prepared via blending method. Briefly, HAP powder (Boao Bio. Tech. Com., Shanghai, China) was added into a CS aqueous solution of 2 wt% acetic acid (HAP/CS solution is 60/100, wt/wt) with magnetic stirring and ultrasonic treatment. After stirring, the mixture was moulded, frozen and lyophilized as described above. The samples were denoted by E, while the pure CS scaffold was denoted by A.

### 2.2. SEM Examination

The lyophilized scaffolds were cut with a razor blade to expose the inner surfaces. After being coated with gold in a sputtering device, the samples were examined with a scanning electron microscope (XL-30 ESEM, Philips Co., Netherland) with an accelerating voltage of 20 kV.

### 2.3. XRD

The composite scaffold samples were ground to fine powder after frozen in liquid $N_2$ for 30 minutes, and then characterized by X-rays diffraction (XRD; MASL, Beijing, China, 40 kV, 20 mA, 3°/min) .

### 2.4. FTIR

The HAP/CS scaffolds prepared via lyophilization and *in situ* hydration were analyzed by Fourier-transform infrared attenuated total reflective spectroscopy (FT-IR; EQUINOX 55, Bruker, Germany). The scaffolds were frozen in liquid $N_2$ for 30 minutes and were ground into a fine powder. The powder samples were mixed with KBr powder and compressed into pellets for FT-IR examination. The spectra were collected over the range of 4000-400 $cm^{-1}$.

### 2.5. Compressive Strength Measurement

The samples of each of the three type scaffolds (A, CS-only; D, HAP/CS composite *in situ* hydrated; E: HAP/CS composite blended) were cut into rectangle (5.0 mm × 5.0 mm × 5.0 mm). The compressive strength was measured using a computer-controlled Universal Testing Machine (AG-1, Shimadzu Co., Tokyo, Japan) with a guideline set in ASTM D5024-95a. The strength was calculated by using the yield point load divided by the specimen's cross sectional area. Five parallel samples were evaluated for each of the scaffolds.

### 2.6. Incubation in Simulated Body Fluid (SBF)

To evaluate the bioactivity of the composite scaffolds *in vitro*, the samples were incubated in SBF (the prescription of SBF referring to Ref. [17]). The 1 g samples were placed into SBF (50 ml) and incubated at 37°C. The concentrations of Ca and P ions in SBF were measured at 1, 3 and 7 days incubation by inductively coupled plasma atomic emission spectrometry (Optima 2000 DV, Perkin

 

Elmer Co., USA). Morphologies of the incubated scaffolds were observed by SEM as described before.

### 2.7. Cell Culture

Osteoblast Cells line MC 3T3-E1 (a clonal preosteoblastic cell line derived from newborn mouse calvaria, which is often used in bone tissue engineering research) were cultured in DMEM supplemented with 10% fetal bovine serum (GIBCO Co., U.S.A.), 100 U/mL penicillin (Sigma, St. Louis, MO), and 100 μg/mL streptomycin (Sigma). Cells were incubated at 37°C in a 5% $CO_2$ incubator, and the medium was changed every 2 days. When the cells reached the stage of confluence, they were harvested by trypsinization followed by the addition of fresh culture medium to create a cell suspension. A cell suspension with a concentration of $2 \times 10^6$ cells/mL was loaded into the 3-D porous scaffolds (14 mm in diameter and 2 mm in thickness), with 200 μL of suspension for each scaffold. The scaffolds were put in a polystyrene 24-well flat-bottom culture plate and incubated at 37°C in a 5% $CO_2$ incubator. After cells attached at about 6 hrs, fresh culture medium was added until the total medium volume was 500 μL. Culture medium was changed every 2 days.

### 2.8. Cell viability Assessment

A MTT assay was applied in this study to quantitatively assess the number of viable cells attached and grown on the tested scaffolds. Briefly, all the tested scaffolds with cultured cells at pretermined time points were fetched to a new 24-well flat-bottom culture plate. One mL of serum-free medium and 100 μL of MTT (Sigma) solution (5 mg/mL in PBS) were added to each sample, followed by incubation at 37°C for 4 h for MTT formazan formation. The upper solvent was removed and 1 mL of 10% sodium dodecyl sulfate (Sigma) in 0.01*N* HCl was added to dissolve the formazan crystals for 6 h at 37°C. During the dissolving period, the spongy scaffolds were squeezed every 30 min to ensure the complete extraction of the formazan crystals. The optical density (OD) at 490 nm was determined against the sodium dodecyl sulfate solution blank. Five parallel replicates were analyzed for each sample.

## 3. Results and Discussion

### 3.1. Phase Analysis

The XRD patterns of the D sample before and after hydration for different hydration periods are summarized in **Figure 1**. The XRD patterns were verified by the Power Diffraction File (HAP: Card No. 090432; CS: Card No. 391894; DCPD: No. 720713; KCl: No. 730713). It indicated that, the DCPD and KCl crystalline phases mainly occurred in the scaffolds D before hydration. The longer the hydration ripening time, the smoother the peaks belong to DCPD and KCl. After 24 h of ripening, DCPD and KCl crystalline phases disappeared in the composite scaffold D. The broad peak that appeared around 20° was assigned to CS (20.305°, 21.290°), and the sharp diffraction characteristic peaks that appeared at around 31.8° and 25.9° correspond to the peaks of HAP (31.773°, 25.879°).

For pH of HAP formation more than 10, it was observed that DCPD (brushite), and (or) amorphous CaP occurred when $Ca^{2+}$ and $HPO_4^{2-}$ were directly dropped into a CS solution with pH < 7 (**Figure 1 b**). During the process of *in situ* hydration in the mixture solution of sodium hydroxide solution and pure ethanol, the unstable brushite, as well as the other amorphous CaP phases transformed into a more stable HAP phase, according to the following Equations (1) and (2) [18].

$$10CaHPO_4+12OH^- \rightarrow Ca_{10}(PO_4)_6OH_2+10H_2O+4PO_3^{4-} \quad (1)$$

$$PO_3^{4+}+ACP+OH^- \rightarrow Ca_{10}(PO_4)_6OH_2 \quad (2)$$

As Pang's report [19] and our study, after 24 h of ripening, the transformation of brushite and amorphous CaP to HAP was found nearly completely.

XRD patterns show the presence of KCl in the CS composite before hydration due to the precipitation of KCl during the lyophilization. After the composites were hydrated and washed, KCl solved and disappeared as indicated in **Figure 1**.

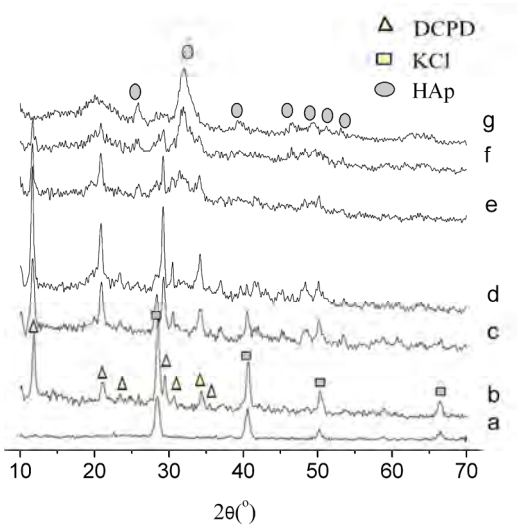


**Figure 1. XRD patterns of (a) KCl, HAP/CS composite scaffold D before hydration (b), after 1 hr (c), after 3 hrs (d), after 6 hrs (e), 12 hrs (f) and 24 hrs (g) hydration.**

 

### 3.2. FTIR

An infrared absorption spectra of the scaffold is summarized in **Figure 2**. The absorption bands at 3540 $cm^{-1}$, 3487 $cm^{-1}$ and 633 $cm^{-1}$ respectively correspond to the stretching and vibration of the lattice $OH^-$ ions, while the bands of absorbed water are shown at 3287 $cm^{-1}$, 3163 $cm^{-1}$, 1648 $cm^{-1}$. The characteristic bands for $HPO_4^{2-}$ were assigned at 1133 $cm^{-1}$, 1064 $cm^{-1}$, 989 $cm^{-1}$, 875 $cm^{-1}$, 577 $cm^{-1}$, 527 $cm^{-1}$ [20]. The magnitude of these bands became weaker with the development of *in situ* hydration and finally disappeared. The characteristic bands for $PO_4^{3-}$ appeared at 963 $cm^{-1}$ for the ν1 mode [21-22]. The signal became clearly as the hydration processing. The observation of the ν3 symmetric P-O stretching vibration at 1032/1042 $cm^{-1}$ as a distinguishable peak, together with the bands 566/602 $cm^{-1}$ corresponding to ν4 bending vibration indicates the presence of HAP in the samples as summarized in **Figure 2(c, d, e, f, g, h)**. Theses peaks show obviously stronger after 24 hours ripening, in accord with the XRD results.

### 3.3. Morphology Analysis

The morphologies of the scaffolds were examined with SEM. The CS-only scaffold A, composite scaffold D after hydration showed a similar spongy appearance (**Figure 3**) in macroscopic morphology, which indicated that both adding the HAP in the system and hydrating the scaffolds did not influence the porous structure. Due to the artifact of the sample preparation for SEM, the pores in the A scaffold were collapsed as illustrated in **Figure 3(a)**. The D scaffolds depict more regular porous structure (**Figure 3(e)**), for its relative high strength can resist the distortion during the sample preparation. However, the microscopic morphology on pore-wall surfaces was quite different. The surface of the scaffold A is smooth as shown in **Figure 3(b)**. Before hydration processing was applied, the walls of D are embedded with flower-shaped large particles, as indicated in **Figures 3(c)** and **(d)**. After hydration, the rod like HAP particles with about 5 μm in diameter were homogeneously scattered in the pore-wall surfaces of the composite scaffold D as shown in **Figure 3(f)**. The SEM results suggest that HAP particles can be homogeneously incorporated with CS matrix via lyophilization and *in situ* hydration process.

### 3.4. Mechanical Property

The compressive strength of A, D and E are illustrated in the **Figure 4**. Sample D has the highest compressive strength when compared to the control. Li reported that the incorporation HAP into CS matrix via blending method would result in the decrease of mechanical properties of HAP/CS material due to the weaker interfacial bonding between HAP filler and CS matrix [23]. However, in our study, no obvious decrease appeared in aspect of mechanical property blended HAP/CS sponge E.

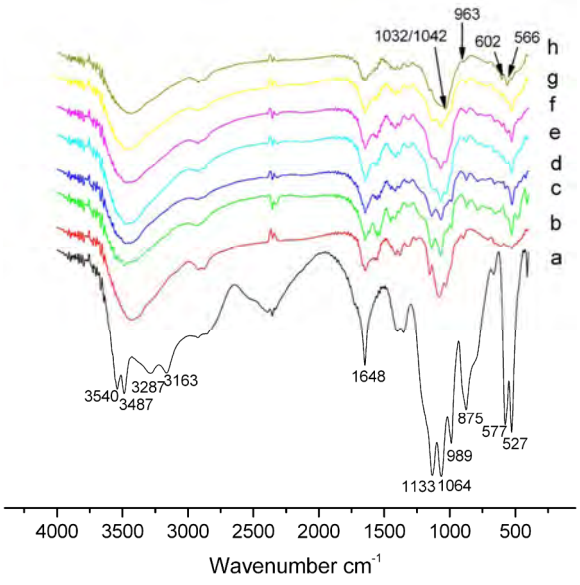


**Figure 2. IR spectra of DCPD (a), CS (b), composite scaffold D before hydration (c), after 1 hr (d), after 3 hrs (e), after 6 hrs (f), 12 hrs (g) and 24 hrs (h) hydration.**

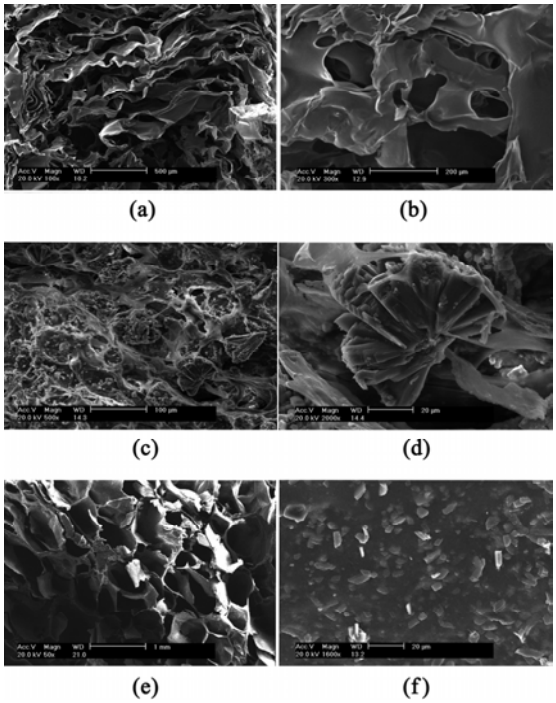


**Figure 3. SEM morphologies of CS-only scaffold (a), the pore wall of the CS-only scaffold (b), composite scaffold D before hydration(c)(d) and after hydration (e)(f).**

 

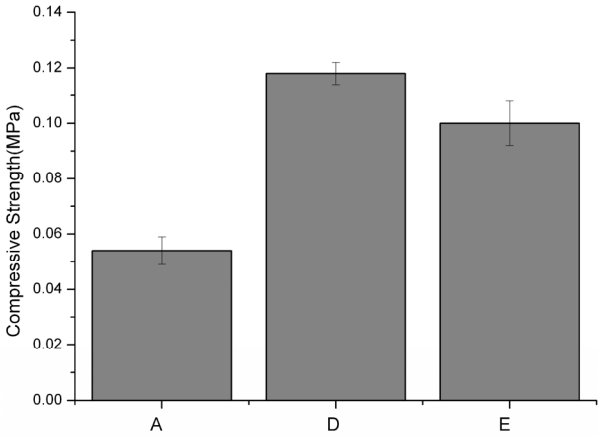


**Figure 4. Compressive strength of the scaffolds A, D after 24 hrs hydration and composite via blending E. Data represented the mean ± SD for five samples. $p < 0.01$ compared with pure CS.**

The composite scaffold D prepared by *in situ* hydration, with HAP particles homogeneously dispersion, has a little increment in compressive strength and less derivation, as compared to the control E. The compressive strength indicated that the observed homogeneous particle dispersion would be helpful to enhance the scaffold mechanically competent.

### 3.5. Bioactivity

According to Kokubo et al., the in vitro immersion of bioactive materials in SBF was thought to reproduce *in vivo* surface structures [13,24,25]. The grown layer is sometimes called a bone-like apatite [25]. A bone-like apatite layer plays an important role in establishing the bone-bonding interface between biomaterials and living tissue [4]. As shown in **Figure 5**, the surface of the soaked scaffolds in SBF showed spherical particles containing tiny crystals which correspond to apatite [26-28]. The size and number of the apatite particles formed on the D scaffold was obviously larger than those of the particles on the scaffolds A and E. The apatite crystals on the sample D also depict a relatively uniformly size according **Figure 5**, unlike those on the sample E that larger particles occurred. With the immersion periods going, the quantities of apatite particles increased in macroscopic morphology, but the difference still existed. The scaffolds A and E were covered with tiny apatite crystals while some larger particles dotted on the E scaffold, but a layer of particle crystals fully covered the wall of the D scaffold. This result is also supported by the results of the Ca and P concentration decrease in SBF.

**Figure 6** displays the concentrates of Ca and P ions in SBF, which soaked the samples. An abrupt decrease in the concentrates of Ca and P ions during the first three days followed by a continuous slow decrease in the next days. The result is in agreement with the SEM observation for changes in macroscopic morphologies after the first three days. This appreciable decrease in Ca and P concentrations can be attributed to the formation of apatite crystals on the specimen surfaces. However, the decreases of Ca and P concentrations in the SBF, which the composite scaffolds D and E were soaked, were larger than that of scaffold A. It is just confirmed that the amount of apatite formed on the scaffold A was less than that of apatite on the composite scaffolds D and E as shown in **Figure 5**. The large apatite crystals dotted on the scaffold E also led to the decrease in the concentrations of Ca and P ions more rapidly than that of scaffold D in the first three day.

According to **Figure 6**, as a result of the difference of crystallinity of HAP, a little increase of Ca and P concentrates at the first day in **Figure 6** D sample is shown. The HAP particles synthesized at low temperatures have been shown to have low crystallinity and high solubility [29]. Therefore, the poorly crystallized HAP in the D scaffolds formed via *in situ* hydration within the solution has high solubility, which led to ions release in the SBF media at early time. There was an increment in the concentration of both Ca and P ions after 12 hrs immersion of the scaffold D in SBF. In the scaffold A, the increment of Ca and P concentrates might be the de-chelate release of CS-Ca chelate at neural environment.

Despite the difference of HAP particles, the scaffolds with HAP (D and E) still show better bioactivity as compared to the CS scaffold A when the scaffolds were soaked in SBF. HAP would be favor to the nucleation of bone-like apatite for HAP particles could act as nuclea tion sites in a metastable calcium phosphate solution

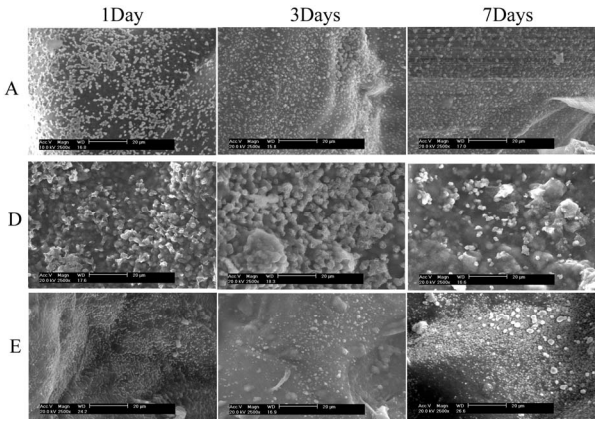


**Figure 5. SEM morphologies of the pore walls of the samples A, composite D after 24 hrs hydration and composite via blending E in SBF after 1, 3 and 7 days immersion.**

 

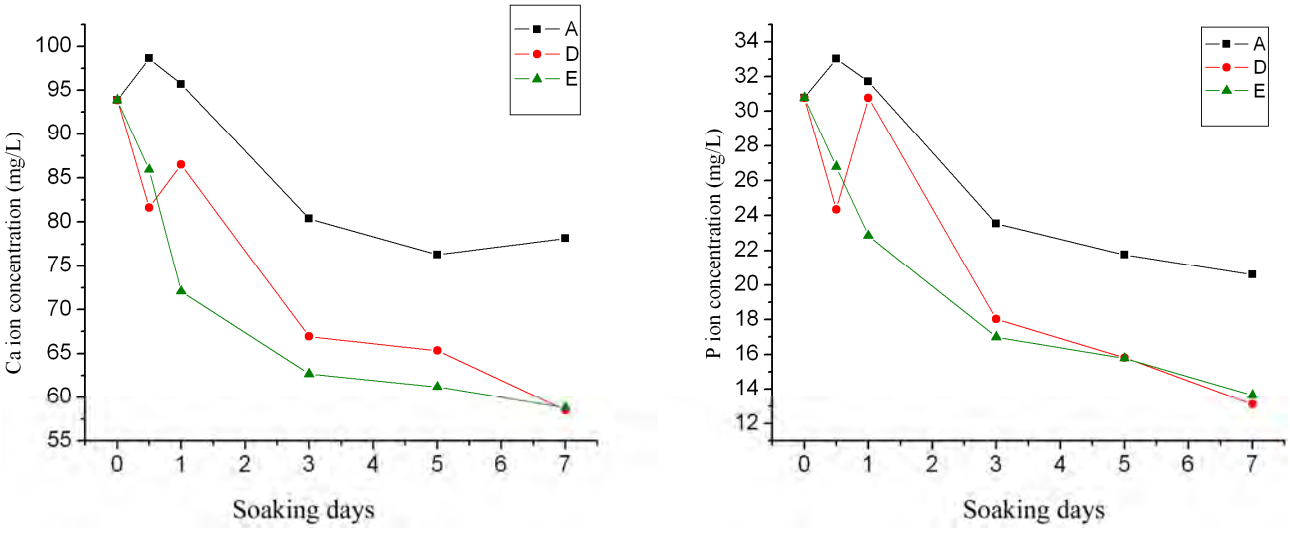


**Figure 6. Concentrations of Ca ions (a) and P ions (b) in SBF in which the samples were immersed (A. CS-only; D. composite D after 24 hrs hydration; E. composite via blending).**

such as SBF [30]. However, a homogeneous dispersion of HAP in composite can obviously induced a homogeneous precipitation of bone-like apatite in SBF, and would be improve the bioactivity more effectively.

### 3.6. Cell Test

The biocompatibility of the scaffolds A, D and E was assessed on cells' proliferation. Cell proliferation was examined with MTT assay (**Figure 7**). The same amount of MC 3T3-E1 cells were seeded on the scaffolds A, D and E. MC 3T3-E1 is a preosteoblast cell line derived from newborn mouse calvaria, which usually is used to evaluate the biocompatibility of the materials for bone tissue engineering. At early 3 day time, a MTT value of sample A has the highest one. After 7 days' culture, the value of the D scaffold was the higher than the others scaffolds, which indicated that the MC 3T3-E1 cells showed much better viability property on D. It is an indication of both the process and the component of HAP might have significant difference in some degree on the biocompatibility of these scaffold materials.

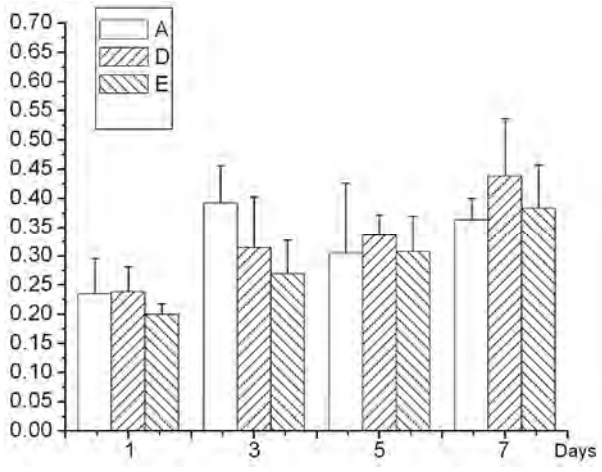


**Figure 7. MTT assay of cells grown on CS scaffold and composite porous scaffolds. Data represent the mean ± SD for three samples. $p < 0.01$ compared with pure CS. (A: CS-only; D: composite D after 24 hrs hydration; E: composite via blending).**

## 4. Conclusions

In this paper, a homogeneous HAP/CS composite scaffold was prepared and investigated. HAP particles were combined homogeneously with CS matrix through lyophilization and *in situ* hydration in alkaline solution. As compared to the controls, the composite scaffold indicated an increment in mechanical strength, altogether with a homogeneous bone-like apatite precipitation in SBF. The difference processing for fabricating the CS/HAP composite scaffold also showed significant difference in cell's biocompatibility according to this study. The results on the homogeneous composite indicate that this novel process is a new approach to fabricating bone tissue engineering scaffolds especially for composite scaffold. Further reports about *in vivo* study will be reported in the near future.

## 5. Acknowledgement

The authors wish to thank the National High Technology Development Program of China (2007AA091603) and the National Science Foundation of China (30870612,

 

20604010) for supporting this research.

## REFERENCES

[1] Y. J. Seol, J. Y. Lee, Y. J. Park, Y. M. Lee, Y. Ku, I. C. Rhyu, S. J. Lee, S. B. Han and C. P. Chung, "Chitosan Sponges as Tissue Engineering Scaffolds for Bone Formation," *Biotechno Lett*, Vol. 26, 2004, pp. 1037-1041.

[2] F. Zhao, W. L. Grayson, T. Ma, B. Bunnell and W. W. Lu "Effects of Hydroxyapatite in 3-D Chitosan–Gelatin Polymer Network On Human Mesenchymal Stem Cell Construct Development," *Biomaterials*, Vol. 27, 2006, pp. 1859-1867.

[3] T. Kawakami, M. Antoh, H. Hasegawa, T. Yamagish, M. Ito and S. Eda, "Experimental Study on Osteoconductive Properties of a Chitosan-Bonded Hydroxyapatite Self-Hardening Paste," *Biomaterials*, Vol. 13, 1992, pp. 759-763.

[4] Z. Ge, S. Baguenard, L. Y. Lim, A. Wee and E. Khor "Hydroxyapatite-Chitin Materials as Potential Tissue Engineered Bone Substitutes," *Biomaterials*, Vol. 25, 2004, pp. 1049-1058.

[5] L. J. Kong, Y. Gao, G. Y. Lu, Y. D. Gong, N. M. Zhao and X. F. A. Zhang, "Study on the Bioactivity of Chitosan/Nano- Hydroxyapatite Composite Scaffolds for Bone Tissue Engineering," *European Polymer Journal*, Vol. 42, 2006, pp. 3171-3179.

[6] Q, Hu, B, Li, M, Wang, J, Shen, "Preparation and Characterization of Biodegradable Chitosan/ Hydroxyapatite Nanocomposite Rods Via in Situ Hybridization: A Potential Material as Internal Fixation of Bone Fracture," *Biomaterials*, Vol. 25, 2004, pp. 779-785.

[7] Y. Zhang, M. Zhang, "Synthesis and Characterization Ofmacroporous Chitosan/Calcium Phosphate Composite Scaffolds for Tissue Engineering," *The Journal of Biomedical Materials Research*, Vol. 55, 2001, pp. 304-312.

[8] J. M. Oliveira, M. T. Rodrigues, S. S. Silva, P. B. Malafaya, M. E. Gomes, C. A. Viegas, I. R. Dias, J. T. Azevedo, J. F. Mano and R. L. Reis, "Novel Hydroxyapatite/Chitosan Bilayered Scaffold for Osteochondral Tissue-Engineering Applications: Scaffold Design and its Performance When Seeded with Goat Bone Marrow Stromal Cells," *Biomaterials*, Vol. 27, 2006, pp. 6123-6137.

[9] S. Viala, M. Freche and J. L. Lacout, "Preparation of a New Organic Mineral-Composite: Chitosan-Hydroxyapatite," Ann Chin Sci Mater, Vol. 23, 1998, pp. 69-72.

[10] F. Zhao, Y. Yin, W. W. Lu, J. C. Leong, W. Zhang, J. Zhang, M. Zhang and K. Yao, "Preparation and Histological Evaluation of Biomimetic Three-Dimensional Hydroxyapatite/Chitosan-Gelatin Network Composite Scaffolds," *Biomaterials*, Vol. 23, 2002, pp. 3227-3234.

[11] M. V. Correlo, F. B. Luciano, B. Mrinal, F. M. Joao, M. N. Nuno and L. R. Ruis, "Hydroxyapatite Reinforced Chitosan and Polyester Blends for Biomedical Applications," *Macromolecular Materials and Engineering*, Vol. 290, 2005, pp. 1157-1165.

[12] X. Shen, H. Tong, T. Jiang, Z. Zhu, P. Wan and J. Hu, "Homogeneous Chitosan/Carbonate Apatite/Citric Acid Nano- Composites Prepared Through a Novel in Situ Precipitation Method," *Journal of Computer Science and Technology*, Vol. 67, No. 11-12, 2007, pp. 2238-2245.

[13] T. Kokubo, M. Hanakawab, M. Kawashita, Minoda, T. Beppu, T. Miyamoto and T. Nakamur, "Apatite Formation on Non-Woven Fabric of Carboxymethylated Chitin in SBF," *Biomaterials*, Vol. 25, No. 18, 2004, pp. 4485- 4488.

[14] K. Tuzlakoglu and R. L. Reis, "Formation of Bone-Like Apatite Layer on Chitosan Fiber Mesh Scaffolds by a Biomimetic Spraying Process," *Journal of Materials Science: Materials in Medicine*, Vol. 18, 2007, pp. 1279-1286.

[15] Z. H. Guo, S. Y. Wei, B. Shedd, R. Scaffaro, T. Pereira and H. T. Hahn, "Particle Surface Engineering Effect on the Mechanical, Optical and Photoluminescent Properties of Zno/Vinyl-Ester Resin Nanocomposites," *Journal of Materials Chemical*, Vol. 17, 2007, pp. 806-813.

[16] M. C. Kuo, C. Tsai, J. C. Huang, M. Chen, "PEEK composites reinforced by nano-sized $SiO_2$ and $Al_2O_3$ particulates," *Materials Chemistry and Physics*, Vol. 90, 2005, pp. 185-195.

[17] T. Kokubo, H. Kushitani, C. Ohtsuki, S. Sakka and T. Yamamuro, "Chemical Reaction of Bioactive Glass and Glass– Ceramics with a Simulated Body Fluid," *Journal of Materials Science: Materials in Medicine*, Vol. 1, 1992, pp. 79-83.

[18] V. M. Rusua, C. H. Ng, M. Wilke, B. Tierscha, P. Fratzld and M. G. Peter, "Size-Controlled Hydroxyapatite Nanoparticles as Self-Organized Organic–Inorganic Composite Materials," *Biomaterials*, Vol. 26, 2005, pp. 5414-5426.

[19] Y. X. Pang and X. Bao, "Influence of Temperature, Ripening Time and Calcination on the Morphology and Crystallinity of Hydroxyapatite Nanoparticles," *Jorunal of European Ceramic Society*, Vol. 23, 2003, pp. 1697-1704.

[20] T. K. Anee, M. Palanichamy and M. Ashok, "Influence of Iron and Temperature on the Crystallization of Calcium Phosphates at the Physiological pH," *Materials Letters*, Vol. 58, 2004, pp. 478-482.

[21] C. W. Chen, R. E. Riman, K. S. Tenhuisen and K. Brown, "Mechanochemical–Hydrothermal Synthesis of Hydroxyapatite from Nonionic Surfactant Emulsion Precursors," *Journal of Cryst Growth*, Vol. 270, 2004, pp. 615-623.

[22] G. C. Koumoulidis, A. P. Katsoulidis, A. K. Ladavos, P. J. Pomonis, C. C. Trapalis, A. T. Sdoukos and T. C. Vaimakis, "Preparation of Hydroxyapatite via Microemulsion Route," *Jouranl of Colloid and Interface Science*, Vol. 259, 2003, pp. 254-260.

[23] B. Q. Li, Q. L. Hu, X. Z. Qian, Z. P. Fang and J. C. Shen,

 

"Bioabsorbable Chitosan/Hydroxyapatite Composite Rod for Internal Fixation of Bone Fracture Prepared by in Situ Precipitation," *Acta Polymerica Sinica*, Vol. 6, 2002, pp. 828-833.

[24] T. Kokubo, I. Ito and T. Huang, "P–Rich Layer Formed on High–Strength Bioactive Glass–Ceramics A–W," *Journal of Biomedical Materials Research*, Vol. 24, 1990, pp. 331- 343.

[25] P. Li, C. Ohtsukl and T. Kokubo, "Effects of Ions in Aqueous Media on Hydroxyapatite Induction by Silica Gel and Its Relevance to Bioactivity of Bioactive Glasses and Glass/ Ceramics," *Journal of Applied Biomaterials*, Vol. 4, 1993, pp. 221-229.

[26] A. S. Posner, "The Mineral of Bone," *Clinical Orthopaedics Related Research*, Vol. 200, 1985, pp. 87-93.

[27] T. Kokubo, "Apatite Formation on Surfaces of Ceramics, Metals and Polymers in Body Environment," *Acta Materialia*, Vol. 7, 1998, pp. 2519-2527.

[28] X. Lu and Y. Leng, "Thyeoretical Analysis of Calcium Phosphate Precipitation in Simulated Body Fluid," *Biomaterials*, Vol. 26, No. 10, 2005, 1097-1108.

[29] T. Matsumoto, M. Okazaki, M. Inoue, S. Yamaguchi, T. Kusunose, T. Toyonaga, Y. Hamada and J. Takahashi, "Hydroxyapatite Particles as a Controlled Release Carrier of Protein," *Biomaterials*, Vol. 24, 2004, pp. 3807-3812.

[30] T. Kokubo, "Apatite Formation on Surfaces of Ceramics, Metals and Polymers in Body Environment," *Acta Materialia*, Vol. 46, 1998, pp. 2519-2527.

 

*Journal of Biomaterials and Nanobiotechnology*, **2010, 1, 50-60**
doi:10.4236/jbnb.2010.11007 Published Online October 2010 (http://www.SciRP.org/journal/jbnb)

# Synthesis and Characterization of Novel Hybrid Poly(methyl methacrylate)/Iron Nanowires for Potential Hyperthemia Therapy

**Huey-Wen Liou[1], Hong-Ming Lin[1*], Yeu-Kuang Hwu[2], Wen-Chang Chen[3], Wei-Jen Liou[1], Li-Chung Lai[4], Wei-Syuan Lin[1], Wen-An Chiou[4]**

[1]Department of Materials Engineering, Tatung University, DeHui St., Taipei, Taiwan; [2]Institute of Physics, Academia Sinica, Academia Rd., Nankang, Taipei, Taiwan; [3]Department of Chemical and Materials Engineering, National Yunlin University of Science and Technology, University Road, Section, Douliou, Yunlin, Taiwan; [4]NISP Lab, Jeong H. Kim Engineering Building, NanoCenter, University of Maryland, College Park, U.S.A.
Email: *hmlin@ttu.edu.tw

Received July 22nd, 2010; revised August 14th, 2010; accepted September 30th, 2010.

## ABSTRACT

*Externally applied magnetic fields have been used in this study to fabricate bamboo-like iron nanowires with or without a layer of Poly(methyl methacrylate) (PMMA). The hybrid PMMA/Fe nanowires were synthesized via hard X-ray synchrotron radiation polymerization with various treatment parameters. The results of XRD show that an oxide layer formed on the surface of the iron nanowires. The $Fe_2O_3$ and $Fe_3O_4$ phases coexist in the iron nanowires without X-ray irradiation. After X-ray irradiation, the $Fe_2O_3$ phase transformed into $Fe_3O_4$, which stabilized the iron nanowires. The results of XAS proved this phase transformation. TGA analysis confirmed the thermal properties and solid contents in these specimens. Their ferromagnetic behaviors were examined by magnetic hysteresis measurement, which indicated that the magnetic and structural properties of the nanowires can be manipulated by irradiation treatment. This may lead to a novel synthesis for iron nanowires that can be used in high thermal efficiency hyperthermia therapy.*

***Keywords*: *Iron Nanowires, Poly(methyl methacrylate), Hybrid, X-Ray Irradiation, XAS, Magnetic Materials***

## 1. Introduction

Recently, several research groups have carried out investigations of the magnetic properties of metal wires. They used different methods to prepare nanowires and microwires. Menon *et al.* [1], Bandyopadhyay *et al.* [2] and Zheng *et al.* [3] fabricated Fe, Co and Ni nanowires, respectively, using electrodeposition into nanoporous anodic alumina templates. Pan *et al.* synthesized NiCo microwires using a hydrothermal method [4]. A template-free method that combines chemical reduction and a magnetic field is applied to prepare Ni nanowires [5]. The latter method only needs one step in its preparation and no thermal treatment.

Herein, iron nanowires have been prepared by an externally applied magnetic field. Hybrid Poly(methyl methacrylate) (PMMA)/iron nanowires are synthesized by combining iron nanowires with radiation polymerization of PMMA. Hard X-ray synchrotron radiation can be used to initiate polymerization of PMMA and successfully produces PMMA beads [6]. This method has two essential characteristics. First, it requires only one step for the preparation of Fe nanowires with a polymerized PMMA coating by hard X-ray synchrotron radiation. Second, the PMMA/iron nanowires can be successfully synthesized without adding emulsifier. Compared with the usual chemical methods of preparing organic/inorganic hybrid materials, the method presented here is a quick, simple and 'green' process, which may reduce environmental pollution and increase broad, practical applications. Hybrid PMMA/Fe nanowires are intentionally designed to manipulate their magnetic properties for application in magnetic hyperthermia. The needle-sharp nanowires enhance friction heating while an alternative magnetic field is applied that increases the heating efficiency in hyperthermia therapy.

In this study, hybrid PMMA/Fe nanowires are investigated by X-ray diffraction (XRD), scanning electron microscopy (SEM), high resolution transmission electron microscopy (HRTEM), X-ray absorption spectroscopy

 

(XAS), thermogravimetry (TGA), and vibrating sample magnetometry (VSM). An XAS spectrum, which is basically the measured X-ray absorption coefficient as a function of the incoming photon energy, is generally divided by the role of multiple scattering photoelectrons into two different regions: X-ray Absorption Near-Edge Structure (XANES) and Extended X-ray Absorption Fine Structure (EXAFS). XANES, also referred as NEXAS (Near Edge X-ray Absorption Fine Structure), can be used to investigate the electronic structure of specific elements, and EXAFS is used mainly to investigate the local atomic structure concerning the type and number of elements as well as the nearest neighbor bond length [7]. In this study, the oxidation states of iron will be examined by XAS to reveal the effects of X-ray irradiation on the formation of iron oxides in iron nanowires.

## 2. Experimental

Methyl methacrylate monomer (MMA, Fluka Chemical Reagent Co.) was purified by reduced pressure distillation to remove the inhibitor before polymerization. Ferric chloride hexahydrate ($FeCl_3 \cdot 6H_2O$) and sodium borohydride ($NaBH_4$) were obtained from Sigma-Aldrich, Inc. Polyvinylpyrrolidone (PVP, K-30, average molecular weight: ca. 40,000 g/mol) was obtained from Tokyo Kasei Kogyo Chemical Reagent Co. Nitric acid (reagent ACS 99.5%), methanol and ethyl alcohol were bought from Wako Pure Chemical Industries. All solutions were prepared with deionized water (> 18 MΩ).

### 2.1. Preparation of Iron Wires and PMMA/Iron Nanowires

Five specimens of iron nanowires and PMMA/Fe nanowires with various parameters were prepared in this study. The first specimen was fabricated using the standard synthesis procedure for magnetic wires. Iron nanowires, denoted as specimen (I), were prepared using an externally applied magnetic field with an intensity of 0.3 T. Normally, Fe nanowires are produced in a 0.7 M aqueous solution of $FeCl_3 \cdot 6H_2O$ at room temperature in a high purity nitrogen atmosphere with an externally applied magnetic field after adding 0.8 M $NaBH_4$ aqueous solution. After synthesis, this notated specimen I is washed with anhydrous ethanol and dried in air. The chemical reaction mechanism (Equation 1) is shown as follows:

$$2FeCl_3 + 6NaBH_4 + 18H_2O \rightarrow 2Fe + 6B(OH)_3 + 6NaCl + 21H_2 \quad (1)$$

The second specimen is the same as specimen I after it undergoes hard X-ray synchrotron radiation for 10 min and is notated as specimen (II). The irradiation is carried out at the National Synchrotron Radiation Research Center (NSRRC) in Taiwan, with the hard X-ray beam line (BL01A). This NSRRC synchrotron light provides a 300 mA, 1.5 GeV electron beam to generate a photon source for scientific research. The hard X-ray beam line is a semi-white-light beam line. The photon flux is $1 \times 10^{12}$ photons/sec, and the radiation is incident onto the sample with a beam footprint of $18.6 \times 9.3$ mm$^2$. The distribution range of photon energy is between 10 and 15 keV, and the dose rate is 5.1 ± 0.9 kGy/s. After exposure, the specimen was washed with anhydrous ethanol and then dried.

For the third specimen, a 0.7 M solution of iron ion was prepared by dissolving $FeCl_3 \cdot 6H_2O$ in methanol and then mixing it with PVP and MMA monomer in a high purity nitrogen atmosphere. Then, a 0.8 M $NaBH_4$ aqueous solution was dropped into the previously prepared solution to synthesize iron nanowires in an externally applied magnetic field. After forming the iron nanowires, the sample was exposed to hard X-ray synchrotron radiation for 10 min. The obtained PMMA/Fe nanowires are denoted as specimen (III).

For the fourth specimen, a 0.7 M $FeCl_3 \cdot 6H_2O$ methanol solution was mixed with PVP and MMA monomers in a high purity nitrogen atmosphere and then exposed to hard X-rays for 10 min to polymerize before a 0.8M $NaBH_4$ aqueous solution was added under an externally applied magnetic field. The obtained sample underwent polymerization once again by hard X-ray exposure for another 10 min.

For the fifth specimen, PMMA polymer was synthesized before iron nanowires formation. MMA stock solution was prepared by dissolving PVP (5 vol.%) in methanol (35 vol.%) with de-ionized water (45 vol.%) and mixing it with MMA monomer (15 vol.%). The stock solution was stirred in high purity nitrogen gas to eliminate oxygen. In addition, the stock solution of iron precursor was prepared in deionized water with concentrations of 0.7 M $FeCl_3 \cdot 6H_2O$. Ten milliliter quantities of MMA stock solution were prepared in sealed bottles, ready for irradiation-induced polymerization for 10 min. After that, we prepared the volume ratios of iron stock solution to PMMA emulsion solution at 1:1. Next, 0.8 M $NaBH_4$ was added to the mixture solution for self-assembled hybrid PMMA/Fe nanowires under high-purity nitrogen gas atmosphere and a magnetic field. These are called specimen (V). The obtained sample was separated from the solution and washed with anhydrous ethanol and deionized water and then dried in air. Fe nanowires (I, II) and PMMA/Fe nanowires (III, IV, and V) were then dispersed on a carbon adhesive tape and observed by SEM. The structural properties of these specimens

 

were analyzed with an X-ray diffractometer. TEM observation further confirmed the specimen's morphology. The magnetic hysteresis properties of all specimens were also analyzed by a VSM analyzer; other correlation characteristics are discussed as well.

### 2.2. Material Properties

The Fe nanowires and Fe nanowires coated with PMMA were characterized by X-ray diffraction, SEM, TEM, TGA analysis and VSM. Powder X-ray diffraction (XRD) patterns of Fe nanowires were obtained by employing NSRRC 17A1 W20 X-ray Powder Diffraction. An SEM HITACHI-S4700 was used to observe the morphology and shape of the Fe nanowires and hybrid PMMA/Fe nanowire materials. High resolution transmission electron microscopy (HRTEM, JEOL JEM-2100F) was used to characterize the morphology of the Fe nanowires and hybrid PMMA/Fe nanowires. The source of synchrotron radiation at the National Synchrotron Radiation Research Center (NSRRC) in Taiwan was used to study the X-ray absorption spectroscopy (XAS) of iron nanowires in the NSRRC 16A and 20A beam line. The fluorescence EXAFS technique was used in this study to detect the X-rays emitted as a result of filling the core hold created by optical absorption.

The magnetic property measurements were carried out with a VSM (Lake Shore 7407, USA) with a maximum magnetic field of 2 T. Thermal degradation was examined with a thermal analyzer (model SDT 2960 Simultaneous DSC-TGA, TA, Germany). Each sample was weighted and filled into Pt crucibles. The samples were heated at a rate of 10℃/min from room temperature to 1400℃ in an oxygen flow of 20 $cm^3$/min. These measurements were conducted under oxygen flow to observe iron oxidation.

## 3. Results and Discussion

### 3.1. Structural Properties

The phase of the reduced iron nanowires has been determined from the XRD pattern as shown in **Figure 1**. Well defined peaks can be observed in the patterns of specimen (I) and (V), corresponding to the existence of a body centered cubic (bcc) phase of iron that coexists with FeO, $Fe_3O_4$ and $Fe_2O_3$ phases in the iron nanowires As indicated in **Figure 1(a)**, specimen (I) is composed of surface iron oxides. For the hard X-ray irradiation specimens (II) and PMMA coated specimens (III-IV), the surface layer of iron oxide gets thicker, as evidenced in **Fig- ures 1(b)**, **(c)** and **(d)**. The results indicate that X-ray irradiation will enhance the oxidation of iron nanowires and affect the magnetic properties of these specimens. Interestingly, after X-ray irradiation, the FeO and $Fe_2O_3$ phases disappear, and only the $Fe_3O_4$ phase can be ob- served. For specimen (V), a pattern similar to specimen (I) can be seen, but it lacks a strong iron [110] peak. Although the synthesis of iron nanowires occurs after X-ray irradiation, the free radicals generated by X-rays are still affecting and inducing trans-grains oxidation of iron nanowires.

### 3.2. Morphology

The morphologies of iron nanowires and hybrid PMMA/ iron nanowires, fabricated with different processing conditions, were characterized by SEM and HRTEM to compare the hard X-ray irradiation effects on them. SEM images of various iron nanowires and PMMA/Fe nanowires are shown in **Figure 2**. The nano wires all show bamboo-like structures. **Figures 2(b)**, **(c)** and **(d)** show that the nanowires have parallel alignment in the same orientation, which may be due to the irradiation or hybridization of PMMA. On the other hand, **Figures 2(a)** and **(e)** show random distribution. As evidenced from the images of electron microscopy, the specimens exhibit orientation arrangement when the Fe nanowires are irradiated by hard X-ray synchrotron radiation. The diameters of both iron nanowires (I) and (II) are all about 40.1 ± 4.2 nm, and the lengths of the nanowires are 584.8 ± 47.2 nm. **Figures 2(c)** and (d) indicate that the diameters of PMMA/Fe nanowires (III) and (IV) are about 23.3 ± 3.9 nm and 31.5 ± 2.5 nm, respectively, and the lengths of these nanowires are 2.7 ± 0.5 μm and 1.1 ± 0.2 μm, respectively. Nanowire (IV) undergoes polymerizations by X-ray irradiation twice, which increases the thickness

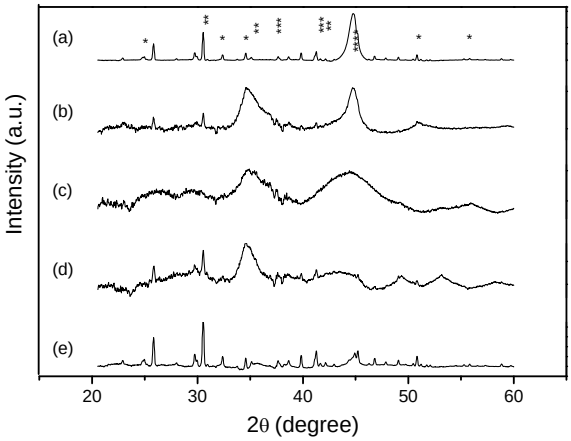


**Figure 1. The XRD diffraction patterns of (a) Fe nanowires (I), (b) Fe nanowires (II) (after hard X-ray irradiation), (c) PMMA/Fe nanowires (III), (d) PMMA/Fe nanowires (IV) and (e) PMMA/Fe nanowires (V). (* $Fe_2O_3$ peaks, ** $Fe_3O_4$ peaks, *** FeO peaks, and **** Fe peaks).**

 

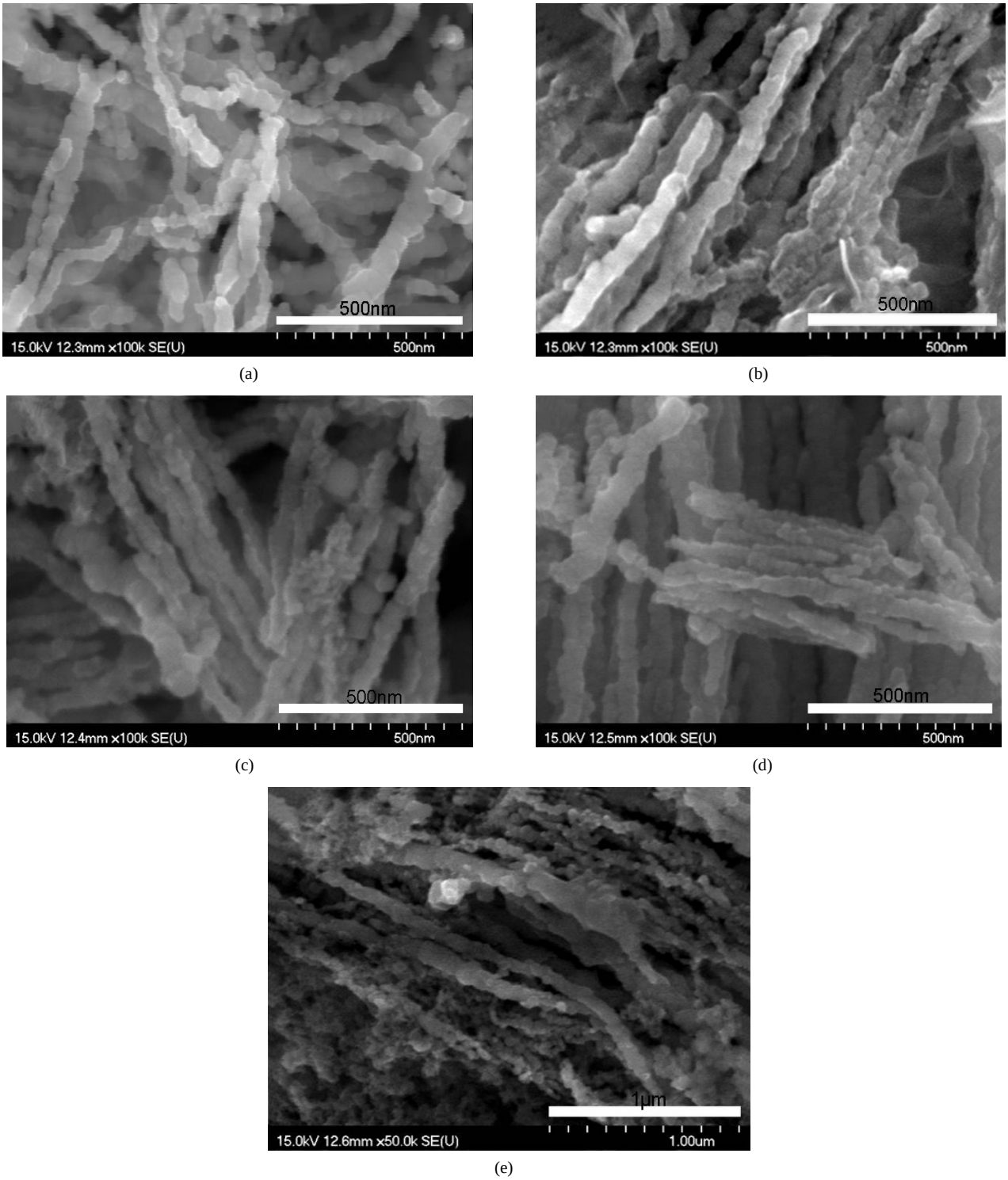


**Figure 2. The SEM images of (a) Fe nanowires (I), (b) Fe nanowires (II) (after hard X-ray irradiation) (c) PMMA/Fe nanowires (III), (d) PMMA/Fe nanowires (IV) and (e) PMMA/Fe nanowires (V).**

of the PMMA, but shortens the length. From the image of **Figure 2(e)**, the morphology of PMMA/iron nanowires looks like a raspberry attached to PMMA/Fe nanoparticles and nanowires. Flocculation is observed

 

between hybrid PMMA/iron nanowires. The average diameter and the average length of specimen (V) are about 36.2 ± 2.8 nm and 1.6 ± 0.4 μm, respectively.

HRTEM images were used to characterize the morphologies and structures of these hybrid materials, as shown in **Figure 3**. For specimen (I) and (II), a thin iron oxide layer formed on the surface of the nanowires, as shown in **Figures 3(a)** and **(b)**. The thickness of the iron oxide layer in specimen (I) and (II) is approximately 4.5 ± 0.8 nm and 3.5 ± 0.2 nm, respectively. It is important to note that for specimen (II), the X-ray irradiation induced oxidation of a thin oxide layer about 1.0 ± 0.1 nm

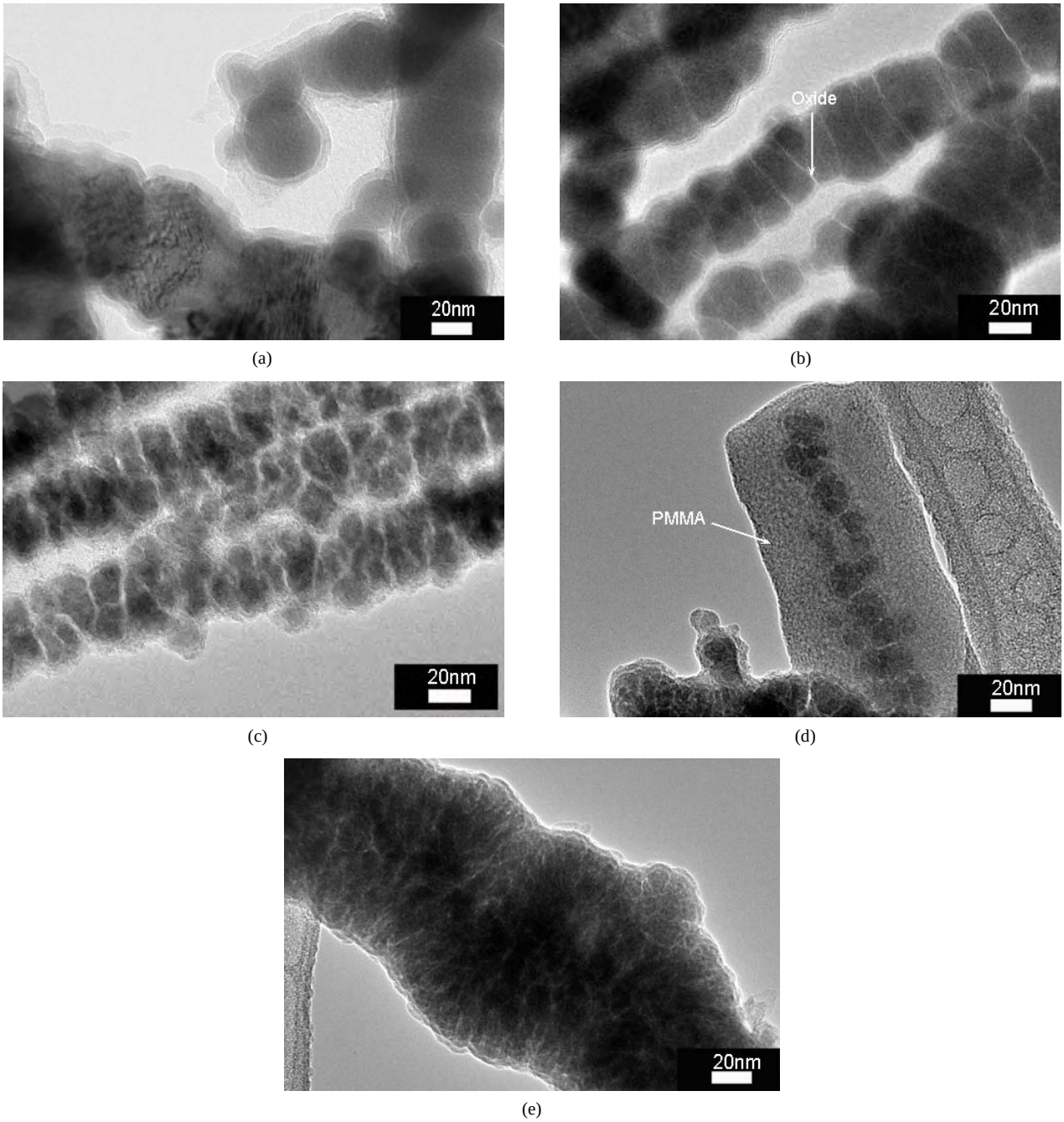


(a) (b) (c) (d) (e)

**Figure 3. TEM images of Fe nanowires and PMMA/iron nanowires hybrid material with different synthesis procedures, (a) Fe nanowires (I), (b) Fe nanowires (II) (after hard X-ray irradiation), (c) PMMA/Fe nanowires (III), (d) PMMA/Fe nanowires (IV) and (e) PMMA/Fe nanowires (V).**

 

between the inner nanograins of iron. The diameter of the iron nanograins was measured from the TEM images in **Figures 3 (a)** and **(b)**. From these, the average diameter of specimen (I) and (II) was determined to be approximately 61.7 ± 3.8 nm and 40.4 ± 11.4 nm, respectively. Thus, X-ray irradiation not only induced oxidation of the iron inner grains, but also refined the iron grain size. This affects the properties of the iron nanowires. **Figures 3(c)**, **(d)** and **(e)** show the coating of PMMA on the iron nanowires. The thickness of the PMMA layer is approximately 4.6 ± 0.5 nm in specimen (III). In specimen (III), the layer of oxide can also be observed between iron nanograins as in specimen (II). This further proves that X-ray irradiation strongly affects the oxidation of iron between its nanograins. Specimen (IV) is not uniformly coated with PMMA, with a thickness of approximately 25.0 ± 0.7 nm.

In this study, iron nanowires were synthesized with or without an MMA monomer, which then underwent hard X-ray polymerization to coat the nanowires in PMMA. Specimen (III) has a more uniform layer coating than specimen (IV). In addition, the PMMA/Fe nanowires (specimen (V)) were grown after PMMA synthesis. The thickness of the PMMA coating layer is approximately 2.6 ± 0.1 nm, which is smaller than specimen (III) and (IV). The X-ray diffraction patterns shown in **Figure 1** indicate that the reduced iron, without a uniform PMMA protection layer, was seriously oxidized by X-ray irradiation. The thickness of the iron oxide layer in hybrid iron nanowires (III), (IV) and (V) are similar and approximately 2.9 ± 0.3 nm, 3.3 ± 0.5 nm and 2.8 ± 0.2 nm, respectively. Specimen (III), (IV) and (V) have a thin oxide layer between their inner iron nanograins that were induced by hard X-ray irradiation and have thicknesses of 1.2 ± 0.1 nm, 1.2 ± 0.1 nm, and 0.5 ± 0.1 nm, respectively. The iron nanowires in specimens (I), (II) and (III) were all irradiated with X-rays. X-ray diffraction patterns indicate that the FeO and $Fe_2O_3$ phases disappeared in these specimens. They indicate that X-ray irradiation induced the reduction of $Fe_2O_3$ to form $Fe_3O_4$ and also caused trans-grain oxidation.

### 3.3. X-ray Absorption Spectroscopy

Iron is widely used in technologically relevant systems. The oxidation of iron surfaces has been extensively studied in the past [8]. Understanding the magnetic properties of these iron nanowires and hybrid PMMA/Iron nanowires requires a precise knowledge of the structure and composition of the oxide layer. This knowledge is important because of the different crystallographic sites of iron atoms in the oxide phases, which result in strongly structure dependent magnetic properties. X-ray absorption spectroscopy is one way to study the oxidation states and the local symmetry of atoms in solids. The X-ray absorption near-edge structure (XANES) depends directly on the oxidation states. The extended X-ray fine structure (EXAFS) includes information on the local structures [9].

The near-edge absorption spectra are acquired at the iron K-edge. The Fe K-edge spectra of the iron nanowires and hybrid PMMA/Fe nanowires samples are shown in **Figure 4**. The pre-edge of the spectra was used to evaluate the sensitivity of XAS to geometric and electronic structural changes [10]. **Figure 4(b)** shows that the iron pre-edge of iron nanowires without X-ray irradiation in specimen (I) is similar to that of commercial pure iron in **Figure 4(a)**. It reveals that a thin oxide layer forms on the surface of as-received iron nanowires. This thin oxide layer also appears in the HRTEM image of **Figure 3(a)**. For specimen (II) to (IV), iron nanowires are all irradiated by high intensity X-rays. They have a similar iron pre-edge as shown in **Figures 4(c)** to **(e)**. The iron pre-edges of these specimens are different than that of reference $Fe_2O_3$ and commercial iron as shown in **Figures 4(g)** and **(a)**, respectively. X-ray diffraction patterns indicate that the $Fe_3O_4$ phase is formed in specimen (II) to (IV). Thus, after X-ray irradiation, the major oxide on the surface of the iron nanowires is the $Fe_3O_4$ phase. This also reveals that X-ray irradiation will induce oxidation of pure iron and reduction of the $Fe_2O_3$ phase. Specimen (V) is prepared with iron nanowires after forming PMMA by X-ray irradiation. Its X-ray diffraction pattern

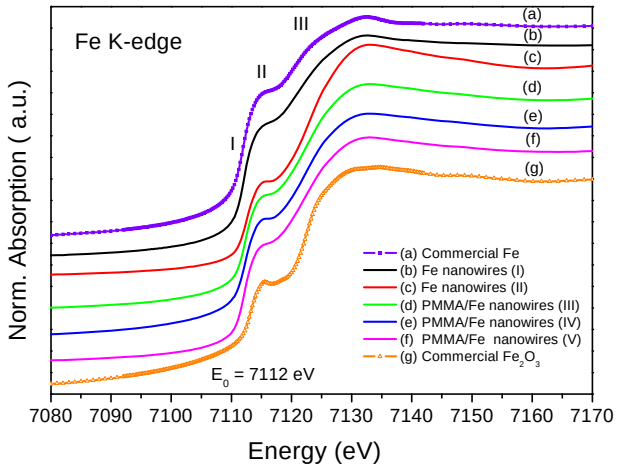


**Figure 4. Fe K-edge of EXAFS of (a) commercial Fe, (b) Fe nanowires (I), (c) Fe nanowires (II) (after hard X-ray irradiation), (d) PMMA/Fe nanowires (III), (e) PMMA/Fe nanowires (IV), (f) PMMA/Fe nanowires (V), and (g) commercial $Fe_2O_3$.**

 

(**Figure 1(e)**) is similar to the iron nanowires without X-ray irradiation in **Figure 1(a)**, only with a lower intensity in the iron peak at around $2\theta = 45^{o}$. The shape of the iron pre-edge of specimen (V) is similar to that of specimen (I) and specimen (II)-(IV). X-ray irradiation effects on the iron oxidephases are enhanced by the formation of $Fe_3O_4$ and the trans-grain oxidation, as indicated in **Figures 3(b)** and **(c)**.

To further examine these results, we differentiated the data of **Figure 4** to obtain the differential pre-edge of the Fe K-edge, as shown in **Figure 5**. The absorption edge differences in these samples are obvious. The first differential pre-edge peak represents the electron transition from the 1s to 4d orbital that directly relates to the oxidation state and geometry of the iron atom [11]. Also, the total intensity of this transition has been shown to in- crease with decreasing coordination number for iron due to the loss of inversion symmetry at the iron site [12]. The differential pre-edge peaks of Fe nanowires are listed in **Table 1**. The differential peak of $Fe_2O_3$ with $Fe^{3+}$ is at 7133.3 eV, which is larger than the 7111.8 eV of com mercial pure iron with Fe. The differential pre-edges of Iron nanowires with or without X-ray irradiation and hybrid PMMA/iron nanowires are all located between $Fe_2O_3$ and pure iron. For pure $Fe_2O_3$, there is a second differential pre-edge peak at 7117.4 eV that is not observed in other specimens, including pure iron. It has been proven that synthesized iron nanowires have an iron oxidation state between $Fe^{2+}$ and $Fe^{3+}$ that forms a surface oxide with an iron core. The position of third differential pre-edge peaks is only observed as the differences between pure iron and iron nanowires (I) and the rest of the specimen. The second and third peaks may have been caused by the 1s-4p transition [13]. It is not sensitive to different oxidation states but is between pure iron and iron oxides.

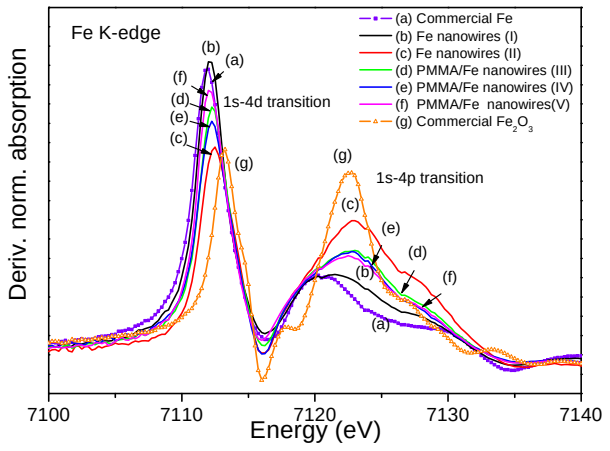


**Figure 5. The differential pre-edge (NEXAFS) of the Fe-K-edge of (a) commercial Fe, (b) Fe nanowires (I), (c) Fe nanowires (II) (after hard X-ray irradiation), (d) PMMA/Fe nanowires (III), (e) PMMA/Fe nanowires (IV), (f) PMMA/ Fe nanowires (V), and (g) commercial $Fe_2O_3$.**

The Fourier-transformed Fe EXAFS data in **Figure 6** indicate that the nearest Fe-O bond appears at about 1.4-1.6 Å for all specimens, corresponding to a tetrahedrally coordinated cation. For commercial iron and iron nanowires without X-ray irradiation, the Fe-Fe bond length of metallic iron is about 2.1Å and can be observed, but not in other specimens. XAS, in this study, was measured in fluorescence mode. Specimens (II) to (V) have a thicker oxide layer compared to specimen (I). Thus, the Fe-Fe bond is not observed in these specimens. The radiation distribution of specimen (II) to (V) shows major differences compared to commercial $Fe_2O_3$. A previous study [14] indicated that the oxide layer in these nanowires is $Fe_3O_4$. XANES of the O K edge spectra in **Figure 7** also shows dramatic differences between $Fe_2O_3$ and the rest of specimens. In the O K-edge, split absorption peaks are observed only in $Fe_2O_3$. This shows that the iron nanowires can be stabilized by the $Fe_3O_4$ surface oxide layer.

As seen in the HRTEM images of **Figure 3**, transgrain oxidation occurs when X-rays irradiate iron nanowires. XAS and XRD results indicate that the oxide phase after X-ray irradiation is mainly $Fe_3O_4$. The oxide layer also got larger after irradiation. The mechanism of X-ray induced oxidation may be the following;

$$2Fe_{(core)} + O_2 \xrightarrow{h\nu} 2FeO \quad (2)$$

$$FeO + Fe_2O_{3(surface)} \xrightarrow{h\nu} Fe_3O_{4(surface)} \quad (3)$$

The iron atoms diffuse out from the core of the nanoparticles that form the iron nanowires. Under X-ray irradiation, iron atoms first oxidize into FeO (Equation 2) and then react with $Fe_2O_3$ to form $Fe_3O_4$ (Equation 3). Thus, the trace $Fe_2O_3$ phase in specimen (I) is transferred into the $Fe_3O_4$ phase, a fact that is proven by XRD and XAS results.

**Table 1. The differential pre-edge peaks of Fe nanowires and PMMA/Fe nanowires.**

| Specimens | First (eV) | Second (eV) | Third (eV) |
|---|---|---|---|
| Fe nanowires (I) | 7112.1 | - | 7120.3 |
| Fe nanowires (II) | 7112.4 | - | 7122.7 |
| PMMA/Fe nanowires (III) | 7112.2 | - | 7122.7 |
| PMMA/Fe nanowires (IV) | 7112.2 | - | 7122.7 |
| PMMA/Fe nanowires (V) | 7112.1 | - | 7122.7 |
| Commercial $Fe_2O_3$ | 7113.3 | 7117.4 | 7122.7 |
| Commercial Fe | 7111.8 | - | 7120.3 |

 

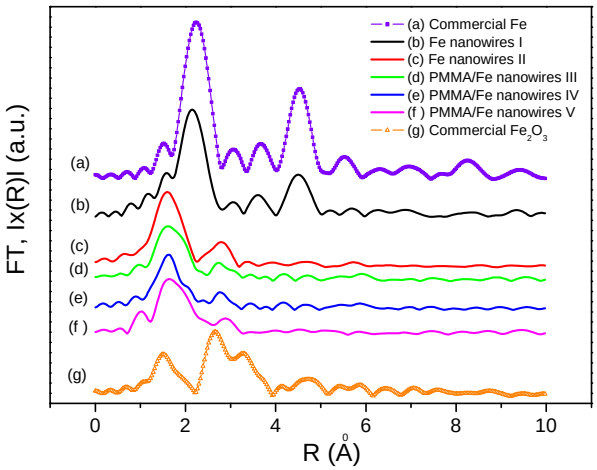


**Figure 6. Fourier-transformed Fe EXAFS data of (a) commercial Fe, (b) Fe nanowires (I), (c) Fe nanowires (II) (after hard X-ray irradiation), (d) PMMA/Fe nanowires (III), (e) PMMA/Fe nanowires (IV), (f) PMMA/Fe nanowires (V), and (g) commercial $Fe_2O_3$.**

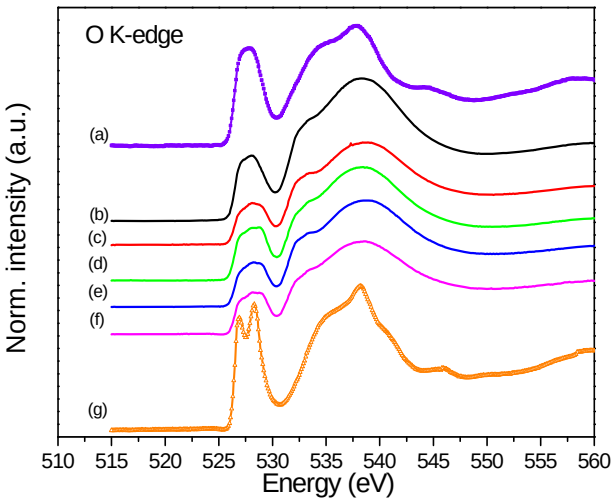


**Figure 7. XANES normalized intensity of the O K edge spec tra of (a) commercial Fe, (b) Fe nanowires (I), (c) Fe nanowires (II) (after hard X-ray irradiation), (d) PMMA/Fe nanowires (III), (e) PMMA/Fe nanowires (IV), (f) PMMA/Fe nanowires (V), and (g) commercial Fe2O3.**

## 3.4. TGA Analysis

To measure the mass content of the specimens, the iron nanowires and the hybrid PMMA/Fe nanowires were examined by TGA analysis with an SDT2960 Simultaneous DSC-TGA (TA Instruments) system. The results are shown in **Figure 8**. The curves show mass decreases in specimen (I), (II), (III), (IV) and (V) prior to 166, 303, 216, 254 and 324℃, respectively, under oxygen atmosphere. Specimen (I), (II), (III), (IV) and (V), had around

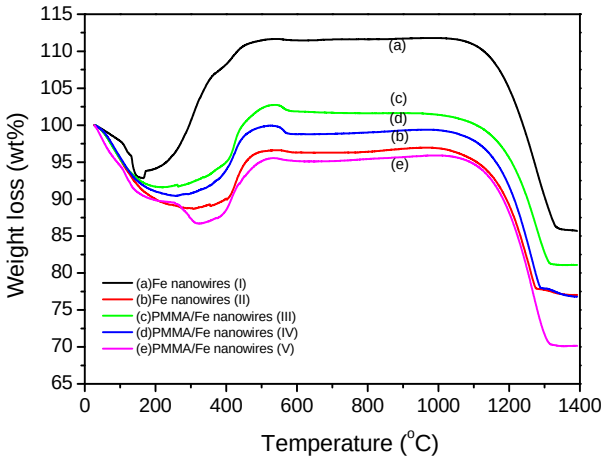


**Figure 8. The TGA spectrums of (a) Fe nanowires (I), (b) Fe nanowires (II) (after hard X-ray irradiation), (c) PMMA/Fe nanowires (III), (d) PMMA/Fe nanowires (IV) and (e) PMMA/Fe nanowires (V).**

7.18, 11.29, 8.48, 9.56, and 13.31 wt% mass loss, respectively, including water, methanol and thermal decomposition of hydroxide materials. Then, the iron nanowires started to oxidize and PMMA began to decompose. After PMMA completely decomposed, the weights of the specimens were greater than 100%, due to iron oxide formation. Specimens (III), (IV) and (V) have a peak at around 500℃ that may have been cause by the carbonization of PMMA. The Curve (a) for specimen (I) in **Figure 8** shows that the oxidation temperature of iron nanowires is lower than that of other specimens. This indicates that the iron nanowires without X-ray or PMMA treatments are oxidized more easily than other specimens. This shows that the inner nanograins of specimen (II) to (V) are protected by thin layers of oxides that resist oxidation at lower temperatures. The weight gain of specimen (I) due to oxidation is great larger than that of specimen (II). This indicates that the iron nanowires treated by X-ray irradiation are highly oxidized. This phenomenon is also proven by the X-ray dif- fraction pattern in **Figure 1**. The major diffraction peak of pure iron in specimen (II) is from dramatic reduction. Specimens (III) to (V) show the same phenomenon as specimen (II). Pure PMMA usually decomposes before 430℃, but the weight gain peak decreased in specimens (III), (IV) and (V) when the temperature was higher than 600℃. This may be due to further decomposition of the residues of carbonized PMMA. The iron oxides were reduced at temperatures higher than 1100℃, which causes weight loss in the TGA thermogram. At temperatures > 1350℃, the

 

residual weight of the specimens indicates their iron content. The residue weight of specimen (II) at 1350℃ is 77.0wt%, less than that of specimen (I), which is about 85.8wt%, as shown in **Figure 8**. This confirms that X-ray irradiation induced the oxidation of specimen (II). Thus, the oxide content in specimen (II) is larger than in specimen (I). According to residual weight in the TGA thermogram, the iron contents of specimens (I) to (V) are about 85.8, 77.0, 81.2, 76.7 and 70.1wt%, respectively.

### 3.5. Magnetic Properties

It was recently shown that nanometer thick native-oxide layers can be used as building blocks in new magnetic structures [15]. For multilayers consisting of alternating Fe and Fe-oxide layers, the magnetic moments of the Fe layers are arranged in a non-collinear fashion [16]. The structure of nanowires after X-ray irradiation can build a chain of iron nanoparticle/iron nano oxide layer structures. This may lead to novel magnetic materials for application in the electronics or medical fields.

The magnetic properties of the various specimens are examined at room temperature by VSM. **Figure 9** and **Table 2** show magnetic hysteresis curves and data of these specimens, respectively. The hysteresis loops of specimens (I), (II), (III), (IV) and (V) reveal their ferromagnetic behavior. Specimen (II), with X-ray irradiation, has a saturation magnetization (Ms) that is 173 emu/g larger than that of specimen (I) (138 emu/g). Their remanences (Mr) are 64 and 51 emu/g, respectively. TEM images of **Figure 3 (a)** and **(b)** show that the diameter of iron nanograins is approximately 40.4 ± 11.4 nm for specimen (II) and 61.7 ± 3.8 nm for specimen (I). These results demonstrate that hard X-ray irradiation causes the refinement of grain size and also induces oxidation reactions in iron nanograins. For specimens (I) and (II), the coercivity (Hc) is 789 Oe (reduced remanence ratio 0.37) and 324 Oe (reduced remanence ratio 0.37), respectively. The saturation magnetization of PMMA/Fe nanowires (III, IV and V) is 101, 82 and 71 emu/g; the coercivity is 171, 116 and 60 Oe; and remanence is 39, 31 and 13 emu/g, respectively.

The magnetic properties of these specimens are attributed to the size and structure of the iron and iron oxides. For specimens (I) and (II), it is clear that X-ray irradiation induces size refinement and reduction of iron oxide. The $Fe_2O_3$ phase is reduced to $Fe_3O_4$. This is not only the case in specimen (II). Specimens (III) and (IV) are also only reduced to $Fe_3O_4$ as observed in X-ray diffraction patterns. These nanowires are synthesized under strong magnetic fields, which arranged the nanograins in magnetically preferred orientation.

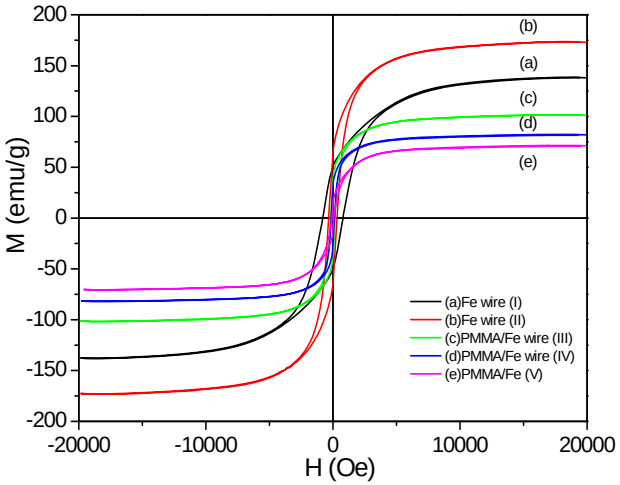


**Figure 9. The VSM measurements of (a) Fe nanowires (I), (b) Fe nanowires (II) (after hard X-ray irradiation), (c) PMMA/Fe nanowires (III), (d) PMMA/Fe nanowires (IV) and (e) PMMA/Fe nanowires (V).**

**Table 2. The VSM measured data of Fe nanowires and PMMA/Fe nanowires.**

| Specimens | Hc (Oe) | Mr (emu/g) | Ms (emu/g) | Sr = Mr/Ms |
|---|---|---|---|---|
| Fe nanowires (I) | 789 | 51 | 138 | 0.37 |
| Fe nanowires (II) | 324 | 64 | 173 | 0.37 |
| PMMA/Fe nanowires (III) | 171 | 39 | 101 | 0.39 |
| PMMA/Fe nanowires (IV) | 116 | 31 | 82 | 0.38 |
| PMMA/Fe nanowires (V) | 60 | 13 | 71 | 0.18 |

The magnetic saturation of iron nanowires and PMMA/iron nanowires is higher than that of the spherecal Fe colloids produced by sonochemical synthesis (101 emu/g) [17] or iron nanoparticles produced by metal vapor deposition (55 emu/g) [18]. **Figure 1** shows the effect of the remaining $Fe_2O_3$ and $Fe_3O_4$ phases. Both remanence and coercivity are affected by the volume fraction of the $Fe_3O_4$ phase. The magnetic properties of iron nanowires are similar to nanocrystalline soft materials where the magnetization averages over several grains [19]. The exchange interactions between iron nanograins in nanowires due to agglomeration account for the remanence enhancement and the drop of the coercive field as shown in specimen (II) with respect to the Stoner–Wohlfarth value [20].

## 4. Conclusions

In summary, iron nanowires and hybrid PMMA/Fe nanowires were successfully synthesized with the

 

reducing agent $NaBH_4$ under an externally applied magnetic field with radiation polymerization. The externally applied magnetic field played an important role in the formation of uniform and parallel iron nanowires.

The bamboo-like structure of the iron nanowires could be observed by SEM and HRTEM. An oxide layer formed on the surface of the iron nanowires. XRD results showed that the $Fe_2O_3$ and $Fe_3O_4$ phases coexisted in the iron nanowires without X-ray irradiation. When these samples are irradiated by hard X-ray from NSRRC, $Fe_3O_4$ is the only phase that can be observed. The Fe and O K-edges of XAS were used to distinguish the oxide structures on the surface of the iron nanowires and PMMA/iron nanowires. The results of XAS show the phase transformation of $Fe_2O_3$ to $Fe_3O_4$. Thus, X-ray irradiation will induce $Fe_2O_3$ phase transformation to $Fe_3O_4$ and stabilize these iron nanowires. TGA analysis is used here to determine the thermal properties and solid content of these specimens.

Magnetic hysteresis measurements reveal that the iron nanowires displayed ferromagnetic behavior. For the iron nanowires (specimen (II)) prepared after X-ray irradiation, the saturation magnetization is 173 (emu/g) larger than that of the initial iron nanowires (specimen (I)). The saturation magnetization of the iron nanowires and PMMA/iron nanowires is higher than that of spherical Fe colloids produced by sonochemical synthesis or iron nanoparticles produced by metal vapor deposition. Iron nanowires-coated PMMA hybrid materials could be designed to manipulate the magnetic and biocompatibility properties for application in magnetic hyperthermia. This study indicates that X-ray irradiation treatment of these iron nanowires will provide a way to manipulate the structural and magnetic properties of novel hybrid nano-materials.

## 5. Acknowledgment

The authors gratefully acknowledge the National Science Council, Taiwan, for financial support, and the TLS (01A) team of the National Synchrotron Radiation Research Center (NSRRC) for technical support.

## REFERENCES

[1] L. Menon, M. Zheng, H. Zeng, S. Bandyopadhyay and D. J. Sellmyer, "Size Dependence of the Magnetic Properties of Electrochemically Self-Assembled Fe Quantum Dots," *Journal of Electronic Materials*, Vol. 29, No. 5, pp. 510-515.

[2] S. Bandyopadhyay, L. Menon, N. Kouklin, H. Zeng and D. J. Sellmyer, "Electrochemically Self-Assembled Quantum Dot Arrays," *Journal of Electronic Materials*, Vol. 28, No. 5, 2000, pp. 515-519.

[3] M. Zheng, L. Menon, H. Zeng, Y. Liu, S. Bandyopadhyay, R. D. Kirby and D. J. Sellmyer, "Magnetic Properties of Ni Nanowires in Self-Assembled Arrays," *Physical Review B*, Vol. 62, No. 18, 2000, pp. 12282-12286.

[4] S. Pan, Z. An, J. Zhang, and G. Song, "Facile Synthesis of Prickly CoNi Microwires," *Materials Letters*, Vol. 64, No. 3, 2010, pp. 453-456.

[5] P. Liu, Z. Li, B. Zhao, B. Yadian, B. and Y. Zhang, "Template–Free Synthesis of Nickel Nanowires by Magnetic Field," *Materials Letters*, Vol. 63, No. 20, 2009, pp. 1650-1652.

[6] H. Liou, W. Liou, H. Lin, Y. Hwu and W. Chen, "Characterization of Gold/PMMA Hybrid Nanomaterials Synthesized by Hard X-Ray Synchrotron Radiation," *Particuology*, Vol. 8, No. 3, pp. 234-239.

[7] H. M. Lin, C. K. Lin and Y. K. Hwu, "X-Ray Absorption Techniques in Examination the Structural Properties of Nanocrystalline Materials," *Fu Jen Studies, Science and Engineering*, Vol. 38, 2004, pp. 1-26.

[8] S. J. Roosendaal, A. M. Vredenberg and F. H. P. M. Habraken, "Oxidation of Iron: The Relation between Oxidation Kinetics and Oxide Electronic Structure," *Physical Review Letters*, Vol. 84, No. 15, 2000, pp. 3366-3369.

[9] S. Couet, T. H. Diederich, K. Schlage and R. Röhlsberger, "A Compact UHV Deposition System for *in situ* Study of Ultrathin Films via Hard X-Ray Scattering and Spectroscopy," *Review of Scientific Instruments*, Vol. 79, No. 9, 2008, pp. 093908-1-093908-9.

[10] G. Giuli, G. Pratesi, C. Ciprianiand and E. Paris, "Iron Local Structure in Tektites and Impact Glasses by Extended X-Ray Absorption Fine Structure and High-Resolution X-Ray Absorption Near-Edge Structure Spectroscopy," *Geochimica et Cosmochimica Acta*, Vol. 66, No. 24, 2002, pp. 4347-4353.

[11] R. G. Shulman, Y. Yafet, P. Eisenberger and W. E. Blumberg, "Observation and Interpretation of X-Ray Absorption Edges in Iron Compounds and Proteins," *Proceedings of the National Academy of Sciences of the United States of America*, Vol. 73, No. 5, 1976, pp. 1384-1388.

[12] C. R. Randall, L. Shu, Y. M. Chiou, K. S. Hagen, M. Ito, N. Kitajima, R. J. Lachicotte, Y. Zang and L. Jr. Que, "X-Ray Absorption Pre-Edge Studies of High-Spin Iron (II) Complexes," *Inorganic Chemistry*, Vol. 34, No. 5, 1995, pp. 1036-1039.

[13] T. E. Westre, P. Kennepohl, J. G. DeWitt, B. Hedman, K. O. Hodgson and E. I. Solomon, "A Multiplet Analysis of Fe K-Edge 1s → 3d Pre-Edge Features of Iron Complexes," *Journal of The America Chemical Society*, Vol. 119, No. 27, 1997, pp. 6297-6314.

[14] S. Son, M. Taheri, E. Carpenter, V. G. Harris and M. E. McHenry, "Synthesis of Ferrite and Nickel Ferrite Nanoparticles Using Radio-Frequency Thermal Plasma Torch," *Journal of Applied Physics*, Vol. 91, No. 10, 2002, pp.

 

7589-7591.

[15] G. S. D. Beach, F. T. Parker, D. J. Smith, P. A. Crozier and A. E. Berkowitz, "New Magnetic Order in Buried Native Iron Oxide Layers," *Physical Review Letters*, Vol. 91, No. 26, 2003, pp. 267201-1-267201-4.

[16] T. H. Diederich, S. Couet and R. Röhlsberger, "Non-collinear Coupling of Iron Layers through Native Iron Oxide Spacers," *Physical Review B*, Vol. 76, No. 5, 2007, pp. 054401-1-054401-5.

[17] K. S. Suslick, M. Fang and T. Hyeon, "Sonochemical Synthesis of Iron Colloids," *Journal of the America Chemical Society*, Vol. 118, No. 47, 1996, pp. 11960-11961.

[18] C. F. Kernizan, K. J. Klabunde, C. M. Sorensen and G. C. Hadjipanayis, "Magnetic Properties of Nanometer-Scale Iron Particles Generated by Iron Atom Clustering in Cold Pentane," *Chemistry of Materials*, Vol. 2, No. 1, 1990, pp. 70-74.

[19] W. J. M. Mulder, G. J. Strijkers, G. A. F. van Tilborg, A, W. Griffioen and K. Nicolay, "Lipid-Based Nanoparticles for Contrast-Enhanced MRI and Molecular Imaging," *NMR in Biomedicine*, Vol. 19, No. 1, 2006, pp. 142-164.

[20] E. V. Shtykova, X. Huang, N. Remmes, D. Baxter, B. Stein, B. Dragnea, D. I. Svergun and L. M. Bronstein, "Structure and Properties of Iron Oxide Nanoparticles Encapsulated by Phospholipids with Poly(ethylene glycol) Tails," *The Journal of Physical Chemistry C*, Vol. 111, No. 49, 2007, pp. 18078-18086.

 

*Journal of Biomaterials and Nanobiotechnology*, **2010, 1, 61-76**
doi:10.4236/jbnb.2010.11008 Published Online October 2010 (http://www.SciRP.org/journal/jbnb)

# Review Article: Immobilized Molecules Using Biomaterials and Nanobiotechnology

**Magdy M.M. Elnashar**

Centre of Scientific Excellence - Polymers Department - Advanced Materials & Nanotechnology Laboratory, National Research Center, El-Behooth St., Dokki, Cairo, Egypt.
Email: magmel@gmail.com

Received August 24th, 2010; revised October 15th, 2010; accepted October 21st, 2010.

## ABSTRACT

*Immobilized molecules using biomaterials and nanobiotechnology is a very interesting topic that touching almost all aspects of our life. It uses the sciences of biology, chemistry, physics, materials engineering and computer science to develop instruments and products that are at the cutting edge of some of today's most promising scientific frontiers. In this review article, the author based on his experience in this arena has tried to focus on some of the supports for immobilization; the most important molecules to be immobilized such as DNA, cells, enzymes, metals, polysaccharides, etc and their applications in medicine, food, drug, water treatment, energy and even in aerospace. He specified a special section on what is new in the arena of supports and technologies used in enzyme immobilization and finally a recommendation by the author for future work with a special attention to up-to-date references.*

***Keywords*: *Immobilized molecules, Biotechnology, Enzymes, Biomaterials, Nanobiotechnology***

## 1. Introduction

### 1.1. Some Important Definitions

#### 1.1.1. Definition of Biotechnology

The European Federation of Biotechnology defined biotechnology as "the integration of natural sciences and engineering in order to achieve the application of organisms, cells, parts thereof and molecular analogues for products and services" [1]. In other words, Biotech applications can be divided into 5 key sectors: ***biomedicine, bioagriculture, industrial biotechnology, bioenergy, and bioenvironment***.

#### 1.1.2. Definition of Immobilization

An immobilized molecule is one whose movement in space has been restricted either completely or to a small limited region by attachment to a solid structure. In general the term immobilization refers to the act of the limiting movement or making incapable of movement i.e., retard the movement [2].

### 1.2. History of Immobilization

Immobilization is a natural phenomenon existing in the universe. Microorganisms in nature are irregularly distributed and often exist in Biofilms. ***Biofilms are surface-attached microbial*** communities consisting of multiple layers of cells embedded in hydrated matrices [3]. Biofilms were first extensively studied during the 1940s but it was not until the 1970s that it was appreciated that their formation occurs in almost all natural environments. A rock immersed in a stream, an implant in the human body, a tooth, a water pipe or conduit, etc. are all sites where Biofilms develop [4]. This natural phenomenon encouraged humans to utilize it for his services.

### 1.3. What Can We Immobilize?

Many molecules have been immobilized and the majority of them are biomolecules due to their biological and biomedical applications. The following are examples of some of these molecules:

• ***Proteins:***

− Enzymes, antibodies, antigens, cell adhesion molecules and "Blocking" proteins

• ***Peptides:***

− Substances composed of amino acids

• ***Drugs:***

− Anticancer agents, antithrombogenic agents, antibiotics, contraceptives, drug antagonists and peptide/protein drugs

• ***Saccharides:***

− Sugars, oligosaccharides and polysaccharides

 

• ***Lipids:***

− Fatty acids, phospholipids, glycolipids and any fat-like substances.

• ***Ligands:***

− Hormone receptors, cell surface receptors, avidin and biotin

− In immunology, small molecules that are bound to another chemical group or molecule

• ***Nucleic acids and nucleotides:***

− DNA, RNA

− High MW substances formed of sugars, phosphoric acid, and nitrogen bases (purines and pyrimidines).

• ***Others:***

− Conjugates or mixtures of any of the above

## 1.4. Methods of Immobilization

The methods of immobilization of the different molecules are almost the same. However, according to **Cao, L. 2005** [5] there is no general universally applicable method of certain molecule immobilization. As enzyme molecules alone or in combination with drugs, antibodies and antigens, are the most used in industries, ***we will be focusing on the immobilization techniques used for enzymes*** as a model of other immobilized molecules. The enzyme market in 2005 was around **2.65** ***billion dollars***, with an expected annual growth of more than 9% [6]. On the industrial level, 75% of the enzymes were used, which is around **2** ***billion dollars***.

However, expensive enzymes are not favored to be used in industries in the Free State as they are difficult to be separated from the products (**Figure 1a**) and consequently are lost after the first use. They were alternatively immobilized on solid supports (**Figure 1b**) so that they can be easily separated from the products by simple filtration or using a fluidized magnetized bed reactor system [7-14].

***The main advantage for enzyme immobilization*** is the easy separation of the enzyme from the reaction mixture (substrates and products) and its reusability for tens of time, which reduces the enzyme and the enzymatic products cost tremendously. Beside this splendid advantage, the immobilization process imparts many other advantages to the enzyme such as:

- The ability to stop the reaction rapidly by removing the enzyme from the reaction solution (or vice versa)
- Product is not contaminated with the enzyme
- Easy separation of enzyme from the product (especially useful in food and pharmaceutical industries)
- Enhancement of enzyme stability against pH, temperature, solvents, contaminants, and impurities.

Immobilization provides a physical support for enzymes, cells and other molecules. Immobilization of enzymes is one of the main methods used to stabilize free enzymes [7,8]. The support material and the main methods of immobilization are key parameters in enzyme immobilization. There are ***five principal methods for immobilization*** of enzymes and cells (adsorption, covalent, entrapment, encapsulation and crosslinking) and no one method is perfect for all molecules or purposes. However, **Katzbauer and Moser, 1995** [15] represented a classification of combination between these methods.

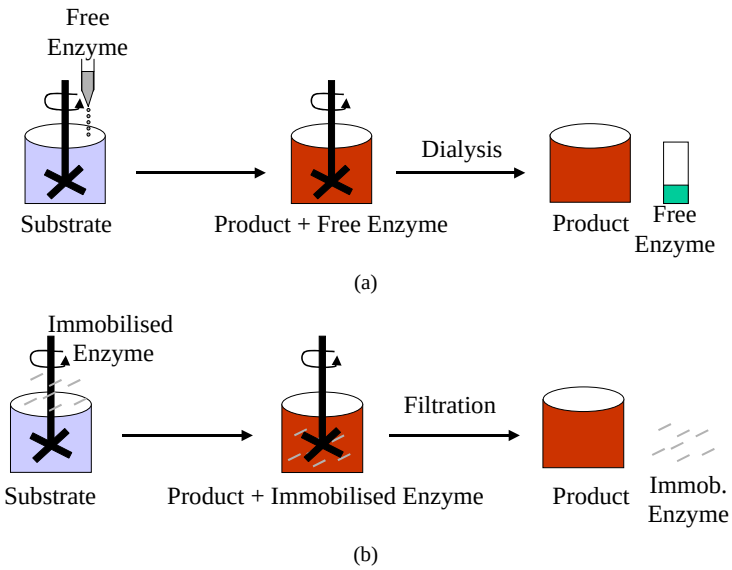


**Figure 1. Schematic diagram of free and immobilized enzyme reactions. (a) Reaction of free enzyme with substrate and formation of product, which has to be separated via dialysis; (b) Reaction of immobilized enzyme with substrate and formation of product, which can be separated via filtration or using a fluidized magnetized bed reactor system.**

 

### 1.4.1. Adsorption

Immobilization by adsorption is the simplest method and involves reversible surface interactions between enzyme and support material as shown in **Figure 2**. The procedure of adsorption consists of mixing together the biological component(s) and a support with adsorption properties, under suitable conditions of pH and ionic strength for a period of incubation, followed by collection of the immobilized material and extensive washing to remove the unbound biological components. The first industrially used immobilized enzyme was prepared by adsorption of amino acid acylase on DEAE-cellulose [16]. **Menaa *et al.* (2008a)** [17] reported the role of hydrophobic surfaces of nanoporous silica glasses on protein folding enhancement.

***Advantages of enzymes immobilized using the adsorption technique:***

- ***Reversibility***, which enables not only the purification of proteins but also the reuse of the carriers;
- ***Simplicity***, which enables enzyme immobilization under mild conditions;
- ***Possible high retention of activity*** because there is no chemical modification [18];
- ***Cheap and quick*** method;
- ***No chemical changes*** to the support or enzyme occurs.

***Disadvantages of enzymes immobilized using the adsorption technique:***

- The immobilized enzymes prepared by adsorption tend to leak from the carriers, owing to the relatively weak interaction between the enzyme and the carrier, which can be destroyed by desorption forces such as high ionic strength, pH, etc,
- Contamination of product,
- Non-specific binding,
- Overloading on the support and
- Steric hindrance by the support.

Consequently, a number of variations have been developed in recent decades to solve this intrinsic drawback. Examples are adsorption–cross-linking; modification–adsorption; selective adsorption–covalent attachment; and adsorption–coating, etc. For more details, the reader is recommended to read the book of **Cao L, 2005** [5].

### 1.4.2. Covalent Binding

This method of immobilization involves formation of a covalent bond between the enzyme and support material as shown in **Figure 3**. Covalent bonds usually provide the strongest linkages between enzyme and carrier, compared with other types of enzyme immobilization methods. Thus, leakage of enzyme from the matrix used is often minimized with covalently bound immobilized enzymes [5]. The bond is normally formed between functional groups present on the surface of the support and functional groups belonging to amino acid residues on the surface of the enzyme.

Multi-step immobilization is one of the technologies to enhance enzyme covalent immobilization [19]. There are many reaction procedures for coupling an enzyme to a support via covalent bond however, most reactions fall into the following categories: formation of an isourea linkage; formation of a diazo linkage; formation of a peptide bond or an alkylation reaction as shown in **Table 1**.

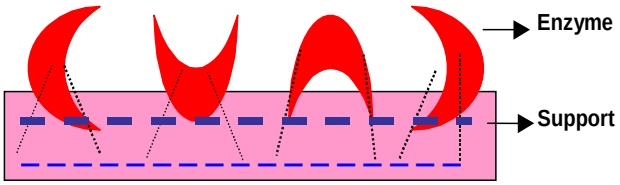


**Figure 2. Immobilization of enzymes using the adsorption technique.**

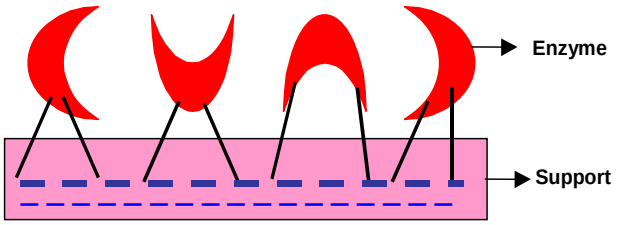


**Figure 3. Immobilization of enzymes using the covalent technique.**

**Table 1. Different methods for covalent binding of enzymes to supports.**

| Reaction | Support – Enzyme Linkage |
|---|---|
| Diazotization | **SUPPORT--N=N---ENZYME** |
| Alkylation and arylation | **SUPPORT--CH2-NH---ENZYME**<br>**SUPPORT--CH2-S---ENZYME** |
| Schiff's base formation | **SUPPORT---CH=N---ENZYME** |
| Amide bond formation | **SUPPORT---CO-NH---ENZYME** |
| Amidation reaction | **SUPPORT---CNH-NH---ENZYME** |
| Thiol-Disulfide interchange | **SUPPORT---S-S---ENZYME** |
| Carrier binding with bifunctional reagents | **SUPPORT---O(CH2)2 N=CH(CH2)3 CH=N---ENZYME** |

 

***Advantages of enzymes immobilized using the covalent technique:***

- ***No leakage*** of enzyme.
- The enzyme can be easily in contact to substrate due to the localization of enzyme on support materials.
- Increase of the thermal stability.

***Disadvantages of enzymes immobilized using the covalent technique:***

- ***The cost is quite high*** as the good supports are very expensive (e.g. Eupergit C and Agaroses).
- Loss of enzyme activity (e.g. mismatched orientation of enzyme on the carriers such as involvement of active centre in the binding).

### 1.4.3. Entrapment

Immobilization by entrapment differs from adsorption and covalent binding as shown in **Figure 4** in that enzyme molecules are free in solution, but restricted in movement by the lattice structure of a gel [20]. The porosity of the gel lattice is controlled to ensure that the structure is tight enough to prevent leakage of enzyme or cells, yet at the same time allows free movement of substrate and product. The support also acts as a barrier and can be advantageous as it protects the immobilized enzyme from microbial contamination by harmful cells, proteins, and enzymes in the microenvironment [21].

Entrapment can be achieved by mixing an enzyme with a polyionic polymer material, such as carrageenan, and by crosslinking the polymer with multivalent cations, e.g. hexamethylene diamine, in an ion-exchange reaction to form a lattice structure that traps the enzymes, this is termed ionotropic gelations.

***Advantages of enzymes immobilized using the entrapment technique:***

- ***Enzyme loading is very high***

***Disdvantages of enzymes immobilized using the entrapment technique:***

- ***Enzyme leakage*** from the support.
- ***Diffusion*** of the substrate to the enzyme and of the product away from the enzyme (***diffusion limitation***).

### 1.4.4. Encapsulation

Encapsulation of enzymes as shown in **Figure 5** can be achieved by enveloping the biological components within various forms of semipermeable membranes [22]. It is similar to entrapment in that the enzyme is free in solution, but restricted in space. Large proteins or enzymes can not pass out of, or into the capsule, but small substrates and products can pass freely across the semipermeable membrane. Many materials have been used to construct microcapsules varying from 10-100 μm in diameter. For example, nylon and cellulose nitrate have proven popular. Ionotropic gelation of alginates have proven it efficacy as well for ***encapsulation of drugs, enzymes and cells*** [23]. On the nano scale level, **Menaa *et al*., 2008b, 2009 & 2010** [24-26] used Silica-based nanoporous sol-gel glasses for the study of encapsulation and stabilization of some proteins.

***Advantages of enzymes immobilized using the encapsulation technique:***

- The enzymes could be encapsulated inside the cell.
- Possibility of coimmobilization. Where cells and/or enzymes may be immobilized in any desired combination to suit particular applications.

***Disdvantages of enzymes immobilized using the entrapment technique:***

- The problems associated with diffusion are acute and may result in ***rupture of the membrane*** if products from a reaction accumulate rapidly.

### 1.4.5. Crosslinking

This type of immobilization is support-free as shown in **Figure 6** and involves joining enzyme molecules to each other to form a large, three-dimensional complex structure, and can be achieved by chemical or physical methods [19]. Chemical methods of crosslinking normally

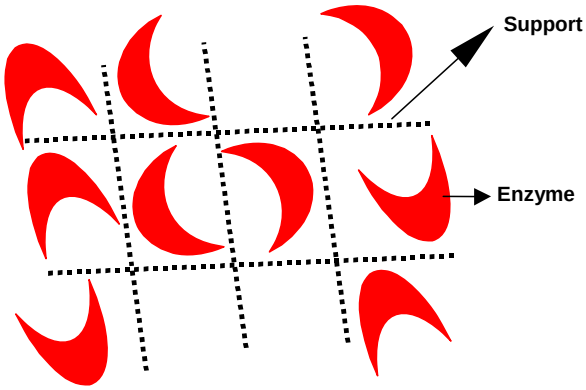


**Figure 4. Immobilization of enzyme using the entrapment technique.**

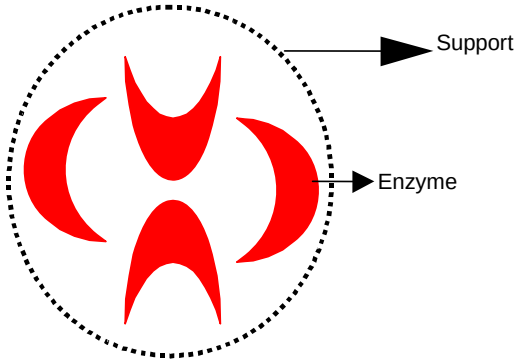


**Figure 5. Immobilization of enzymes using the encapsulation technique.**

 

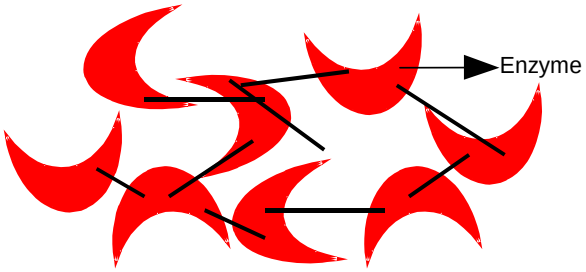


**Figure 6. Crosslinking technique.**

involve covalent bond formation between the enzymes by means of a bi- or multifunctional reagent, such as glutaraldehyde, dicarboxylic acid or toluene diisocyanate. Flocculating agents, such as polyamines, polyethyleneimine, polystyrene sulfonates, and various phosphates, have been used extensively to cross-link cells using physical bonds. Crosslinking is rarely used as the only means of immobilization, because ***poor mechanical properties*** of the aggregates ***are severe*** limitations. Crosslinking is most often used to enhance the other methods of immobilization described.

***Advantages of enzymes immobilized using the crosslinking technique:***

- The immobilization is ***support-free***.
- Cross-linking between the same enzyme molecules stabilises the enzymes by increasing the rigidity of the structure

***Disdvantages of enzymes immobilized using the crosslinking technique:***

- ***Harshness of reagents*** of crooslinking is a limiting factor in applying this method to many enzymes.
- The enzyme may partially lose activity or become totally inactivated in case the cross-linking reagent reacted across the active site.

## 1.5. Examples of Matrices and Shapes for Immobilization

Matrices for immobilization can be classified according to their chemical composition as organic and inorganic supports. The former can be further classified into natural and synthetic matrices as in **Table 2** [27]**.**

***The shape of the carrier*** can be classified into two types, *i.e.* irregular and regular shapes such as (A): beads; (B): fibres; (C): hollow spheres; (D): thin films; (E): discs and (F): membranes**.** Selection of the geometric properties for an immobilized molecule is largely dependent on the peculiarity of certain applications.

**Table 2. Chemical classification of enzyme matrices.**

| Organic | Inorganic |
|---|---|
| **Natural polymers** | **Minerals** |
| **Polysaccharides** | Attapulgite clays |
| Cellulose | Bentonite |
| Dextran | Kieselgur |
| Starch | Pumic stone |
| Agar and agarose | Hornblend |
| Alginate | Diatomaceous earth |
| Carrageenans | Sand |
| Chitin and chitosan | |
| **Proteins** | |
| Collagen | |
| Gelatin | |
| Albumin | |
| Ferritin | |
| **Synthetic polymers** | **Fabricated materials** |
| Polystyrene | Non-porous glass |
| Polyacrylate and polymethacrylate | Controlled pore glass |
| Polyacrylamides | Controlled pore metal oxides |
| Hydroxyalkyl methacrylate | Alumina catalyst |
| Vinyl polymer | Porous silica |
| Maleic anhydride polymer | Silochrome |
| Polyethyleneglycol | Iron oxide |
| Aldehyde-based polymer | Stainless steel |

 

***Gel disks*** are widely used in the literature. Researchers usually use the casting method, e.g. a Petri dish, to make a single film of gel and then cut it into disks using cork borers. **Elnashar *et al.*, 2005** [28], invented a new equipment to make many uniform films in one step and with high accuracy using the equipment "Parallel Plates" as shown in **Figure 7.**

***Gel beads*** are mostly used in industries as they have the largest surface area and can be formed by many techniques such as the interphase technique, ionic gelation methods, dripping method and the Innotech Encapsulator [7,10]. The Innotech Encapsulator as shown in **Figure 8** has the advantage of high bead production (50 – 3000 beads per second depending on bead size and encapsulation-product mixture viscosity), which is suitable for the scaling up production on the industrial scale.

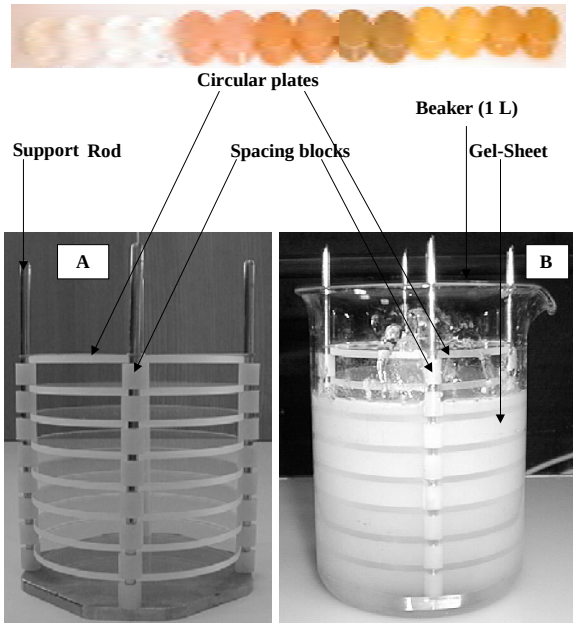


**Figure 7. Parallel plates equipment for making uniform k-carrageenan gel disks.**

**Figure 8. Inotech Encapsulator IE-50 R.**

## 1.6. Properties of Matrices for Immobilization

The supports on which molecules such as enzymes, antibodies, antigens, etc will be immobilized are of great interest. The term support or media is usually understood to refer to a combination of a ligand that is firmly attached often by covalent means, and a solid insoluble matrix. These supports have to exhibit good chemical and physical stability and contain available functional groups to bind to the active molecule. To use a support for immobilization of active molecules such as enzymes, a range of fundamental properties are required, which are summarised as follows [20].

a) Availability of matrix from a reliable commercial source

b) Matrix has an abundance of easily derivatizable functional groups

c) Matrix has good mechanical and chemical stability

d) Matrix has good capacity for the target molecule

e) Matrix material is "user friendly"

# 2. Applications of Immobilized Molecules

## 2.1. Drug Delivery Systems

Advanced drug delivery systems (ADDS) have found applications in many biomedical fields [29,30]**.** Drug delivery is a combination of material science, pharmaceutics and biology [31]. Adoption of different types of membranes in ADDS has made it possible to release drug in an optimal fashion according to the nature of a disease [32]. Examples of drug delivery systems include glucose-sensitive insulin and drug loaded magnetic nanoparticles.

### 2.1.1. Development of Glucose-Sensitive Insulin

The swelling or shrinking of smart hydrogel beads in response to small changes in pH or temperature can be used successfully to control drug release, because the diffusion of the drug out of the beads depends on the gel state [33].

Drug-delivery systems in which a drug is liberated in response to a chemical signal (*e.g.* ***insulin release in response to rising glucose concentration***) can be achieved using this system. The exposure of a glucose-sensitive insulin releasing system to glucose resulted in the oxidation of glucose to gluconic acid and thus a decrease in the pH, protonation and shrinking of the polymer, leading to an increased release of insulin. The polymer swells in size at normal body pH (pH = 7.4) and closes the gates. It shrinks at low pH (pH = 4) when the blood glucose level increases, thus opening the gates and releasing the insulin from the nanoparticles [34].

### 2.1.2. Drug Loaded Magnetic Nanoparticles

Nanotechnology offers the means to send the drugs to

 

targeted sites, and has the drug released in a controlled manner, which reduce side effects due to lower dosage and minimize or prevent drug degradation by using pathways other than gastrointestinal. Magnetic nanoparticles are recently applied in various fields such as MRI imaging, water treatment, hyperthermia and drug delivery systems. Drug loaded magnetic nanoparticles (DLMNP) have several advantages such as: small particle size; large surface area; magnetic response; biocompatibility and non-toxicity. DLMNP is introduced through injection and directed with external magnets to the right organ, which requires smaller dosage because of targeting, resulting in fewer side effects.

Recently, **Yu *et al.*, 2008** [35] reported a novel *In Vivo* strategy for combined cancer imaging and therapy by employing thermally cross-linked superparamagnetic iron oxide nanoparticles as a drug-delivery carrier. Whereas, **Kettering *et al.*, 2009** [36] used magnetic iron nanoparticles with cisplatin adsorbed in them for drug release in magnetic heating treatments for ***cancer***.

## 2.2. Enzyme-Linked Immunosorbent Assays (ELISA)

ELISA is a test used as a general screening tool for the detection of antibodies or antigens in a sample [37]. ELISA technology links a measurable enzyme to either an antigen or antibody. The procedure for detection of Ab in patient's sample as follows:

- Immobilize Ag on the solid support (well)
- Incubate with patient sample
- Add antibody-enzyme conjugate
- Amount of antibody-enzyme conjugate bound is proportional to amount of Ab in the sample
- Add substrate of enzyme
- Amount of color is proportional to amount of Ab in patient's sample.

However, ELISA technique in some cases is regarded as time consuming and it needs special equipment to run the assay (not portable). Thus many techniques have been developed to fasten the process such as that of **Xin *et al.*, 2009** [38], where he developed a chemiluminescence enzyme immunoassay using magnetic particles to monitor 17β-estradiol (E2) in environmental water samples. Another technique is using simple/rapid (S/R) test. The development of simple/rapid S/R tests has been extended from pregnancy detection of HIV antibodies in whole blood in addition to serum and plasma [39].

## 2.3. Antibiotics Production

Penicillins are the most widely used β-lactam antibiotics, with a share of about ***19 % of the estimated world-wide antibiotic market*** (**Table 3**) [8,27].

Production of antibiotics is one of the key areas in the field of applied microbiology. The conventional method of production is in stirred tank batch reactors. Since it is a no growth associated process, it is difficult to produce the antibiotic in continuous fermentations with free-cells. But it is a suitable case for cell immobilization, since growth and metabolic production can be uncoupled without affecting metabolite yields. Therefore, several attempts have been made to immobilize various microbial species on different supports matrices for antibiotic production. The most widely studied system is the production of penicillin G using immobilized cells of Penicillium *chrysogenum* [4]. In a recent study by Elnashar *et al.*, they were successful to covalently immobilize pencillin G acylase on carrageenan modified gels with retention of 100% activity after 20 reuses [9].

## 2.4. Medical Applications Particularly in Therapy

Medical applications of immobilized enzymes include diagnosis and treatment of diseases, among those enzyme replacement therapies, as well as artificial cells and organs, and coating of artificial materials for better biocompatibility [41]. Examples of potential medical uses of immobilized enzyme systems are listed below. For more applications, readers are encouraged to read the review article of **Soetan *et al.*, 2010** [42], where he reviewed the biochemical, biotechnological and other applications of enzymes.

- ***Asparaginase*** (3.5.1.1) for leukemia
- ***Arginase*** (3.5.3.1) for cancer
- ***Urease*** (3.5.1.5) for artificial kidney, uraemic disorders
- ***Glucose oxidase*** (1.1.3.4) for artificial pancreas
- ***Carbonate dehydratase*** (4.2.1.1) and catalase (1.11.1.6) for artificial lungs
- ***Glucoamylase*** (3.2.1.3) for glycogen storage disease
- ***Glucose-6-phosphate dehydrogenase*** (1.1.1.49) for glucose-6-phosphate dehydrogenase deficiency
- ***Xanthine oxidase*** (1.1.3.22) for Lesch–Nyhan disease
- ***Phenylalanine ammonia lyase*** (4.3.1.5) for phenylketonuria
- ***Urate oxidase*** (1.7.3.3) for hyperuricemia
- ***Heparinase*** (4.2.2.7) for extracorporeal therapy procedures

In addition to the above applications, we will focus the light on some important applications as solving the problem of lactose Intolerant people, production of fructose for diabetics and for people on diet regimen, and treatment of rheumatoid arthritis and joint diseases.

 

#### 2.4.1. Solving the Problem of Lactose Intolerant People

β-galactosidase is widely used in milk industries for hydrolysis of lactose to glucose and galactose. Lactose is the main carbohydrate contained in milk at a concentration between 5% and 10% (w/v) depending on the source of milk [43]. Lactose could also be found in whey permeate at higher concentrations. The consumption of foods with a high content of lactose is causing a medical problem for ***almost 70% of the world population***, especially in the developing countries, as the naturally present enzyme (β-galactosidase) in the human intestine, loses its activity during lifetime [44]. Undigested lactose in chyme retains fluid, bacterial fermentation of lactose results in production of gases, diarrhoea, bloating and abdominal cramps after consumption of milk and other dairy products.

Unfortunately, there is ***no cure to "lactose intolerance"***. This fact, together with the relatively low solubility and sweetness of lactose, has led to an increasing interest in the development of industrial processes to hydrolyze the lactose contained in dairy products (milk and whey) with both the free and immobilized conditions [45]. The studies have shown that glucose and galactose, the two monosaccharides hydrolosates of lactose (products hydrolyzed from lactose), are four times sweeter than lactose, more soluble, more digestible [46], and can be consumed by 'lactose intolerant' people. Interesting results of immobilized β-galactosidase on thermostable biopolymers of grafted carrageenan were obtained recently by **Elnashar and Yassin** [10,13].

#### 2.4.2. Fructose for Diabetics and for People on Diet Regimen

People on diet regimen and patients suffering from diabetes are highly recommended to consume fructose rather than any other sugar. Fructose can be produced from starch by enzymatic methods involving α-amylase, amyloglucosidase, and glucose isomerase, resulting in the production of a mixture consisting of oligosaccharides (8%), fructose (45%), and glucose (50%) [47]. However, separation of fructose from this high content fructose syrup is costly and thus makes this method uneconomical. In industries, inulinases are used to produce 95% of pure fructose after one step of the enzymatic hydrolysis of inulin. Industrial inulin hydrolysis is carried out at 60 °C to prevent microbial contamination and also because it permits the use of higher inulin substrate concentration due to increased solubility. **Elnashar *et al.*, 2009** and **Danial *et al.*, 2010**, have succeeded recently to produce a thermostable inulinolytic immobilized enzyme, which would be expected to play an important role in food and chemical industries, in which fructose syrup is widely applied [7,10].

#### 2.4.3. Treatment of Rheumatoid Arthritis and Joint Diseases

Superoxide dismutase (SOD) and catalase (CAT) have been encapsulated in biodegradable microspheres (MS) to obtain suitable sustained protein delivery [48]. A modified water/oil/water double emulsion method was used for poly (D,L-lactide-co-glycolide) (PLGA) and poly (D, L-lactide) PLA MS preparation co-encapsulating mannitol, trehalose, and PEG400 for protein stabilization. SOD release from PLGA MS may be potentially useful for long-term sustained release of the enzyme for the treatment of rheumatoid arthritis or other intra-ar- ticular and joint diseases (inflammatory manifestation).

### 2.5. Non Medical Applications of Immobilized Enzymes

#### 2.5.1. Treatment of Pesticide-Contaminated Waste

Application of pesticide in agriculture serves to lower the cost of production, increase crop yields, provide better quality produce and also reduce soil erosion. Although pesticides are toxic and have adverse effect on human health and the environment, their use is inevitable in many cases as an effective means of controlling weeds, insect, and fungus, parasitic and rodent pests. One of the most important technologies to be applied for this approach is immobilized enzyme. The immobilized enzyme is capable of breaking down a range of pesticide-contaminated waste as organophosphate insecticides [49,50].

#### 2.5.2. Neutralizing Dangerous Chemical Gases or Vapors

The use of immobilized enzymes in the national security arena has shown to be promising. For example, they could include infiltrating items such as air filters, masks, clothing, or bandages with the concentrated immobilized enzymes to neutralize dangerous chemical gases or vapors [51].

### 2.6. Purification of Proteins

Protein purification is an important objective in industrial enzymes in order to increase the enzyme's specific activity and to obtain an enzyme in its pure form for a specific goal. Affinity ligands is the most used technique for purification of target molecules as it can reduce the number of chromatographic steps in purification procedures to one or two steps. Immobilization of affinity ligands to an insoluble support can be a powerful tool in isolation of particular substances (e.g. protein) from a complex mixture of proteins. Some examples of affinity ligands are immobilized carbohydrate-binding proteins and immobilized metal ions. Another technique for protein purifica-

 

tion is using Electric field gradient focusing (EFGF). For more information on the principles and methods of protein purification, readers should refer to the **"Handbook: Purifying challenging proteins: principles and methods" in 2007** [52].

#### 2.6.1. Immobilized Carbohydrates-Binding Proteins

Purification of proteins could be performed using immobilized carbohydrates such as mannose, lactose and melibiose. For example, immobilized lactose on sepharose 4B™ will be selective for purification of lactase from a mixture of other proteins. More information on this technique can be found in the book of **Hermanson *et al.*, 1992** "Immobilized affinity ligand techniques" [53].

#### 2.6.2. Electric Field Gradient Focusing (EFGF)

Electric field gradient focusing is a member of the family of equilibrium gradient focusing techniques (e.g gel electrophoresis). It depends on an electric field gradient and a counter-flow to focus, concentrate and separate charged analytes, such as peptides and proteins. Since analytes with different electrophoretic mobilities have unique equilibrium positions, EFGF separates analytes according to their electrophoretic mobilities, similar to the way isoelectric focusing (IEF: electrophoresis is a pH gradient where the cathode is at a higher pH value than the anode) separates analytes according to isoelectric points. The constant counter flow is opposite to the electrophoretic force that drives the analytes. When the electrophoretic velocity of a particular analyte is equal and opposite to the velocity of the counter flow, the analyte is focused in a narrow band because at this position the net force on it is zero.

However, EFGF avoids protein precipitation that often occurs in IEF when proteins reach their isoelectric points and, therefore, can be applied to a broad range of proteins. **Sun (2009)** [54] in his Ph.D. thesis demonstrated that protein concentration exceeding 10,000-fold could be concentrated using such devices.

### 2.7. Extraction of Biomolecules Using Magnetic Particles

The traditional methods for biomolecules purification such as centrifugation, filtration, and chromatography can today be replaced by the use of magnetic particles. They are reactive supports for biomolecules capturing. Their use is simple, fast, and efficient for the extraction and purification of biomolecules. In the biomedical Weld, numerous publications deal with the use of magnetic particles for biomolecule extraction [55], cell sorting [56], and drug delivery [57]. Magnetic beads are widely used in molecular biology [58], medical diagnosis [59], and medical therapy [55].

The major application concerns the extraction of biomolecules such as proteins [60], antibodies, and nucleic acids [61]. Magnetic beads carrying antibodies are also used for specific bacteria [55] and virus captures [58]. **Krupey in 1994** [62] patented a method for virus capture process. The method was based on interactions between viruses and anionic polymers, leading to the precipitation of complexes by charge neutralization. After the capture step, viruses were extracted by centrifugation. At the current time, to our knowledge, only one method using magnetic beads has been published recently [63]. In these studies, some DNA and RNA viruses were concentrated more than 100 and 1000 times, respectively, using polyethyleneimine (PEI)1-conjugated magnetic beads.

### 2.8. Heavy Metals Removal

Heavy metal pollution is an environmental problem of worldwide concern. Several industrial wastewater streams may contain heavy metals such as; Pb, Cr, Cd, Ni, Zn, As, Hg, Cu, Ag. Traditionally, precipitation, solvent extraction, ion-exchange separation and solid phase extraction are the most widely used techniques to eliminate the matrix interference and to concentrate the metal ions. Many materials have been used to remove them such as sorbents [64] (e.g. silica, chitosan, sponge, etc) and biosorbents (e.g. immobilized algae) [65].

**Biosorbents**: can be defined as the selective sequestering of metal soluble species that result in the immobilization of the metals by microbial cells such as cyanobacteria. It is the physicochemical mechanisms of inactive (*i.e.* non-metabolic) metal uptake by microbial biomass. Metal sequestering by different parts of the cell can occur via various processes: complexation, chelation, coordination, ion exchange, precipitation, reduction. Size of immobilized bead for metals removal is a crucial factor for use of immobilized biomass in bio-sorption process. It is recommended that beads should be in the size range between 0.7 and 1.5 mm, corresponding to the size of commercial resins meant for removing metal ions. **Abdel Hameed and Ebrahim, 2007** [63] in their review article, has revealed some of the immobilized algae on different matrices that have potential in heavy metals removal due to its high uptake capacity and abundance**.**

### 2.9. Production of Biosensors

Biosensors are chemical sensors in which the recognition system utilizes a biochemical mechanism [66]**.** A biosensor is a sensing device made up of a combination of a specific biological element and a transducer. The "specific biological element" such as antibodies [67]**,** enzymes [68], bacteria [69,70] and DNA [71] recognizes a specific analyte such as pollutions (toxicity caused by pesticides, phenols, mercury, arsenic, etc) and the changes in the biomolecules are usually converted into

 

electrical signal (which is in turn calibrated to a certain scale) by a transducer.

### 2.10. Production of Biodiesel

The idea of using biodiesel as a source of energy is not new [72], but it is now being taken seriously because of the escalating price of petroleum and, more significantly, the depletion of fossil fuels (oil and gas) within the next 35 years and the emerging concern about global warming that is associated with burning fossil fuels [73]. Biodiesel is much more environmentally friendly than burning fossil fuels, to the extent that governments may be moving towards making biofuels mandatory [74]. The global market survey of biodiesel has shown a tremendous increase in its production**.**

Biodiesel is made by chemical combination of any natural oil or fat with an alcohol such as methanol and a catalyst (e.g. lipases) for the transesterification process. Transesterification is catalyzed by acids, alkalis [75] and lipase enzymes [76]. Use of lipases offers important advantages as it is more efficient, highly selective, involves less energy consumption (reactions can be carried out in mild conditions), and produces less side products or waste (*environmentally favorable*). However, it is not currently feasible because of the *relatively high cost of the catalyst* [77].

On the industrial level, a number of methods for the immobilization of lipases on solid supports have been reported [78]. Commercially available lipases are supplied both as lyophilised powders, which contain other components in addition to the lipase [79]. The immobilized lipases most frequently used for biodiesel production are lipase B from *Candida Antarctica* [80]. This is supplied by Novozymes under the commercial name ***Novozym 435*®** (previously called SP435) and is immobilized on an acrylic resin. The *Mucor miehei* commercial lipase (Lipozyme IM60 – Novozym) immobilized on a macroporous anionic exchange resin has also been extensively used for the same purpose [81].

### 2.11. Life Detection and Planetary Exploration

Analytical techniques based on mass spectrometry have been traditionally used in space science. Planetary exploration requires the development of miniaturized apparatus for in situ life detection. Recently, a new approach is gaining acceptance in the space science community: the application of the well-known, highly specific, antibody–antigen affinity interaction for the detection and identification of organics and biochemical compounds. Antibody microarray technology allows scientists to look for the presence of thousands of different compounds in a single assay and in just one square centimeter. The detection of organic molecules of unambiguous biological origin is fundamental for the confirmation of present or past life.

Preservation of biomarkers on the antibody stability under space environments, smaller biomolecules, such as amino acids, purines, and fatty acids, are excellent biomarkers in the search for ***life on Mars***, but they may be much less resistant to oxidative degradation. Recent work by **Kminek and Bada, 2006** [82] showed that amino acids can be protected from radiolysis decomposition as long as they are shielded adequately from space radiation. They estimated that it is necessary to drill to a depth of 1.5 to 2 m to detect the amino acid signature of life that became extinct about ***three billion years ago***. A microfabricated capillary [83] electrophoresis device (kind of new immobilization technology) for amino acid chirality determination was developed for extraterrestrial exploration [84]. Recently, antibody microarray, a new immobilization technology that kept the stability of antibody under space environment allowed it to be applied for planetary exploration Exomars mission [85].

## 3. Recent Advances in Supports and Technologies used in Enzyme Immobilization

In the search for suitable supports for enzyme immobilization, it was found that physical and chemical properties (e.g. pore size, hydrophilic/hydrophobic balance, aquaphilicity and surface chemistry) of support could exert effect on enzyme immobilization and its catalytic properties [86]. Thus there was a need for new immobilization techniques/supports to avoid such shortcomings [19]. The following are some examples of the recent carriers and technologies used for enzyme immobilization.

### 3.1. New Carriers Used in Immobilization

#### 3.1.1. New Carriers Used in Immobilization

Over the last few years, mesoporous support such as silica and silicates having pore size of 2–50 nm has been developed and being considered as one of the most promising carriers for enzyme immobilization [87-91]. The exploitation of novel carriers that enable high enzyme loading and activity retention has become the focus of recent attention [92]. The large surface areas and greater pore volumes of these materials could enhance the loading capacity of an enzyme and the large pores in the support facilitate transport of substrate and product [93].

Functional mesoporous material resulted in exceptionally high immobilization efficiency with enhanced stability, while conventional approaches yielded far lower immobilization efficiency [94]. Additionally, the increase in the thermal stability of immobilized enzyme indicated that *protein inside a confined space could be stabilized by some folding forces* which did not exist in proteins in

 

bulk solutions [95]. Confinement of the support nanopore could be similar to the macromolecular crowding [96], and could also stabilize the enzyme at high temperature.

Nanoporous gold [97] and nanotube [98,99] have also been used to immobilize enzymes. Most of the obtained immobilized enzymes were used in the electrode preparation and biosensor applications. The modified porous gold electrode shows an overall increased signal, and therefore a better detection limit and higher sensitivity when used as sensors.

#### 3.1.2. Magnetic Hybrid Support

The use of magnetic supports for enzyme immobilization enables a rapid separation in an easily stabilized fluidized bed reactor for continuous operation of enzyme. It can also reduce the capital and operation costs [100]. Due to the functionalization [101] of enzyme and its suitable microenvironment, magnetic materials were often embedded in organic polymer or inorganic silica to form hybrid support [102]. Recently, because of the low enzyme loading on the conventional magnetic beads, further attention was paid to the magnetic mesoporous support [103]. Magnetite mesoporous silica hybrid support was fabricated by the incorporation of magnetite to the hollow mesoporous silica shells, which resulted in the perfect combination of mesoporous materials properties with magnetic property. The produced hybrid support has shown to improve the enzyme immobilization [104].

### 3.2. New Technologies for Enzyme Immobilization

#### 3.2.1. Single Enzyme Nanoparticles

In the field of industrial enzymes, there is a great research for improving the enzyme stability under harsh conditions. As an innovative way of enzyme stabilization, "single-enzyme nanoparticles (SENs)" technology was rather attractive because enzymes in the nanoparticle exhibited very good stability under harsh conditions [107] have developed armored SENs that surround each enzyme molecule with a porous composite organic/ inorganic network of less than a few nanometers thick. They significantly stabilized chymotrypsin and trypsin and the protective covering around chymotrypsin is so thin and porous that a large mass transfer limitation on the substrate could not take place.

**Yan *et al.* (2006)** [106] provided a simple method that yields a single enzyme capsule with enhanced stability, high activity and uniformed size. The 2-step procedure including surface acryloylation and in situ aqueous polymerization to encapsulate a single enzyme in nanogel to provide robust enzymes for industrial biocatalysis. The immobilized horseradish peroxidase (HRP) exhibited similar biocatalytic behavior (Km and kcat) to the free enzyme. However, the immobilization process significantly improved the enzyme\s stability at high temperature in the presence of polar organic solvent.

#### 3.2.2. Enzymatic Immobilization of Enzyme

The use of green chemistry rather than using harsh chemicals is one of the main goals in enzyme industries to avoid the partial denaturation of enzyme protein. An emerging and novel technology is to fabricate solid protein formulations [108,109]. As model proteins, enhanced green fluorescent protein (EGFP) and glutathione S-transferase (GST) were tagged with a neutral Gln-donor substrate peptide for MTG (Leu-Leu-Gln-Gly, LLQG-tag) at their C-terminus and immobilized onto the casein-coated polystyrene surface [108].

Luciferase (Luc) and glutathione-S-transferase (GST) ybbR-fusion proteins were immobilized onto PEGA resin retaining high levels of enzyme activity using phosphopantetheinyl transferase (Sfp) mediating site-specific covalent immobilization [109]. In general, the Sfp-catalyzed surface ligation is mild, quantitative and rapid, occurring in a single step without prior chemical modification of the target protein.

#### 3.2.3. Microwave Irradiation

The use of porous supports for immobilization of enzymes is difficult to distribute because of diffusion limitations [110] and they often remain only on external channel [111]. For enzymes having large dimensions, such as penicillin acylase (PA), the mass transfer is even slower. The immobilization of such enzyme to porous materials can prove tedious using conventional techniques [112].

**Wang *et al.*, 2008b & 2009a** [95,113] have recently succeeded to immobilize papain and PA using the adsorption technique into the mesocellular siliceous foams (MCFs) using microwave irradiation technology. Reaction time of 80 and 140 s were enough for papain and PA to attach on the wall of MCFs, respectively. The activities of papain and penicillin acylase immobilized with microwave-assisted method were 779.6 and 141.8 U/mg, respectively. In another experiment, macromolecules crowding was combined with small molecular quenching to perfect microwave-assisted covalent immobilization [113].

#### 3.2.4. Photoimmobilization Technology

In the field of ***immobilization of biomolecules***, potential applications of photoimmobilization using nitrene groups could take place. Nitrene groups have a property of insertion into C-H bond. When photoreactive polymer and horseradish peroxidase or glucose oxidase are exposed to ultraviolet (UV) light at 365 nm, the reactive nitrene immobilizes the protein molecules in 10 to 20 min

 

through covalent bonding [114]. Horseradish peroxidase (HRP) and glucose oxidase (GOD) have been immobilized onto the photoreactive cellulose membrane by the ultraviolet and sunlight [115]. They found that sunlight intensity required for optimum immobilization was 21,625 lux beyond which no appreciable increase in immobilization was observed. Moreover, sunlight exposure gave better immobilization compared to 365 nm UV light.

#### 3.2.5. Ionic Liquids

Ionic liquids, the green solvents for the future, are composed entirely of ions and they are salts in the liquid state. In the patent and academic literature, the term "ionic liquid" now refers to liquids composed entirely of ions that are fluid around or below 100°C (e.g. ethanolamine nitrate, m.p. 52-55$^{o}$C). The date of discovery of the "first" ionic liquid is disputed, along with the identity of the discoverer. Room-temperature ionic liquids are frequently colorless, fluid and easy to handle [116].

Versatile biphasic systems could be formed by controlling the aqueous miscibility of ionic liquid [117]. Based on a biphasic catalytic system where the enzyme is immobilized into an ionic liquid (IL), Mecerreyes and co-workers [118] have reported a new method which allows recycling and re-using of the HRP enzyme in the biocatalytic synthesis of PANI. The HRP enzyme was dissolved into the IL 1-butyl-3-methylimidazolium hexafluorophosphate and the IL/HRP phase acts as an efficient biocatalyst and can be easily recycled and reused several times. Due to the immiscibility between the IL and water, the immobilized HRP could be simply recovered by liquid/ liquid phase separation after the biocatalytic reaction [119,120]. Although this new method is faster and easier than the classical immobilization of HRP into solid supports, it would not be widely applied to the industrial production in the coming future because of the ionic liquids' expenses.

## 4. Recommendation for the Future of Immobilization Technology

At present, a vast number of methods of immobilization are currently available. Unfortunately, there is no a universal enzyme support, *i.e.* the best method of immobilization might differ from enzyme to enzyme, from application to application and from carrier to carrier. Accordingly, the approaches currently used to design robust industrial immobilized enzymes are, without exception, labeled as "irrational", because they often result from screening of several immobilized enzymes and are not designed. As a consequence, some of the industrial enzymes are working below their optimum conditions.

Recently, **Cao L. (2005)** [5] in his book "Carrier bound immobilized enzymes" tackled this problem as he surmised that the major problem in enzyme immobilization is not only the selection of the right carrier for the enzyme immobilization but it is how to design the performance of the immobilized enzyme.

The ***author of this review article*** is suggesting from his point of view as he is working in that field for the last ten years to follow these steps in order to get to this goal in the shortest time:

1- build a ***data base*** containing all information on the available biomolecules (enzymes, antibodies, etc) and carriers (organic, inorganic, magnetic hybrid, ionic liquids, etc) then

2- use the dry lab (***bioinformatics***) to validate the probability of success and the efficiency of the immobilization process then

3- starting the experiment in the ***wet lab***.

The author believes that if this strategy could be performed, we should expect immobilized molecules working at their optimum conditions, with higher stability and efficiency, which will save money, time and effort for the prosperity of human being.

## 5. Acknowledgement

The author would like to thank the Centre of Excellence for Advanced Sciences, NRC, Egypt, the Research and Development Innovation (RDI) program and the Science and Technology Development Fund STDF/IMC for supporting this work, and highly appreciates the efforts of Mrs Joanne Yachou for her contribution towards editing.

## REFERENCES

[1] H. Buyukgungor and L. Gurel, "The Role of Biotechnology on the Treatment of Wastes," *African Journal of Biotechnology*, Vol. 8, No. 25, 2009, pp. 72537262.

[2] Z. T. Yu-Qung, S. Mei-Lin, Z. Wei-De, D. Yu-Zhen, M. Yue and Z. Wen-Ling, "Immobilization of L-Asparaginase of the Microparticles of the Natural Silk Serum Protein and Its Characters," *Biomaterials*, Vol. 25, No. 17, 2003, pp. 3151-3759.

[3] K. Kierek-Pearson and E. Karatan, "Biofilm Development in Bacteria," *Advances in Applied Microbiology*, Vol. 57, 2005, pp. 79-111.

[4] B. Carpentier and O. Cerf, "Biofilms and Their Consequences, with Particular Reference to Hygiene in the Food Industry," *Journal of Applied Bacteriology*, Vol. 75, No. 6, 1993, pp. 499-511.

[5] L. Cao and R. D. Schmid, "Carrier-Bound Immobilized Enzymes: Principles, Application and Design," WILEY-VCH Verlag GmbH & Co, Weinheim, 2005.

[6] M. Ayala and E. Torres, "Enzymatic Activation of Alkanes: Constraints and Prospective," *Applied Catalysis A: General*, Vol. 272, No. 1-2, 2004, pp. 1-13.

 

[7] E. N. Danial, M. M. Elnashar and G. E. Awad, "Immobilized Inulinase on Grafted Alginate Beads Prepared by the One-Step and the Two-Steps Methods Indus," *Chemical Engineering Research*, Vol. 49, No. 7, 2010, pp. 3120-3125.

[8] M. M. Elnashar, "Chapter in a Book Entitled "Low-cost Foods and Drugs Using Immobilized Enzymes on Biopolymers," *Book entitled Biopolymers*, published by www.sciyo.com (In Press), 2010.

[9] M. M. Elnashar, A. M. Yassin and T. Kahil, "Novel Thermally and Mechanically Stable Hydrogel for Enzyme Immobilization of Penicillin G Acylase Via Covalent Technique," *Journal of Applied Polymer Science*, Vol. 109, No. 6, 2008, pp. 4105-4111.

[10] M. M. Elnashar, E. N. Danial and G. E. Awad, "Novel Carrier of Grafted Alginate for Covalent Immobilization of Inulinase," *Industrial & Engineering Chemistry Research*, Vol. 48, 2009, No. 22, pp. 9781-9785.

[11] M. M. Elnashar, A. M. Yassin, A. A. Abdel Moneim and E. M. Abdel Bary, "Surprising Performance of Alginate Beads for the Release of Low Molecular Weight Drugs," *Journal of Applied Polymer Science*, Vol. 116, No. 5, 2010, pp. 3021-3126.

[12] M. M. Elnashar and A. M. Yassin, "Covalent Immobilization of B-Galactosidase on Carrageenan Coated Chitosan". *Journal of Applied Polymer Science*, Vol. 114, No. 1, 2009a, pp. 17-24.

[13] M. M. Elnashar and A. M. Yassin, "Lactose Hydrolysis by β-Galactosidase Covalently Immobilized to Thermally Stable Biopolymers," *Applied Biochemistry and Biotechnology*, Vol. 159, No. 2, 2009b, pp. 426-437.

[14] M. E. Mansour, M. M. Elnashar and M. E. Hazem, "Amphoteric Hydrogels Using Template Polymerization Technique," *Journal of Applied Polymer Science*, Vol. 106, No. 6, 2007, pp. 3571-3580.

[15] B. Katzbauer, M. Narodoslawsky, A. Moser, "Classification System for Immobilization Techniques," *BioProcess Engineering*, Vol. 12, No. 4, 1995, pp. 173-179.

[16] T. Tosa, T. Mori, N. Fuse and I. Chibata, "Studies on Continuous Enzyme Reactions Part V Kinetics and Industrial Application of Aminoacylase Column for Continuous Optical Resolution of Acyl-*Dl* Amino Acids," *Biotechnology and Bioengineering*, Vol. 9, No. 4, 1967, pp. 603-615.

[17] B. Menaa, C. Torres, M. Herrero, V. Rives, A. R. W. Gilbert and D. K. Eggers, "Protein Adsorption to Organically-Modified Silica Glass Leads to a Different Structure Than Sol-Gel Encapsulation," *Biophysical Journal*, Vol. 95, No. 8, 2008a, pp. 51-53.

[18] S. Çetinus, E. Sahin and D. Saraydin, "Preparation of Cu(II) Adsorbed Chitosan Beads for Catalase Immobilization," *Food Chemistry*, Vol. 114, No. 3, 2009, pp. 962-969.

[19] T. Xie, A. Wang, L. Huang, H. Li, Z. Chen, Q. Wang and X. Yin, "Review: Recent Advance in the Support and Technology Used in Enzyme Immobilization," *African Journal of Biotechnology*, Vol. 8, No. 19, 2009, pp. 4724-4733.

[20] G. F. Bickerstaff, "Impact of Genetic Technology on Enzyme Technology," *Biotechnology & Genetic Engineering Reviews*, Vol. 15, No. 1, 1995, pp. 13-30.

[21] A. Riaz, S. Qader, A. Anwar and S. Iqbal, "Immobilization of a Thermostable á-amylase on Calcium Alginate Beads from Bacillus Subtilis KIBGE-HAR," *Australian Journal of Basic and Applied Sciences*, Vol. 3, 2009, p. 2883.

[22] A. Groboillot, D. K. Boadi, D. Poncelot and R. J. Neufled, "Immobilization of Cells for Application in the Food Industry," *Critical Reviews in Biotechnology*, Vol. 14, No. 2, 1994, pp. 75-107.

[23] J. S. Patil, M. V. Kamalapur, S. C. Marapur and D. V. Kadam, "Ionotropic Gelation and Polyelectrolyte Complexation: The Novel Techniques to Design Hydrogel Particulate Sustained, Modulated Drug Delivery System: A Review," *Digest J. Nanomat. Biostruct*, Vol. 5, 2010, p. 241.

[24] B. Menaa, M. Herrero, V. Rives, M. Lavrenko and D. K. Eggers, "Favorable Influence of Hydrophobic Surfaces on Protein Structure in Porous Organically-Modified Silica Glasses," *Biomaterials*, Vol. 29, No. 18, 2008b, pp. 2710-2718.

[25] B. Menaa, Y. Miyagawa, M. Takahashi, M. Herrero, V. Rives, F. Menaa and D. K. Eggers, "Bioencapsulation of Apomyoglobin in Nanoporous Organosilica Sol-Gel Glasses: Influence of the Siloxane Network on the Conformation and Stability of a Model Protein," *Biopolymers*, Vol. 91, No. 11, 2009, pp. 895-906.

[26] B. Menaa, F. Menaa, C. Aiolfi-Guimaraes and O. Sharts, "Silica-Based Nanoporous Sol-Gel Glasses: From Bioencapsulation to Protein Folding Studies," *International Journal of Nanotechnology*, Vol. 7, No. 1, 2010, pp. 1-45.

[27] M. M. Elnashar, "Development of a Novel Matrix for the Immobilization of Enzymes for Biotechnology," Leeds University, UK, 2005.

[28] M. M. Elnashar, P. A. Millner, A. F. Johnson and T. D. Gibson, "Parallel Plate Equipment for Preparation of Uniform Gel Sheets," *Biotechnology Letters*, Vol. 27, No. 10, 2005, pp. 737-739.

[29] C. C. Lin and A. T. Metters, "Hydrogels in Controlled Release Formulations: Network Design and Mathematical Modeling," *Advanced Drug Delivery Reviews*, Vol. 58, No. 12-13, 2006, pp. 1379-1408.

[30] E. J. Pollauf and D. W. Pack, "Use of Thermodynamic Parameters for Design of Double-Walled Microsphere Fabrication Methods," *Biomaterials*, Vol. 27, No. 14, 2006, pp. 2898-2906.

[31] D. W. Pack, A. S. Hoffman, S. Pun and P. S. Stayton, "Design and Development of Polymers for Gene Delivery," *Nature Reviews Drug Discovery*, Vol. 4, 2005, pp. 581-593.

[32] A. C. R. Grayson, I. S. Choi, B. M. Tyler, P. P. Wang and B. H. Michael, "Multi-Pulse Drug Delivery from a Resorbable Polymeric Microchip Device," *Nature Materials journal Cima*, Vol. 2, No. 11, 2003, pp. 767-772.

 

[33] Y. H. Kim, I. C. Kwon, Y. H. Bae and S. W. Kim, "Saccharide Effect on the Cloud Point of Thermosensitive Polymers," *Macromolecules*, Vol. 28, No. 4, 1995, pp. 939-944.

[34] P. Sona, "Nanoparticulate Drug Delivery Systems for the Treatment of Diabetes," *Digest J. Nanomat. Biostruct*, Vol. 5, No. 2, 2010, pp. 411-418.

[35] M. Yu, Y. Jeong, J. Park, S. Park, J. Kim, J. Min, K. Kim and S. Jon, "Drug-Loaded Superparamagnetic Iron Oxide Nanoparticles for Combined Cancer Imaging and Therapy *in vivo*," *Angewandte Chemie International Edition*, Vol. 47, No. 29, 2008, pp. 5362-5365.

[36] M. Kettering, H. Zorn, S. Bremer-Streck, H. Oehring, M. Zeisberger, C. Bergemann, R. Hergt, J. Halbhuber, A. Kaiser and I. Hilger, "Characterization of Iron Oxide Nanoparticles Adsorbed with Cisplatin for Biomedical Applications," *Physics in Medicine and Biology*, Vol. 54, 2009, pp. 5109-5121.

[37] M. Farre, M. Kuster, R. Brix, F. Rubio, M.-J. L. d. Alda and D. Barcelo, "Comparative Study of an Estradiol Enzyme-Linked Immunosorbent Assay Kit, Liquid Chromatography-Tandem Mass Spectrometry, and Ultra Performance Liquid Chromatography-Quadrupole Time of Flight Mass Spectrometry for Part-Per-Trillion Analysis of Estrogens in Water Samples," *The Journal of Chromatography A*, Vol. 1160, No. 1-2, 2007, pp. 166-175.

[38] T. Xin, X. Wang, H. Jin, S. Liang, J. Lin and Z. Li, "Development of Magnetic Particle-Based Chemiluminescence Enzyme Immunoassay for the Detection of 17β-Estradiol in Environmental Water," *Applied Biochemistry and Biotechnology*, Vol. 158, No. 3, 2009, pp. 582-594.

[39] World Health Organization (WHO), "HIV Simple/Rapid Assays: Operational Characteristics (Phase I)," 2002, http://www.who.int/3by5/en/simplerapidassays.pdf

[40] M. Ogaki, K. Sonomoto, H. Nakajima and A. Tanaka, "Continuous Production of Oxytetracycline by Immobilized Growing *Streptomyces Rimosus* Cells," *Applied Microbiology and Biotechnology*, Vol. 24, 1986, pp. 6-11.

[41] A. K. Piskin, "Therapeutic Potential of Immobilized Enzymes," *NATO ASI Series, Series E*, Vol. 252, 1993, p. 191.

[42] K. Soetan, O. Aiyelaagbe and C. Olaiya, "Review of the Biochemical, Biotechnological and Other Applications of Enzymes," *African Journal of Biotechnology*, Vol. 9, No. 4, 2010, pp. 382-393.

[43] J. A. Ordoñez, M. A. Cambero, L. Fernandez, M. L. Garcia, G. Garcia and L. Hoz, "Componentes de los Alimentos y procesos. Tecnologia de los Alimentos," Editorial Sintesis, Madrid, Spain, 1998.

[44] M. Richmond, J. Gray and C. Stine, "Beta-galactosidase: Review of Recent Research Related to Technological Application, Nutritional Concerns, and Immobilization," *The Journal of Dairy Science*, Vol. 1759, 1981, p. 64.

[45] J. H. German, "Applied Enzymology of Lactose Hydrolysis," *In Milk Powders for the Future*, p. 81.

[46] S. Sungur and U. Akbulut, "Immobilization of β-galactosidase onto Gelatin by Glutaraldehyde and Chromium (III) Acetate," *Journal of Chemical Technology & Biotechnology*, (*Oxford, Oxfordshire*) Vol. 59, No. 3, 1994, pp. 303-306.

[47] P. Gill, R. Manhas and P. Singh, "Hydrolysis of Inulin by Immobilized Thermostable Extracellular Exoinulinase from Aspergillus *Fumigatus*," *Journal of Food Engineering*, Vol. 76, No. 3, 2006, pp. 369-375.

[48] S. Giovagnoli, "Biodegradable Micropheres as Carriers for Native Superoxide Dismutase and Catalase Delivery," *AAPS Pharmaceutical Science Technology*, Vol. 5, No. 4, 2004, p. 51.

[49] I. Horne, T. D. Sutherland, R. L. Harcourt, R. J. Russell and J. G. Oakeshott, "Identification of an (Organophosphate Degradation) Gene in an Agrobacterium Isolate," *Applied and Environmental Microbiology*, Vol. 68, No. 7, 2002, pp. 3371-3376.

[50] F. Sharmin, S. Rakshit, H. Jayasuriya, "Enzyme Mmobilization on Glass Surfaces for the Development of Phosphate Detection Biosensors," *Agricultural Engineering International: the CIGR Ejournal. Manuscript FP* 06 019, Vol. IX. April 2007.

[51] E. Ackerman and C. Lei, "Immobilizing Enzymes for Useful Service," 2008, http//www.google

[52] Hand book from GE Healthcare, "Purifying Challenging Proteins: Principles and Methods," General Electric Co, USA, 2007.

[53] G. Hermanson, A. Mallia and P. Smith, "Immobilized Affinity Ligand Techniques," Academic Press Incorporation, New York, 1992.

[54] X. Sun, "Polymeric Microfluidic Devices for Bioanalysis," Brigham Young University, China, 2009.

[55] T. Delair and F. Meunier, "Amino-Containing Cationic Latex Oligo-Conjugates: Application to Diagnostic Test Sensitivity Enhancement," *Colloids and Surface*, Vol. 153, No. 1-3, 1999, pp. 341-353.

[56] J. T. Kemshead, J. G. Treleaven, F. M. Gibson, J. Ugallstad, A. Rembaum and T. Philip, "Removal of Malignant Cells from Marrow Using Magnetic Microspheres And Monoclonal Antibodies," *Progress in Experimental Tumor Research*, Vol. 29, 1985, pp. 249-245.

[57] R. Langer, "New methods of drug delivery," *Science*, Vol. 249, No. 4976, 1990, pp. 1527-1533.

[58] J. D. Andreadis and L. A. Chrisey, "Use of Immobilized Pcr Primer to Generate Covalently Immobilized Dnas for *In Vitro* Transcription/Translation Reaction," *Nucleic Acids Research*, Vol. 28, No. 2, 2000, p. e5.

[59] M. Myrmel, E. Rimstad and Y. Wasteson, "IMS of Norwalk-like Virus (Geno Group I) in Artificially Contaminated Environmental Water Samples," *International Journal of Food Microbiology*, Vol. 62, No. 1-2, 2000, pp. 17-26.

[60] X. Ding and Y. Jiang, "Adsorption/Desorption of Protein on Magnetic Particles Covered by Thermosensitive Polymers," *Journal of Applied Polymer Science*, Vol. 278, 2000, p. 459.

 

[61] S. Rouquier, B. J. Tracks, "Direct Selection of cDNAs Using Whole Chromosomes," Nucleic Acids Research, Vol. 23, No. 21, 1995, pp. 4415-4420.

[62] J. Krupey, "Water Insoluble Cross-Linked Acid Composition," *United States Patent*, Vol. 5, No. 294, 1994, p. 681.

[63] A. Ifiata, K. Satoh, M. Murata, M. Hikata, T. Hayakawa and T. Yamaguchi, "Virus Concentration Using Sulfonated Magnetic Beads to Improve Sensitivity in Nucleic Acid Amplification Tests," *Biological and Pharmaceutical Bulletin*, Vol. 26, No. 8, 2003, pp. 1065-1069.

[64] H. M. Abdel and O. Ebrahim, "Review: Biotechnological Potential Uses of Immobilized Algae," *International Journal of Agriculture and Biology*, Vol. 9, 2007, p. 183.

[65] K. Shareef, "Sorbents for Contaminents Uptake from Aqueous Solutions," *Part* 1 *Heavy Metals. World Journal of Agriculture Science*, Vol. 5, 2009, p. 819.

[66] C. Jianrong, M. Yuqing, H. Nongyue, W. Xiaohua and L. Sijiao, "Nanotechnology and Biosensors," *Biotechnology Advance*, Vol. 22, No. 7, 2004, pp. 505-518.

[67] S. Rodriguez-Mozaz, S. Reder, M. J. Lopez de Alda, G. Gauglitz and D. Barcelo, "Simultaneous Multi-Analyte Determination of Estrone, Isoproturon and Atrazine in Natural Waters by the River Analyser (Riana), an Optical Immunosensor," *Biosensors and Bioelectronics*, Vol. 19, No. 7, 2004, pp. 633-640.

[68] C. Nistor, A. Rose, M. Farre, L. Stocia, U. Wollenberger, T. Ruzgas, D. Pfeiffer, D. Barcelo, L. Gorton and J. Emneus, "In-Field Monitoring of Cleaning Efficiency in Waste Water Treatment Plants Using Two Phenol-Sensitive Biosensors," *Analytica Chimica Acta*, Vol. 456, No, 1, 2002, pp. 3-17.

[69] J. C. Philp, S. Balmand, E. Hajto, M. J. Bailey, S. Wiles, A. S. Whiteley, A. K. Lilley, J. Hajto and S. A. Dunbar, "Whole Cell Immobilized Biosensors for Toxicity Assessment of a Wastewater Treatment Plant Treating Phenolics-Containing Waste," *Analytica Chimica Acta*, Vol. 487, No. 1, 2003, pp. 61-74.

[70] T. Petanen and M. Romantschuk, "Use of Bioluminescent Bacterial Biosensors as an Alternative Method for Measuring Heavy Metals in Soil Extracts," *Analytica Chimica Acta*, Vol. 456, No. 1, 2002, pp. 55-61.

[71] G. Marrazza, I. Chianella and M. Mascini, "Disposable DNA Electrochemical Biosensors for Environmental Monitoring," *Analytica Chimica Acta*, Vol. 387, No. 3, 1999, pp. 297-307.

[72] S. Sawayama, S. Inoue, Y. Dote and S. Y. Yokoyama, "$CO_2$ Fixation and Oil Production through Microalga," *Energy Conversion and Management*, Vol. 36, No. 6-9, 1995, pp. 729-731.

[73] M. Gavrilescu and Y. Chisti, "Biotechnology: A Sustainable Alternative for Chemical Industry," *Biotechnology Advance*, Vol. 23, No. 7-8, 2005, pp. 471-499.

[74] "Biodiesel: Biodiesel Review," 2006. http://www.sipef.be/pdf/biodiesel_presentation.pdf

[75] L. C. Meher, D. V. Sagar, S. N. Naik, "Technical Aspects of Biodiesel Production by Transesterification—A Review," *Ren. Sustain. Energ. Rev*, Vol. 10, No. 3, 2006, pp. 248- 268.

[76] R. Sharma, Y. Chisti and U. C. Banerjee, "Production, Purification, Characterization, and Applications of Lipases," *Biotechnology Advance*, Vol. 19, No. 8, 2001, pp. 627- 662.

[77] H. Fukuda, A. Kondo and H. Noda, "Biodiesel Fuel Production by Transesterification of Oils," *Journal of Bioscience and Bioengineering*, Vol. 92, No. 5, 2001, pp. 405- 416.

[78] S. Pedersen and M. W. Christensen, "Immobilized Biocatalysts," *Applied biocatalysis. P. Adlercreutz*, Harwood Academic Publishers, Amsterdam, 2000, pp.213-228.

[79] A. Salis, E. Sanjust, V. Solinas and M. Monduzzi, "Commercial Lipase Immobilization on Accurel MP1004 Porous Polypropylene," *Biocatal. Biotransf*, Vol. 23, No. 5, 2005, pp. 381-386.

[80] H. M. Chang, H. F. Liao, C. C. Lee and C. J. Shieh, "Optimized Synthesis of Lipase-Catalyzed Biodiesel by Novozym 435," *Journal of Chemical Technology & Biotechnology*, Vol. 80, No. 3, 2005, pp. 307-312.

[81] D. De Oliveira, M. Di Luccio, C. Faccio, C. D. Rosa, J. P. Bender, N. Lipke, S. Menoncin, C. Amroginski and J. V. De Oliveira, "Optimization of Enzymatic Production of Biodiesel from Castor Oil in Organic Solvent Medium," *Applied Biochemistry and Biotechnology*, Vol. 115, No. 1-3, 2004, pp. 771-780.

[82] G. Kminek and J. L. Bada, "The Effect of Ionizing Radiation on the Preservation of Amino Acids on Mars. Earth Planet," *Science Letters*, Vol. 245, No. 1-2, 2006, pp. 1-5.

[83] L. D. Barron, "Chirality and Life," *Space Science Reviews*, Vol. 135, No. 1-4, 2008, pp. 187-201.

[84] L. D. Hutt, D. P. Glavin and R. A. Mathies, "Microfabricated Capillary Electrophoresis Amino Acid Chirality Analyzer for Extraterrestrial Exploration," *Analytical Chemistry*, Vol. 71, No. 18, 1999, pp. 4000-4006.

[85] "Exomars Mission Conference," 2005. http://www.aurora.rl.ac.uk/Report_of_Pasteur_9_Sept. pdf

[86] L. Cao and Schmidt, "Immobilized Enzymes: Science or Art?" *Current Opinion in Chemical Biology*, Vol. 9, No. 2, 2005, pp. 217-226.

[87] B. Chen, M. E. Miller and R. A. Gross, "Effects of Porous Polystyrene Resin Parameters on Candida Antarctica Lipase B Adsorption, Distribution, and Polyester Synthesis Activity," *Langmuir*, Vol. 23, No. 11, 2007a, pp. 6467-6474.

[88] M. I. Kim, J. Kim, J. Lee, H. Jia, H. Bin Na, J. K. Youn, J. H. Kwak, A. Dohnalkova, J. W. Grate and P. Wang, "Crosslinked Enzyme Aggregates in Hierarchically-Ordered Mesoporous Silica: A Simple and Effective Method for Enzyme Stabilization," *Biotechnology and Bioengineering*, Vol. 96, No. 2, 2007, pp. 210-218.

[89] M. C. Rosales-Hernandez, J. E. Mendieta-Wejebe, J. Correa-Basurto, J. I. Vazquez-Alcantara, E, Terres-Rojas and J. Trujillo-Ferrara, "Catalytic Activity of Acetylcho-

 

linesterase Immobilized on Mesoporous Molecular Sieves," *International Journal of Biological Macromolecules*, Vol. 40, No. 5, 2007, pp. 444-448.

[90] A. M. Wang, C. Zhou, H. Wang, S. B. Shen, J. Y. Xue and P. K. Ouyang, "Covalent Assembly of Penicillin Acylase in Mesoporous Silica Based on Macromolecular Crowding Theory," *Chinese Journal of Chemical Engineering*, Vol. 15, No. 6, 2007, pp. 788-790.

[91] A. Wang, H. Wang, S. Zhu, C. Zhou, Z. Du and S. Shen, "An Efficient Immobilizing Technique of Penicillin Acylase with Combining Mesocellular Silica Foams Support and P-Benzoquinone Cross Linker," *Bioprocess and Biosystems Engineering*, Vol. 31, No. 5, 2008a, pp. 509-517.

[92] T. Boller, C. Meier and S. Menzler, "Eupergit Oxirane Acrylic Beads: How to Make Enzymes Fit for Biocatalysis," *Organic Process Research Development*, Vol. 6, 2002, pp. 509-519.

[93] A. S. M. Chong and X. S. Zhao, "Design of Large-Pore Mesoporous Materials for Immobilization of Penicillin G Acylase Biocatalyst," *Catalysis Today*, Vol. 93-95, 2004, pp. 293-299.

[94] C. H. Lei, Y. S. Shin, J. Liu and E. J. Ackerman, "Entrapping Enzyme in a Functionalized Nanoporous Support," *Journal of American Chemical Society*, Vol. 124, No. 38, 2002, pp. 11242-11243.

[95] A. M. Wang, M. Q. Liu, H. Wang, C. Zhou, Z. Q. Du, S. M. Zhu, S. B. Shen and P. K. Ouyang, "Improving Enzyme Immobilization in Mesocellular Siliceous Foams by Microwave Irradiation," *Journal of Bioscience and Bioengineering*, Vol. 106, No. 3, 2008b, pp. 286-291.

[96] M. S. Cheung and D. Thirumalai, "Nanopore-Protein Interactions Dramatically Alter Stability and Yield of the Native State in Restricted Spaces," *Journal of Molecular Biology*, Vol. 357, No. 2, 2006, pp. 632-643.

[97] R. Szamocki, A. Velichko, F. Mucklich, S. Reculusa, S. Ravaine, S. Neugebauer, W. Schuhmann, R. Hempelmann and A. Kuhn, "Improved Enzyme Immobilization for Enhanced Bioelectrocatalytic Activity of Porous Electrodes," *Electrochemistry Communications*, Vol. 9, No. 8, 2007, pp. 2121-2127.

[98] R. J. Chen, Y. G. Zhang, D. W. Wang and H. J. Dai, "Noncovalent Sidewall Functionalization of Single-Walled Carbon Nanotubes for Protein Immobilization," *Journal of American Chemical Society*, Vol. 123, No. 16, 2001, pp. 3838-3839.

[99] L. S. Wan, B. B. Ke and Z. K. Xu, "Electrospun Nanofibrous Membranes Filled with Carbon Nanotubes for Redox Enzyme Immobilization," *Enzyme Microbial Technology*, Vol. 42, No. 4, 2008, pp. 332-339.

[100] G. Bayramoglu, S. Kiralp, M. Yilmaz, L. Toppare and M. Y. Arica, "Covalent Immobilization of Chloroperoxidase onto Magnetic Beads: Catalytic Properties and Stability," *Biochemical Engineering Journal*, Vol. 38, No. 2, 2008, pp. 180-188.

[101] A. Dyal, K. Loos, M. Noto, S. W. Chang, C. Spagnoli, K. Shafi, A. Ulman, M. Cowman and R. A. Gross, "Activity of Candida Rugosa Lipase Immobilized on Gamma-Fe2o3 Magnetic Nanoparticles," *Journal of American Chemical Society*, Vol. 125, No. 7, 2003, pp. 1684-1685.

[102] X. Q. Liu, Y. P. Guan, R. Shen and H. Z. Liu, "Immobilization of Lipase onto Micron-Size Magnetic Beads," *Journal of Chromatography B-Analytical Technologies in the Biomedical and Life Sciences*, Vol. 822, No. 1-2, 2005, pp. 91-97.

[103] S. Sadasivan and G. B. Sukhorukov, "Fabrication of Hollow Multifunctional Spheres Containing MCM-41 Nanoparticles and Magnetite Nanoparticles Using Layer-by-Layer Method," *Journal of Colloid and Interface Science*, Vol. 304, No. 2, 2006, pp. 437-441.

[104] J. Kim, J. Lee, H. B. Na, B. C. Kim, J. K. Youn, J. H. Kwak, K. Moon, E. Lee, J. Park and A. Dohnalkova, "A Magnetically Separable, Highly Stable Enzyme System Based on Nanocomposites of Enzymes and Magnetic Nanoparticles Shipped in Hierarchically Ordered, Mesocellular, Mesoporous Silica," *Small*, Vol. 1, 2005, p. 1203.

[105] I. Hegedus and E. Nagy, "Improvement of Chymotrypsin Enzyme Stability as Single Enzyme Nanoparticles," *Chemical Engineering Science*, Vol. 64, No. 5, 2009, pp. 1053-1060.

[106] M. Yan, J. Ge, Z. Liu and P. K. Ouyang, "Encapsulation of Single Enzyme in Nanogel with Enhanced Biocatalytic Activity and Stability," *Journal of American Chemical Society*, Vol. 128, No. 34, 2006, pp. 11008-11009.

[107] J. Kim and J. W. Grate, "Single-Enzyme Nanoparticles Armored by a Nanometer-Scale Organic/Inorganic Network," *Nano Letters*, Vol. 3, No. 9, 2003, pp. 1219-1222.

[108] Y. Tanaka, Y. Tsuruda, M. Nishi, N. Kamiya and M. Goto, "Exploring Enzymatic Catalysis at a Solid Surface: A Case Study with Transglutaminase-Mediated Protein Immobilization," *Organic Biomolecular Chemistry*, Vol. 5, No. 11, 2007, pp. 1764-1770.

[109] L. S. Wong, J. Thirlway and J. Micklefield, "Direct Site-Selective Covalent Protein Immobilization Catalyzed by a Phosphopantetheinyl Trans Ferase," *Journal of American Chemical Society*, Vol. 130, No. 37, 2008, pp. 12456-12464.

[110] K. Buchholz, "Non Uniform Enzyme Distribution Inside Carriers," *Biotechnology Letters*, Vol. 1, No. 11, 1979, pp. 451-456.

[111] B. Chen, E. M. Miller, L. Miller, J. J. Maikner and R. A. Gross, "Effects of Macroporous Resin Size on Candida Antarctica Lipase B Adsorption, Fraction of Active Molecules, and Catalytic Activity For Polyester Synthesis," *Langmuir*, Vol. 23, No. 3, 2007b, pp. 1381-1387.

[112] L. M. Van Langen, M. H. A. Janssen, N. H. P. Oosthoek, S. R. M. Pereira, V. K. Svedas, F. van Rantwijk and R. A. Sheldon, "Active Site Titration as a Tool for the Evaluation of Immobilization Procedures of Penicillin Acylase," *Biotechnology Bioengineering*, Vol. 79, No. 2, 2002, pp. 224-228.

[113] A. M. Wang, C. Zhou, M. Q. Liu, Z. Q. Du, S. M. Zhu, S. B. Shen and P. K. Ouyang, "Enhancement of Micro-

 

wave-Assisted Covalent Immobilization of Penicillin Acylase Using Macromolecular Crowding And Glycine Quenching," *Journal of Bioscience and Bioengineering*, Vol. 107, No. 3, 2009a, pp. 219-224.

[114] A. Naqvi and P. Nahar, "Photochemical Immobilization of Proteins on Microwave-Synthesized Photoreactive Polymers," *Analytical Biochemistry*, Vol. 327, No. 1, 2004, pp. 68-73.

[115] S. Kumar and P. Nahar, "Sunlight-Induced Covalent Immobilization of Proteins," *Talanta*, Vol. 71, No. 3, 2007, pp. 1438-1440.

[116] R. D. Rogers and K. R. Seddon, "Ionic Liquids-Solvents of the Future?" *Science*, Vol. 302, No. 5646, 2003, pp. 792-793.

[117] K. E. Gutowski, G. A. Broker, H. D. Willauer, J. G. Huddleston, R. P. Swatloski, J. D. Holbrey, R. D. Rogers, "Controlling the Aqueous Miscibility of Ionic Liquids: Aqueous Biphasic Systems of Water-Miscible Ionic Liquids and Water-Structuring Salts for Recycle, Metathesis, and Separations," *Journal of American Chemical Society*, Vol. 125, No. 22, 2003, pp. 6632-6633.

[118] V. Rumbau, R. Marcilla, E. Ochoteco, J. A. Pomposo and D. Mecerreyes, "Ionic Liquid Immobilized Enzyme for Biocatalytic Synthesis of Conducting Polyaniline," *Macromolecules*, Vol. 39, No. 25, 2006, pp. 8547-8549.

[119] R. A. Sheldon, R. M. Lau, M. J. Sorgedrager, F. Van Rantwijk and K. R. Seddon, "Biocatalysis in Ionic Liquids," *Green Chemistry*, Vol. 4, 2002, pp. 147-151.

[120] F. Van Rantwijk, R. M. Lau and R. A. Sheldon, "Biocatalytic Transformations in Ionic Liquids," *Trends Biotechnology*, Vol. 21, No. 3, 2003, pp. 131-138.

 

# Call for Papers

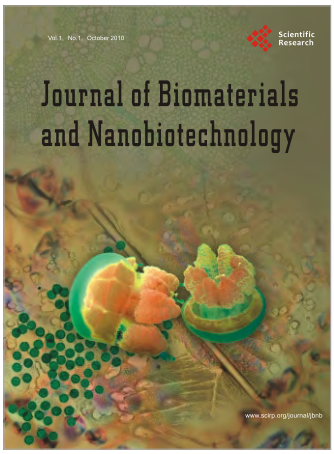


# Journal of Biomaterials and Nanobiotechnology

http://www.scirp.org/journal/jbnb

**Journal of Biomaterials and Nanobiotechnology** is an international, interdisciplinary, English-language publication of original contributions concerning studies of the preparation, performance, and evaluation of biomaterials; the chemical, physical, toxicological, mechanical, electrochemical and optical behavior of nanostructured materials for biotechnology applications. The goal of this journal is to keep a record of the state-of-the-art research and to promote study, research and improvement within its various specialties. With an open access publication model of this journal, all interested readers around the world can freely access articles online. Now we sincerely invite you to submit your research manuscript to JBNB.

## Subject Coverage

Journal of Biomaterials and Nanobiotechnology publishes original papers including but not limited to the following fields:

- Development, design and synthesis of biocompatible biomaterials (sol-gel materials, glasses, ceramics, polymers, hydrogels, metal-organic frameworks, organic-inorganic hybrid materials, nanocomposites, combinations of synthetic materials and living cells and tissues, porous materials) as bulk and thin-films

  Nanoparticles (fullerenes, carbon nanotubes, silica based nanoparticles…) as biomarkers and fluorescents tags for cell detection, imaging and drug delivery systems
- Nanocrystals and bio-crystallization processes
- Self-assembly of biological molecules
- Bio-induced nanopatterning, arrays of biological molecules, bioships
- Biomimetics and bio-inspired materials
- Nanocapsules
- Bio-encapsulation, bio-adsorption, controlled release of biomolecules (drugs, proteins, etc…), nutraceuticals

  Nanostructured materials : micro- and nanofluidics
- Photo-induced species and structure conformations of biomolecules in biomaterials
- Bio-MEMS
- Theranostics and Diagnostics tools: emerging techniques involved in bio-detection and analysis of individual biological molecules (imaging, spectroscopy, microscopy…
- Molecular recognition techniques: biosensors
- Biomolecules/surfaces interactions studies: biocompatibility of materials, biomolecules conformations, structure and dynamics at surfaces, molecular interactions, biological activity, thermodynamics and pharmacokinetics of nanostructured materials

We are also interested in: 1) Short-Reports 2-5 page papers where an author can either present an idea with theoretical background but has not yet completed the research needed for a complete paper or preliminary data; 2) Book Reviews-Comments and critiques.

## Notes for Intending Authors

Your paper should not have been previously published or be currently under consideration for publication any place else. Submit your paper electronically through the JBNB online system. All papers are subject to peer review. After your paper has been accepted, you must sign a copyright transfer agreement with JBNB. Papers accepted for publication will be available free online. A fee will be charged to cover the publication cost. Manuscripts must be written in English.

## Website and E-Mail

http://www.scirp.org/journal/jbnb E-mail: jbnb@scirp.org

*Journal of Biomaterials and Nanobiotechnology*, **2010, 1, 1-76.**
Published Online October 2010 in SciRes (http://www.SciRP.org/journal/jbnb).

# TABLE OF CONTENTS

**Volume 1 Number 1** **October 2010**



 